

PRODUCTION INDUCED RESERVOIR COMPACTION
AND SURFACE SUBSIDENCE,
WITH APPLICATIONS TO 4D SEISMIC

A DISSERTATION
SUBMITTED TO THE DEPARTMENT OF GEOPHYSICS
AND THE COMMITTEE ON GRADUATE STUDIES
OF STANFORD UNIVERSITY
IN PARTIAL FULFILLMENT OF THE REQUIREMENTS
FOR THE DEGREE OF
DOCTOR OF PHILOSOPHY

Haibin Xu
July 2002

© Copyright by Haibin Xu 2002
All Rights Reserved

I certify that I have read this dissertation and that in my opinion it is fully adequate, in scope and quality, as a dissertation for the degree of Doctor of Philosophy.

Amos Nur (Principal Advisor)

I certify that I have read this dissertation and that in my opinion it is fully adequate, in scope and quality, as a dissertation for the degree of Doctor of Philosophy.

Gary Mavko (Geophysics)

I certify that I have read this dissertation and that in my opinion it is fully adequate, in scope and quality, as a dissertation for the degree of Doctor of Philosophy.

Jack Dvorkin (Geophysics)

Approved for the University Committee on Graduate Studies:

Abstract

Reservoir compaction due to hydrocarbon production and pore pressure depletion is common in unconsolidated reservoirs worldwide. Compaction may result in well failure, surface subsidence, and platform sinking. Surface subsidence is the differential sinking of the Earth's surface with respect to the surrounding terrain. Subsidence occurs in many parts of the world, in some cases as much as tens of meters within the short period of a few decades. Examples of subsidence from Wilmington, California; Belridge, California; Ekofisk, the North Sea; Lake Maracaibo, Venezuela; and Groningen, the Netherlands, are well documented.

There are four major implications of reservoir compaction and surface subsidence on the economic performance of a reservoir: (1) Reservoir compaction and surface subsidence are very common geohazards. They may result in well failure and platform sinking, which are very costly to repair. (2) For oil / gas fields located at low surface level, subsidence may pose severe environmental problems. (3) Porosity loss as a result of reservoir compaction may have a significant impact on the calculation of reserves. (4) In some low-pressure reservoirs, reservoir compaction is a major drive mechanism for petroleum production.

In this path-finding study, we use InSAR to measure surface subsidence occurred in oil fields due to production, and investigate the applications and implications of reservoir compaction and surface subsidence in reservoir monitoring. Traditionally, reservoir monitoring is carried out through 4D seismic technique. In this thesis, we study how to use InSAR measured subsidence as an alternate or supplemental monitoring tool in addition to 4D seismic. Our major findings are the following:

(1) For the traditional “geomechanics + flow simulation” workflow of subsidence prediction, InSAR provides massive data for validation. Previously, those types of predictions can only be validated at very few points where geodetic survey data are available. In Chapter 3, we present an example in the Belridge and Lost Hills fields where such massive subsidence distribution data are obtained from InSAR.

(2) InSAR can be used as a stand-alone tool for reservoir characterization and monitoring. First, the magnitude and patterns of subsidence are often good indications of reservoir shape, size and depth, as well as being affected by reservoir rock properties and

production history. In Chapter 3, we show that the large subsidence in Lost Hills compared to Belridge, is caused by its shallow reservoir depth, large reservoir thickness, and large reservoir rock compressibility, although Lost Hills has a much smaller production volume than Belridge. We also suggest that the asymmetry of subsidence in the Lost Hills field is caused by the asymmetric distribution of production volume within the field. Second, subsidence pattern may also be a good indication of permeability anisotropy. In Chapter 4, we perform numerical simulations for an imaginary reservoir, which is homogeneous and isotropic except that the permeability may be anisotropic. We perform numerical simulations for different combinations of permeability anisotropy and boundary conditions. We find that subsidence pattern is affected by both factors. Since we often have fairly good knowledge about the tectonic settings and boundaries of a reservoir from geology, using subsidence from InSAR, we may be able to infer information about permeability anisotropy, which is otherwise very difficult to obtain. Finally, subsidence pattern may be an indication of bypassed oil. For shallow reservoirs, if the compaction heterogeneity is not blurred when expressed at the surface, it might be possible to identify bypassed oil from the pattern of subsidence.

(3) InSAR can also be used together with 4D seismic for reservoir monitoring. First, traditionally, 4D seismic changes are interpreted in terms of pressure and saturation changes in the reservoir, while porosity is assumed to be constant during the production. This is often inaccurate or incorrect. By using compaction as an additional input, we can improve the accuracy of 4D seismic interpretations. In Chapter 5, we will show how to integrate 4D seismic and geomechanics, to interpret 4D seismic signatures in terms of not only pressure and saturation changes, but also porosity changes. Second, as we show in Chapter 5, using 4D seismic and geomechanics, we can predict porosity loss in a reservoir. On the other hand, this porosity loss in the reservoir is related to surface subsidence. If we know how the two are related, then the surface subsidence from InSAR can be used as an independent source for checking the validity of the porosity loss prediction from 4D seismic. In Chapter 3, we will show the relationship between absolute volume loss on the ground (subsidence) and the absolute volume loss in the reservoir (compaction, or porosity loss). This relationship provides a way to calculate porosity loss from surface subsidence, and hence provides an integral constraint to the 4D seismic prediction of porosity loss.

This thesis includes 5 chapters. We present systematically the observation, modeling, and implications of production-induced reservoir compaction and surface subsidence, using differential InSAR, Reservoir Simulation, and Rock Physics. The chapters are:

Chapter 1: Introduction to production-induced reservoir compaction and surface subsidence. We review the phenomenon, observation, modeling, inversion, and monitoring of surface subsidence. We describe in detail the new technique of InSAR for measuring surface subsidence, and discuss the ultimate potentials of InSAR for petroleum applications.

Chapter 2: Biot's linear quasi-static poroelasticity theory, as applied to the modeling of reservoir compaction and surface subsidence. We compare the original formulation with a few simplified forms of the Biot's theory. We also present a simplified form of the Biot's theory for "disk-shaped" reservoirs, which is used in Chapter 3.

Chapter 3: InSAR measurement of production-induced surface subsidence in Belridge and Lost Hills oil fields, California, and numerical modeling that relates observed subsidence to reservoir production history. We develop a method for calculating the "volume loss ratio", which is the ratio of absolute volume loss on the ground (subsidence) to the absolute volume loss in the reservoir (compaction). We discuss the implications of InSAR in reservoir monitoring.

Chapter 4: Investigation of the relationship between reservoir compaction and reservoir properties, through reservoir simulation. We show the combined effect of permeability anisotropy and boundary conditions on the geometric patterns of resulting surface subsidence. We demonstrate through an example that, in principle, InSAR can be used as a stand-alone tool for reservoir monitoring.

Chapter 5: Investigation of 4D seismic response to reservoir compaction, using published laboratory pressure-porosity and pressure-velocity data. We used laboratory measurements of porosity, pressure, and velocity on hand-made clay-sand mixtures. Through this example, we demonstrate that by combining 4D seismic and geomechanics, we can predict porosity loss in a reservoir due to production. This prediction can be constrained by InSAR measured subsidence, using the "volume loss ratio" we developed in Chapter 3.

Acknowledgements

I answer his questions, he questions my answers, loop after loop. Then I got my Ph.D. Thank you, Amos. You're the best advisor anyone can dream of. Well, maybe the only drawback of being your student is that, I have to share you with the whole University (Amos is the director of the Overseas Studies Program at Stanford). I have benefited from your six questions throughout my research ---"*What is the problem? Why is it important? What is known? What can I do? Anticipated results? Anticipated Impact?*"

I am so grateful to my co-advisor Jack Dvorkin for his sharing of my excitements as well as frustrations in research. Without his guidance, advise and critique, this work won't be possible. Jack has the greatest vision and insights. He is the standard that I look up to now in academia, and future in industry.

This work also has benefited greatly from Gary Makvo's outstanding teaching and constructive comments. I learned a lot from him on how to make clear and meaningful presentations. I made friends with many of Gary's former students. One impression they gave me is that, they're so grateful that Gary cares not merely for his students' rock physics knowledge, but also their future opportunities (such as career concerns).

I thank Howard Zebker and the SAR group (especially Mamta Sinha) for their help in SAR research. I thank my thesis committee, Jef Caers (chairman), Howard Zebker, Amos Nur, Gary Mavko, and Jack Dvorkin, for their time and patience.

Joining SRB was a defining moment in my life. The past 5 years has been one of the best parts in my life experience. I'd like to thank the SRB group. Margaret has been of tremendous help. Thanks, Manika and Tapan, for being great mentors and friends to all of us. I like to thank Aya, Diana, Emma, Juan, Manuel, Mike, and Salman. I especially like to thank my former and current officemates, Sandra, Andres, Youngseuk, Alexander, Mario, and Zohar.

I like to thank SRB graduates Zhijing Wang, Dehua Han, and Hezhu Yin. As a Chinese student, it's certainly flattering for me to hear their names mentioned again and again at SRB seminars. One time a student presented her results on clay velocity measurements, which contradicted Zhijing's earlier results. One said: "As long as Zhijing doesn't oppose (in the SRB annual meeting), it's fine." Another joked: "Well, maybe we should arrange a phone call for him when you talk."

I like to thank the staff in the Geophysics Department, especially Agnes Kehoe, for making everything so smooth.

I enjoyed many classes in Stanford. The following stand out: GP112(Mukerji), GP262(Mavko), GP210(Claerbout), EE261 (Kazofsky), and CS106x (Plummer).

I like to thank the many people (Stan Lee, Shiyu Xu, Wenjie Dong, Lydia Deng, Jennifer Zhang, Houzhu Zhang, Biaolong Hua) who made my summer internship in Mobil such a pleasant one. I like to thank WesternGeco (Nader Dutta, Lee Bell, Olav Holberg) for inviting me to work in their Seismic Reservoir Services division after my graduation.

Many thanks to my parents Xu Shangming and Fu Shangshu. Many thanks to my sisters Xu Zhiqin and Xu Xueqin and their families. I thank my grandmother, uncles, aunts, and many cousins. My mother's parents and my father's father all died before I was born, due to starvation in the 60s. This grandmother is the only grandmother that I know. She is fortunate to have more than 20 grandchildren.

My hometown is Lujiang, Anhui, China. I left home when I was 13 years old. I'm glad that I've been able to be independent early, but I also regret that I can't take care of my parents now as they've become older. At the time of this writing, my mother is going through a 3-month procedure of medical treatment. I thank my father and elder sister for taking care of her so patiently and lovingly. I can't wait for my parents' visit to Houston next year.

My special thanks go to my fiancée Shana Shi. Thank you Shana, for the long period of struggling together against the old Chinese-style family opposition towards our relationship. I never challenge their good intentions, but often there is nothing that does more harm than good intentions. The good thing is, it helped us mature. I haven't had much life in the past months due to the overwhelming thesis work. I really look forward to some day when we can sit down in a sofa and watch some TV together at night, worry-free, in a little apartment that we call "home". Shana, I love you so much.

I thank the Shi family, especially Jenny Shi, Yanmin Shi, Xinen Shi, and Shuping Li. You're my family in America. I'm proud that finally Shana and I have your trust and good wish towards our relationship. One thing for sure is, after I have started working in Houston, the concept of "coming home", especially during holidays, will be "going to our home in Palo Alto". I also like to thank Hal Lemmon, the other Ph.D. in the family, who is so kind and intelligent, and helped Shana and me so much.

I'd like to thank my friends. Here at Stanford University and the San Francisco bay area. In California. Many in Texas, both Dallas and Houston. Across the United States and also many in China. Friends I made in parties, in classrooms, in outdoor activities, in professional conferences, and in the job-hunting process. My friends during childhood and teenage time were Xu Zhisheng, Xu Zhifeng, Liu Li, Peng Xuelian, Wang Yougui, Ji Hong, Qu Licheng, Xu Shangfei, Sheng Li, Wang Shaoyong, Liu Haifeng, ... I like to thank the Chinese gangs in college and graduate

school, especially USTC 9207, EDPC (eat drink play club) 1998, and Lujiang USTCers. I like to thank Zhao Fang, Chen Min, Xu Haifeng, Jin Zhen, Gao Yun, Elaine White, ... in USTC. The one-day trip to Yefu Mountain, and the midnight trip to Science Island, were two of the best trips I ever had. EDPC members are now Statistics professor in Duke, electric engineer in Onetta, petroleum engineer in BP, ... I like to thank all the new friends I made since 1997. I like to thank the first group of people who helped me settle down in the USA in 1997, Lily Zhang, Wenjie Hsieh, ... I like to thank Zhao Yi, Liu Yuguang, Teng Li, Wu Chunling, Chen Weitian, Shan Guojian, ... I like to thank Ah-san Wang of Caltech (now in Michigan). Especially I'd like to thank two of my best friends, my buddies from undergraduate time, Cheng Xing, who is now at Univ. of Michigan, and Chen Yun, who is now at Univ. of Illinois, for being in Stanford physically during my defense.

I'd like to thank a few more people, real or in fiction, who had significant influence on me in my younger ages: Wei Xiaobao, Vito and Michael Corleone, and Russell Crowe (*"for anybody who's on the downside of advantage and relying purely on courage, it's possible"*).

My friend asks me: what did you learn in Stanford over the last 5 years? I answered: I learned three things:

First, I learned the basic living skills. I learned how to drive a stick-shift car, I learned how to pay taxes, and I learned some driving rules in traffic schools from time to time.

Second, I learned a little bit on how to do research. I learned how to search for literature. I learned how to write down my thoughts. I learned how to give a presentation. I learned how to keep Shana busy so that I had time to study.

Third, and most importantly, I learned how to live in a country of great talents and free minds. I learned that happiness is really not a reaction, but a choice. I learned that what separates people is not color, religion, or accent, but ignorance. I've come to determine that my goal for a fulfilled life is that someday I can say without a doubt to myself: "I worked, I loved, I lived".

For all the people who helped me learn these, I'm so grateful to you.

Table of Contents

Abstract	iv
Acknowledgements	vii
Table of Contents	x
List of Figures	xiii
List of Tables.....	xvii
Chapter 1	1
Introduction and Overview.....	1
1.1 Abstract.....	1
1.2 Terminology/Phenomenology of Subsidence	1
1.3 Observation of Subsidence by InSAR	6
1.4 Inversion	8
1.5 Monitoring of Surface Subsidence	10
1.6 Previous Research Activities in Compaction and Subsidence.....	10
1.7 Ultimate Potentials of the Petroleum Applications of InSAR	14
1.8 Description of Thesis Chapters.....	16
1.9 References.....	17
Chapter 2	21
Biot’s Linear Quasi-Static Isotropic Poroelasticity	21
2.1 Abstract.....	21
2.2 The Mechanical Description	21
2.2.1 “Variables” in the Biot Theory	22
2.2.2 “Parameters” in the Biot Theory	24
2.3 Formulation of Biot’s Linear Isotropic Quasi-static Poroelasticity	24
2.3.1 Constitutive Laws	24
2.3.2 Volumetric Responses of Poroelasticity	26
2.3.3 Governing Equations.....	27
2.3.4 Field Equations	29
2.4 Comparisons Among Several Formulations	30
2.4.1 Elastic and Poroelastic Formulations	31
2.4.2 Reservoir Simulation and Poroelasticity	31
2.5 Surface Deformation for Axisymmetric and Disk-Shaped Reservoirs	33
2.6 Conclusions.....	34
2.7 References.....	34
Chapter 3	35
Production-Induced Surface Subsidence in the Belridge / Lost Hills Oil Fields, Measured by InSAR.....	35

3.1 Abstract.....	35
3.2 Introduction	36
3.3 Geology and Production History of Belridge / Lost Hills Fields.....	37
3.4 Subsidence from InSAR	40
3.5 Subsidence from Oil Production.....	43
3.6 Discussion.....	46
3.6.1 Factors Affecting Surface Subsidence	46
3.6.2 Relationship Between Subsurface Compaction and Surface Subsidence	50
3.7 Conclusions.....	52
3.8 Acknowledgments	52
3.9 Appendix : InSAR Basics.....	52
3.9.1 Where to Look	52
3.9.2 Basic Concepts.....	53
3.9.3 Brief Theory.....	53
3.9.4 Quick Facts	55
3.9.5 Previous Applications	56
3.10 References.....	56
Chapter 4.....	59
Static Monitoring: Compaction/Subsidence as a Stand-Alone Monitoring Tool.....	59
4.1 Abstract.....	59
4.2 Introduction	59
4.3 Numerical Simulation.....	61
4.3.1 Setup	62
4.3.2 Handling of Boundary Conditions	63
4.4 Simulation Results	63
4.4.1 Closed Boundary and Isotropic Permeability --- Plates (1,1) & (2,1) of Figure 4.2	64
4.4.2 Open Boundary and Isotropic Permeability --- Plates (1,2) & (2,2) of Figure 4.2	65
4.4.3 Open Boundary and Anisotropic Permeability, Plate (3,2) of Figure 4.2	65
4.4.4 Closed Boundary and Anisotropic Permeability, Plate (3,1) of Figure 4.2, and Explanation From the Analytical Solution.....	66
4.4.5 Closed Boundary Along One Direction, the Last Two Columns in Figure 4.2	67
4.5 Rectangular Reservoir.....	67
4.6 Discussion.....	69
4.7 Conclusions.....	70
4.8 Acknowledgments	70
4.9 References.....	71
Chapter 5	72
Dynamic Monitoring: Compaction/Subsidence as an Additional Input/Constraint in the 4D Seismic Monitoring Workflow.....	72
5.1 Abstract.....	72
5.2 Introduction	72
5.3 The Status & Limitations in Today's Reservoir Compaction Study.....	74
5.4 The Status & Limitations in Today's 4D Seismic Study	74

5.5 Studying Reservoir Compaction and 4D Seismic Together 78

5.6 Yin’s Laboratory Data of Shaly Sands 79

5.7 Reservoir Compaction During Primary Depletion..... 83

5.8 A Synthetic Example 85

5.9 Reservoir Compaction for Cycles of Depletion and Injection..... 88

5.10 Discussion..... 90

5.11 Conclusions..... 92

5.12 Acknowledgments 92

5.13 References..... 92

List of Figures

Figure 1.1: Joseph Poland of USGS stands near BM S661 Southwest of Mendota in the San Joaquin Valley, California in 1977. The nine meters of cumulative subsidence is due to intensive withdrawal of groundwater (from <i>Poland</i> , 1984).....	2
Figure 1.2: Surface subsidence near Lake Maracaibo, Venezuela, due to production of heavy oil (from the Internet).....	3
Figure 1.3: Cartoon showing the possible mechanism of production-induced reservoir compaction and surface subsidence. Surface subsidence commonly forms a bowl shape (from <i>Piau</i> , 1994).....	4
Figure 1.4: Principle of differential InSAR for measuring surface deformation (from http://www-star.stanford.edu/sar_group).....	7
Figure 1.5: Integral inversion yields subsurface pressure distribution from surface deformation (from <i>Nur</i> , personal communication).....	9
Figure 1.6: Correlation between subsidence and production/injection in the Wilmington oil field, California, during a period of 30 years between 1937 and 1967 (from <i>Colazas & Strehle</i> , 1995).....	9
Figure 1.7: USGS subsidence interest group conference (from the Internet).....	12
Figure 1.8: USGS subsidence interest group conference (from the Internet).....	13
Figure 3.1: Location of Belridge and Lost Hills oil fields.....	37
Figure 3.2: Satellite intensity image of Lost Hills oil field. It is visible in the image three dark lines: the straight line on top is highway 46, the straight line to the upper right is highway 5, and the curved line is the California Aqueduct. The altitude of ERS satellite is almost 800 km above the ground, but still characteristic on the surface is clear to see.....	40
Figure 3.3: Interferograms of Belridge and Lost Hills oil field. The time lapse is 105 days (11/5/99 – 2/17/96). The perpendicular baseline is 227 meters, hence the image includes both deformation and topography information. Most noticeably, the large fringes to the bottom left are topography effects, while the “bowl” shaped fringes in the image are resulting from deformation.....	42
Figure 3.4: Unwrapped interferogram showing the subsidence in Belridge and Lost Hills oil fields occurred between 11/5/99 – 2/17/96 (105days). The scale is in centimeters. The maximum subsidence reached 15 cm at the center of Lost Hills field.....	43

Figure 3.5: (a) InSAR observed subsidence in Lost Hills oil field occurred between 11/5/99 – 2/17/96 (105days). The dark lines show the locations of profile 1 and 2. The scale is in centimeters. (b). InSAR observed subsidence and theoretical subsidence along profile 1 for assumed reservoir radius of 0.5, 1, 2, and 8 miles, in Lost Hills field for the same period. (c) InSAR observed subsidence and theoretical subsidence along profile 2 for assumed reservoir radius of 0.5, 1, 2, and 8 miles, in Lost Hills field for the same period.	45
Figure 3.6: Well density map of Lost Hills oil field (courtesy of <i>Chevron USA</i>).	47
Figure 3.7: Annual production volume of the Belridge (North and South) and Lost Hills oil fields in barrels.	49
Figure 3.8: Theoretical values of volume loss ratio as a function of the ratio of reservoir depth over reservoir radius, calculated from <i>Geertsma’s</i> model [1973].	51
Figure 3.9: Radar imaging geometry. The solid lines show that radar signal paths for the first interferogram pair formed by antennas at A1 and A2. Dashed lines show signal path for second interferogram acquired over the same site but with antennas located at A1 and A2’ (from <i>Zebker</i> , 1994).	54
Figure 4.1: (left) Surface subsidence over a two-year period between 1992 and 1994 at East Mesa field caused by the activity of a geothermal plant (from <i>Massonnet et al.</i> , 1997). (right) Zoom in of the subsidence area.	60
Figure 4.2: Pressure distribution after 50 days of production. The diagrams on top show boundary conditions --- an arrow that is completely inside the box represents closed boundary, and an arrow that crosses the box represents open boundary. The diagrams to the leftmost show permeability – a short arrow represents $k=100$ mD, and a long arrow represents $k = 500$ mD. Therefore, for example, the image on the bottom right has the following setup: $k_x = 500$ mD, $k_y = 100$ mD, open boundary along x direction (here we use $\gamma_1 = \gamma_2 = 1$), close boundary along y direction (here we use $\gamma_3 = \gamma_4 = 0$).	64
Figure 4.3: Pressure profiles for open boundary and anisotropic permeability.	66
Figure 4.4: Pressure distribution after 50 days of production in a rectangular reservoir, whose length is twice its width. The single producing well is at the center of reservoir. Permeability is isotropic. The boundary is open to the left and right, while closed at the top and bottom.	68
Figure 4.5: Explanation for the observation in Figure 4.4 that pressure drop is more significant along the direction where the boundaries are closed.	68
Figure 5.1: Links among reservoir simulation, 4D processing, 4D modeling, 4D inversion, and seismic history matching. Rock physics plays a central role in the dual processes of 4D modeling and 4D inversion.	75

Figure 5.2: Ultrasonic laboratory measurements on Wilmington sands. (a) Confining pressure vs. porosity, illustrating loading (compaction) and unloading/reloading trends for the two samples in the study. (b) P-wave modulus calculated from pulse transmission measurements vs. porosity, showing time dependence. The loading, unloading and reloading trends can be seen clearly in the data as well [Moos & Chang, 1998].....77

Figure 5.3: Laboratory data of Yin [1992] on room-dry sand-clay mixture of 30% clay content. Top – porosity versus differential (confining minus pore) pressure. The upper branch is loading while the lower branch is unloading. Bottom – P- and S-wave velocity versus differential pressure. The lower branches are for loading while the upper branches are for unloading.....80

Figure 5.4: Laboratory data of Yin [1992] on room-dry sand-clay mixture of 30% clay content. Upper row – P- and S-wave impedance versus the differential pressure. Lower row – Poisson’s ratio versus the differential pressure (left) and versus P-wave impedance (right). In the lower row, the upper branch is for loading while the lower branch is for unloading.81

Figure 5.5: Upper row – P- and S-wave impedance versus the differential pressure for varying saturation. Lower row – Poisson’s ratio versus the differential pressure (left) and versus P-wave impedance (right) for varying saturation. Dry data are from Yin’s [1992] sand-clay mixture of 30% clay content. Saturated data are obtained from fluid substitution based on the dry data. During fluid substitution, uniform and patchy saturation methods have been used. Patchy saturation pattern is not uncommon during recovery in a heterogeneous reservoir.82

Figure 5.6: Patchy fluid substitution to estimate the P-wave impedance and Poisson’s ratio variations within an effective pressure range. Upper row – absolute values. Lower row – values normalized between zero and one. Left column – P-wave impedance. Right column – Poisson’s ratio.....83

Figure 5.7: Upper row – P-wave impedance and S-wave impedance versus differential pressure and for varying saturation using patchy fluid substitution. Lower row – Poisson’s ration versus differential pressure and versus P-wave impedance at varying pressure and saturation. Arrows show increasing Pdiff or Sw. For the bottom right panel, Pdiff = 5, 7.5, 10, 15, 20, 30, 40, 50 MPa, and Sw vary from 0 to 1 with step of 0.1.84

Figure 5.8: Upper row – Differential pressure and water saturation change during gas production from a model rectangular reservoir (map view). Gas is produced from the lower right corner and water is entering into the upper left corner. Lower row – calculated new P-wave impedance and Poisson’s ratio. The initial Impedance and Poisson’s ratio are set to be 3.1km/s*g/cc and 0.36 respectively (uniform).....86

Figure 5.9: Pressure, saturation, and porosity changes from changes of P-wave impedance and Poisson’s ratio.....87

Figure 5.10: The combined effect of pressure, saturation, and porosity on seismic changes in six different domains. Row 1, left, Poisson’s ratio versus P-wave impedance, and right, V_p/V_s ratio versus P-wave velocity. Row 2, left, P- versus S-wave velocity, and right, AVO intercept versus AVO gradient. Row 3, left, acoustic impedance versus elastic impedance at 30° , and right, Lamé’s constant λ versus Lamé’s constant μ , both multiplied by bulk density ρ . In all the domains, blue color corresponds to loading curve in Figure 5.10, and red color corresponds to unloading curve in Figure 5.11. Arrows show the directions of increasing differential pressure and water saturation.89

Figure 5.11: A synthetic example for one cycle of production and injection. The first row corresponds to base survey, the third row corresponds to repeat survey, the fifth row corresponds to a second repeat survey. The second and fourth rows are pressure and saturation changes between the surveys. First row: the initial reservoir condition. Second row: simulated pore pressure and saturation changes during production. Third row: new distributions of pressure, saturation, impedance, Poisson’s ratio, and porosity. Fourth row: simulated pore pressure and saturation changes during pressure restoration Fifth row: new distributions of pressure, saturation, impedance, Poisson’s ratio, and porosity.....90

List of Tables

Table 1.1: Examples of land subsidence observed in oil and gas fields due to production.	5
Table 1.2: Phillips: at Ekofisk oil field.	11
Table 1.3: Shell: at Belridge oil field.	11
Table 2.1: Basic kinematic and dynamic quantities that describe a porous rock.	23
Table 2.2: “Variables” in the Biot theory.	23
Table 2.3: “Parameters” in the Biot theory.	24
Table 2.4: Constitutive laws of elasticity and poroelasticity.	25
Table 2.5: Stress and strain “variables”.	26
Table 2.6: Volumetric responses under drained and undrained conditions.	26
Table 2.7: Some common situations and the theory commonly used corresponding to those situations.	30
Table 2.8: Comparison between poroelasticity and reservoir simulation.	32
Table 3.1: Twenty-five largest oil fields of the United States ranked by cumulative production [International Petroleum Encyclopedia, 1989].	38
Table 3.2: Production history of Belridge and Lost Hills oil fields (<i>bbl</i>).	39
Table 3.3: Key parameters for diatomite formation.	39
Table 3.4: Satellite parameters of the two interferograms.	41
Table 3.5: C_m values (cm^2/kg) for sandstones and carbonates (compiled from Geertsma, 1973). Larger C_m values correspond to softer rocks.	49
Table 4.1: Simulation setup for solving equation (1). The meanings of most of the parameters are straightforward; the meaning of “ γ ” will be explained in the next section.	62

Chapter 1

Introduction and Overview

1.1 Abstract

Surface subsidence is observed worldwide in many producing reservoirs. In this introductory chapter, we will review the phenomenon, observation, modeling, inversion, and monitoring of production-induced reservoir compaction and surface subsidence. We will describe in some detail the new technique of InSAR for measuring surface subsidence, and conclude this chapter by discussing the ultimate potentials of InSAR for petroleum applications.

1.2 Terminology/Phenomenology of Subsidence

We first summarize the terminology/phenomenology in land subsidence due to oil/gas production. Much of the contents are taken from *Piau* [1994] and *Poland* [1984]. We will also present a list of well-known cases of production-induced subsidence.

The compaction/subsidence of petroleum reservoirs and of aquifers is one of the most spectacular, frequently costly and dangerous manifestations of the poromechanical behavior of rocks. Figure 1.1 shows the amount of subsidence at one location in the San Joaquin Valley of California due to intensive groundwater withdrawal. Similar amount of subsidence is observed in Wilmington, California, where the subsidence is due to oil production. Figure 1.2 shows the subsidence in Lake Maracaibo, Venezuela, where dikes have to be built to prevent the lake water from flooding the surrounding area.

The basic mechanism of reservoir compaction and surface subsidence is simple. It is the result of the well-known poromechanical coupling of pore pressure and effective stress in the rocks. Fluid production is accompanied by an expansion of the interstitial fluid in the rock reservoir and hence a fall in pore pressure. That follows an increase in the vertical effective stress in the reservoir, resulting in its compaction. Compaction of

the reservoir is transmitted to the surface and causes vertical movements of the ground. This is the visible part of the phenomenon, known as subsidence.

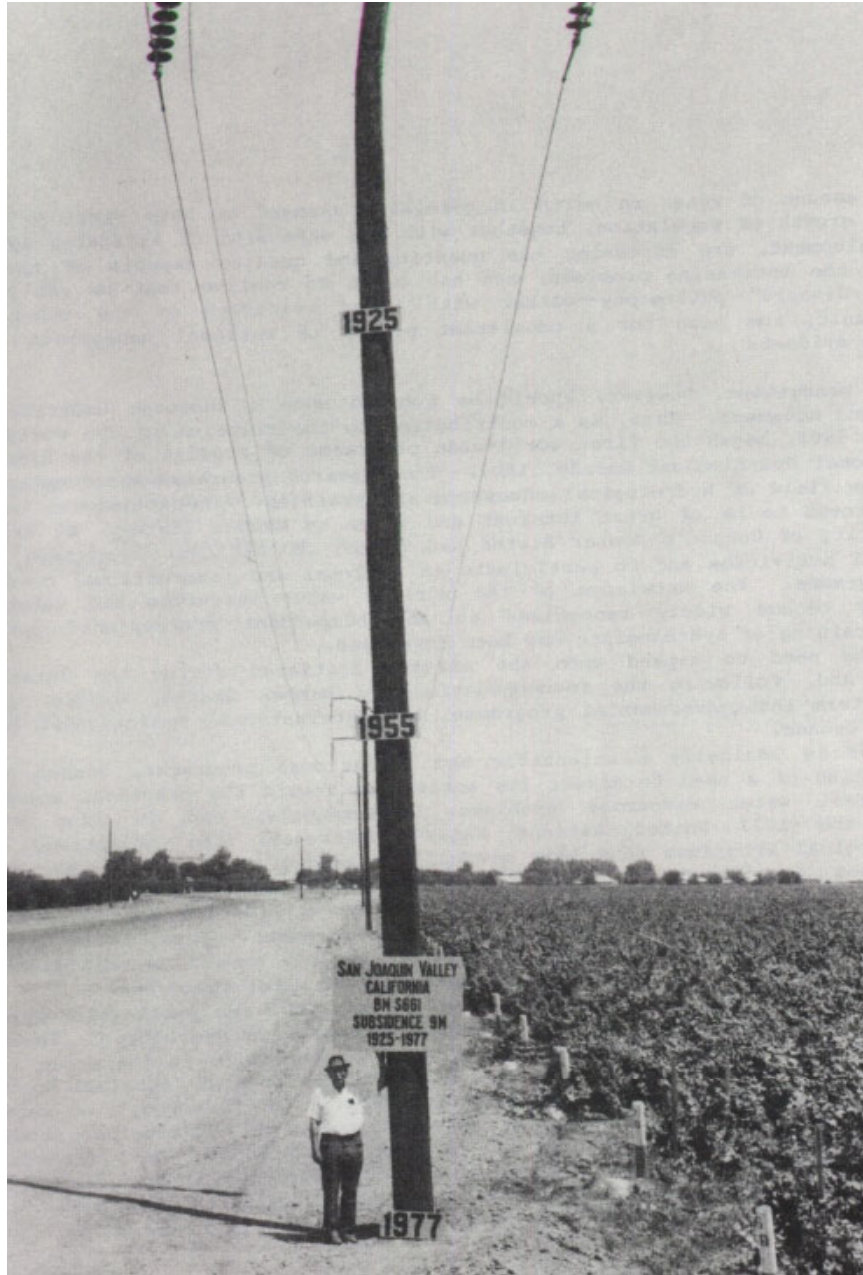


Figure 1.1: Joseph Poland of USGS stands near BM S661 Southwest of Mendota in the San Joaquin Valley, California in 1977. The nine meters of cumulative subsidence is due to intensive withdrawal of groundwater (from Poland, 1984).



Figure 1.2: Surface subsidence near Lake Maracaibo, Venezuela, due to production of heavy oil (from the Internet).

On the surface, the subsided ground is typically basin-shaped; the term used is "subsidence bowl" (Figure 1.3). The differential vertical displacements are accompanied by horizontal displacements directed towards the center of the basin.

Land subsidence has been studied intensively in the past. Different aspects of the phenomenon were addressed. However, an accurate characterization of subsidence due to oil and gas production is rare due to various reasons, one of which is the difficulty of measuring surface subsidence precisely, with high resolution, over a large area, and in a timely fashion. In Chapter 3 of this thesis, we will demonstrate the power of differential InSAR in measuring subsidence compared to traditional geodetic techniques. InSAR technique can potentially solve the difficulty described above.

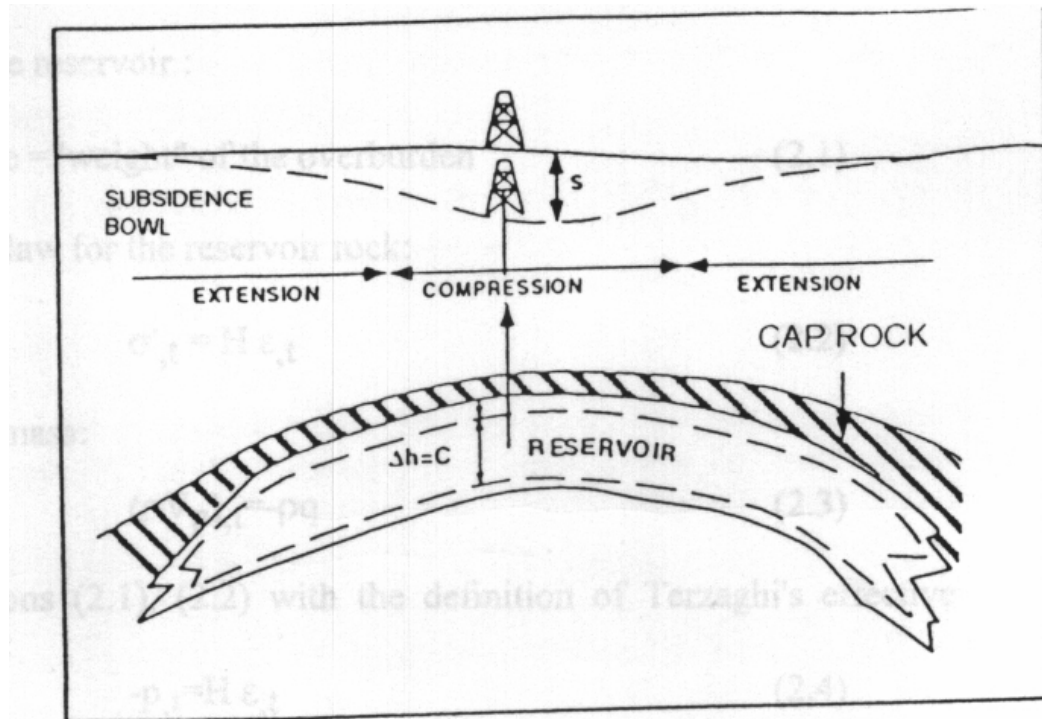


Figure 1.3: Cartoon showing the possible mechanism of production-induced reservoir compaction and surface subsidence. Surface subsidence commonly forms a bowl shape (from Piau, 1994).

Some well-known examples of land subsidence due to hydrocarbon production are:

- (1) Bolivar Coast (Venezuela): on the East coast of Lake Maracaibo. The subsidence affects an area of 450 km^2 and reached its maximum, 4.32 m , in 1978. Dikes and major drainage systems had to be built and pumping implemented to evacuate rainwater.
- (2) Wilmington (California): one of the most spectacular and expensive cases of subsidence, the bowl of subsidence covers 75 km^2 and reached a maximum of 8.8 m in 1965 at the center of the basin. A water injection program began in 1958 to maintain the pressure.
- (3) Ekofisk (North Sea): as of year 1991, subsidence is 6.4 m at the center of the subsidence basin, where most of the operating superstructures (production and injection platforms, waste processing platforms, storage tanks and living quarters) are located. The consequences of the subsidence are aggravated by the marine environment. The reduction in the platform airgaps required an expensive lifting operation to be performed in 1986 (455 million US\$), as well as protection of the central tank by a concrete shell round its periphery (500 million US\$).

Table 1.1: Examples of land subsidence observed in oil and gas fields due to production.

Location	Subsidence Rate	Original Author's notes	Reference
Belridge oil field, California	As high as 30-40 <i>cm/year</i> during 1992-1996	Frequent oil well failures due to subsidence; steam injection is used to reduce the subsidence with <i>limited</i> success	<i>van der Kooij</i> , 1997
Wilmington oil field, California	Cumulative subsidence reached a maximum of around 10 <i>m</i> between 1926-1967	Earthquake could also be an important cause in this field besides production; nevertheless, subsidence rate reached its peak of more than 2 <i>ft/year</i> at some locations in 1951 when oil production was also at its peak	<i>Colazas et al.</i> , 1995
Costa Oriental oil fields, Venezuela	Maximum cumulative subsidence of more than 5 <i>m</i> , maximum rate of 20 <i>cm/year</i> , during 1920-1995	Very shallow reservoir (300-1000 <i>m</i>), unconsolidated and highly porous	<i>Leal et al.</i> , 1995
Groningen gas fields, Netherlands	Some decimeters per year during production history	Minor earthquakes at some points near small production gas fields are noticed; the surface level varies between -1 to 2 <i>m</i> with respect to sea level	<i>Barends et al.</i> , 1995
Po Delta gas field, Italy	4-17 <i>cm/year</i> during 1956-1961	Due to low GWR, extraction of gas in the delta area involved massive water withdrawals.	<i>Brighenli et al.</i> , 1995
Ekofisk field, the North Sea	More than 3 <i>m</i> by 1984 in a period of 20 years	Platform sinking was noticed	<i>Sulak</i> , 1991

Table 1.1 shows a few field cases in which significant subsidence from production is observed. Although there may be tectonic causes involved in the subsidence, the major causes in those cases are ground fluid withdrawal (hydrocarbon production). One evidence supporting this is that, in general, there are fairly good correlations between the subsidence rate and production rate, namely, the faster the production is, the faster the subsidence is [*van der Kooij*, 1997; *Colazas et al.*, 1995].

Land subsidence due to oil production has significant impact on production. In some cases, the impact is positive, e.g., around 30% of heavy oil in the Bolivar Coastal Field in Venezuela is produced by reservoir compaction. But in most cases, the impacts are negative. Significant surface subsidence often causes extremely expensive damage, e.g., well failure [*van der Kooij*, 1997], gas leakage and seismicity [*Katz et al.*, 1994], and platform sinking [*Piau*, 1994].

1.3 Observation of Subsidence by InSAR

Differential Synthetic Aperture Radar interferometry (differential InSAR) is a newly emerged technique that can measure the surface movement at the precision of centimeter or even millimeter level with high-resolution over a large area. This brings the possibility of using InSAR technique to track the land subsidence during production, and hence help monitoring the entire production process.

Synthetic Aperture Radar (SAR) is a microwave-coherent imaging system that has day, night and all-weather capabilities. In repeat-pass SAR interferometry, or InSAR, two SAR datasets of the same area acquired from almost identical perspective are co-registered and combined into a so-called interferogram. Using InSAR technique, a detailed and accurate 3-D relief map of the earth's surface can be produced [Zebker *et al.*, 1994].

An extension of the basic InSAR technique, denoted “differential InSAR” since the phase measurement of interest results from the difference of two interferograms, allows the detection of very small (cm, mm level) movement of land surface features. The power of the differential InSAR lies in its capability of providing the high-resolution and large area coverage with an almost unprecedented accuracy [Zebker *et al.*, 1994, Carnec, 1995, Coulson, 1997 and van der Kooij, 1997].

The principle of differential InSAR is fairly straightforward. A microwave sensor, which can be on board a spacecraft, passes a spot on the ground and takes a “shot” of the spot. After a certain period, the same sensor passes the same spot again and takes a second “shot” (Figure 1.4). By comparing the two shots as well as a reference elevation map of the area, a detailed surface deformation map can be obtained for the period between the two passes of the sensor.

A number of space agencies collect SAR data at a regular basis. For example, European Space Agency (ESA) operates the ERS-1, ERS-2 satellites, which collect high quality SAR data for any point on earth approximately every 35 days.

In the last decade, differential InSAR received more and more attentions from researchers in a number of scientific areas. Gabriel *et al.* [1989] applied the technique to agricultural fields and mapped the changes in surface elevation over a large area to cm-

level sensitivities. The technique is also applied in the area of earthquake study. For example, the pre-, post-, and co-seismic displacements fields caused by the 1992 Landers earthquake, California has been successfully produced which agree quite well with measurements with traditional techniques [Massonet *et al.*, 1993, 1998 and Zebker *et al.*, 1994].

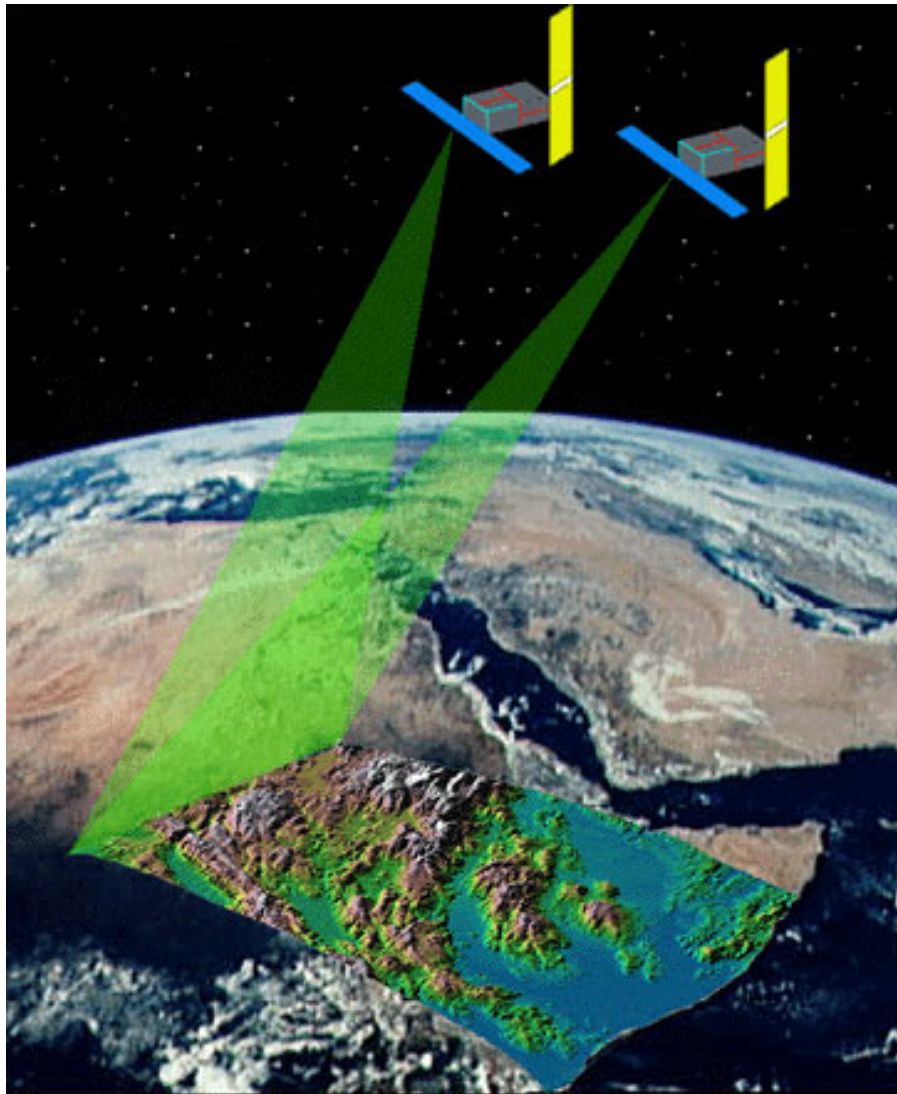


Figure 1.4: Principle of differential InSAR for measuring surface deformation (from http://www-star.stanford.edu/sar_group).

The success of mapping small changes in the contexts of biological studies and earthquake studies open up the possibility of applying the same technique to the monitoring of the surface subsidence accompanying oil and gas production. For example,

van der Kooij [1997] detected a subsidence rate as high as 30-40 *cm* per year at the Belridge oil fields, California using the differential InSAR technique. *Fielding et al.* [1998] observed similar results using differential InSAR.

Traditional measurements of land subsidence are made by detailed surveying and tide gauges. Recently, GPS surveys and tiltmeters have been used. All these techniques have the following disadvantages: (1) measure changes in locations of a limited set of benchmarks; (2) require a large number of individual observations to map the subsidence distribution; (3) require ground access; and (4) are generally costly to acquire. Differential InSAR technique, in contrast, can provide a geographically comprehensive map of the deformation, with a sampling rate far denser than the most detailed surveys. Comparing to traditional techniques such as tide gauge and GPS measurements, the most desirable advantage of differential InSAR is its capability to measure surface deformation at very high horizontal resolution (a typical grid can be 30 *m* x 30 *m*) and with very high vertical accuracy (1 *cm* or even 1 *mm* of surface deformation). Therefore, differential InSAR is the leading candidate for monitoring subsidence from oil production. In the following of this thesis, we will use “InSAR” for “differential InSAR” to save space.

1.4 Inversion

Figure 1.5 illustrates the dual-relationship between pore pressure depletion inside the reservoir and subsidence on the surface. Mathematically, it can be expressed as:

$$u(\bar{x}, t) = \frac{\alpha(1-2\nu)}{2\mu\pi(1-\nu)} \int_{dV} \Delta p(V, t) g(\bar{x}, V) dV \quad (1)$$

Where u is surface subsidence, p is pore pressure, g is the Green’s function, α is the Biot’s coefficient, μ is the shear modulus, and ν is the Poisson’s ratio. That is, the surface subsidence is proportional to the integration of the product of pore pressure drop distribution and the Green’s function. More detail will be presented in Chapter 2.

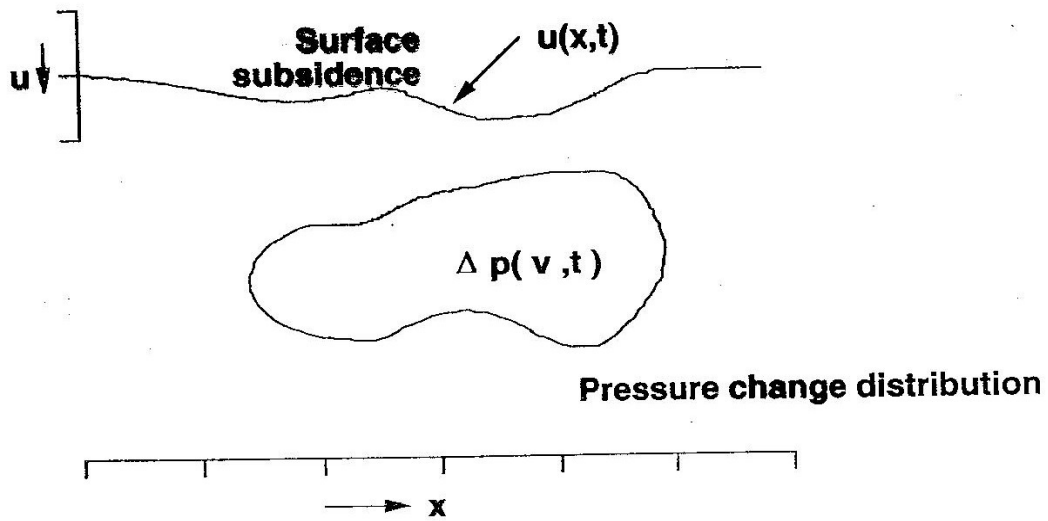


Figure 1.5: Integral inversion yields subsurface pressure distribution from surface deformation (from Nur, personal communication).

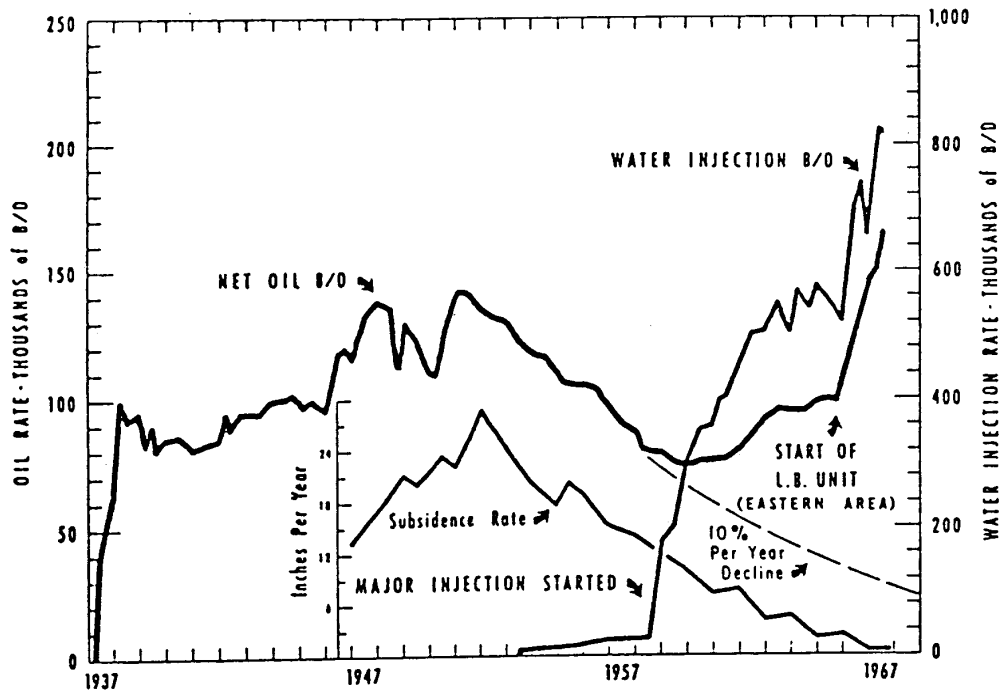


Figure 1.6: Correlation between subsidence and production/injection in the Wilmington oil field, California, during a period of 30 years between 1937 and 1967 (from Colazas & Strehle, 1995).

The correlation between surface subsidence and pore pressure drop is observed in many oil fields. Figure 1.6 shows the subsidence rate, production rate, and injection rate in the Wilmington oil field over an interval of 30 years between 1937 and 1967. Before the injection program started, subsidence rate and production rate correlated with each other. After the injection program started, although there was an increase in production, subsidence rate declined. This demonstrates that subsidence is proportional to the difference of production minus injection, or in other words, the net production. It suggests that subsidence is most likely proportional to the pore pressure drop.

Equation (1) is a forward problem, which states that subsidence is merely the surface imprint of reservoir pressure depletion. Therefore, it is possible to use this equation to invert pore pressure changes from surface subsidence.

1.5 Monitoring of Surface Subsidence

In reservoir monitoring, the mainstream approach is using repeat seismic surveys (4D seismic). Repeat seismic surveys have the advantage of high resolution and high accuracy. However, it is very expensive and time consuming.

It is important to explore alternate or supplemental approaches in reservoir monitoring. For example, *Ushijima et al.* [1999] studied how to use a 4-D electrical technique for reservoir monitoring.

In this thesis, we will show how to use InSAR measured surface subsidence as a reservoir monitoring tool. Subsidence can be used both as a stand-alone monitoring tool, and as an additional input/constraint to the traditional 4D seismic monitoring tool. Compared to 4-D seismic, monitoring reservoir dynamics by using InSAR measured surface subsidence has the advantage of low cost and all time availability.

1.6 Previous Research Activities in Compaction and Subsidence

Two of the most extensive efforts in studying hydrocarbon production induced subsidence are Phillips' work in the Ekofisk field in the North Sea, and Shell's work in

the Belridge field in the Southern California. Tables 1.2 and 1.3 list a few publications by researchers from the two companies on the two fields.

Table 1.2: Phillips: at Ekofisk oil field.

Year	Author	Title
1972	Raghavan	A review of the consolidation and rebound processes in one dimensional porous columns
1988	<i>Boade, Chin, Siemers</i>	Forecasting of Ekofisk reservoir compaction and subsidence by numerical simulation
1994	<i>Prebost, Chin</i>	A constitutive model for simulating reservoir compaction under a constrained stress path that leads to high shear
1998a	<i>Chin, Raghavan, Thomas</i>	Fully coupled analysis of well responses in stress-sensitive reservoirs
1998b	<i>Chin, Raghavan, Thomas</i>	Fully-coupled geomechanics and fluid-flow analysis of wells with stress-dependent permeability
1999	<i>Chin, Thomas</i>	Fully coupled analysis of improved oil recovery by reservoir compaction

Table 1.3: Shell: at Belridge oil field.

Year	Author	Title
1986	Hansen, Purcell	Earth stress measurements in the south Belridge oil field, kern county, California
1988	<i>Schwartz</i>	Characterizing the lithology, petrophysical properties, and depositional setting of the Belridge diatomite, South Belridge field, Kern County, California
1990	<i>Bowersox, Shore</i>	Reservoir compaction of the Belridge Diatomite and surface subsidence, South Belridge field, Kern County, California
1993	<i>Hansen, Prats, Chan</i>	Finite-element modeling of depletion-induced reservoir compaction and surface subsidence in the South Belridge oil field, California
1995	<i>Hansen, Prats, Chan</i>	Modeling of reservoir compaction and surface subsidence at South Belridge
1995	<i>De Rouffignac, Bondor, Karanikas, Hara</i>	Subsidence and well failure in the South Belridge diatomite field
1996	<i>Fredrich, Arguello, Thorne, Wawersik, Deltrick, Rouffignac, Myer, Bruno</i>	Three-dimensional geomechanical simulation of reservoir compaction and implications for well failures in the Belridge diatomite
1998	<i>Biegert, Berry, Oakley</i>	Oil field subsidence monitoring using spaceborne interferometric SAR --- a Belridge 4-D case history

The USGS maintains an extensive research effort in surface subsidence, but focuses on those caused by groundwater withdrawal. One of the earliest pioneers in USGS studying subsidence was Joseph Poland (Figure 1.1). Figures 1.7 and 1.8 are the book covers for two USGS subsidence interest group conferences.



Figure 1.7: USGS subsidence interest group conference (from the Internet).

Subsidence caused by groundwater withdrawal and hydrocarbon production have certain similarities, but they occur in distinct geologic environments. Groundwater withdrawal for civil and industrial usage usually takes place at shallow depth, where the

porous media are soil or soft rocks. These media are characterized by large porosity and permeability. Hydrocarbon production usually takes place at greater depth, where the porous media are consolidated or unconsolidated rocks. These media are usually characterized by smaller porosity and permeability than those at shallower depth. The pressure and temperature at greater depth are also much larger. The geological structures at greater depth are also often more complicated. Additionally, direct measurements of compaction and related parameters are easier to conduct at shallower depth.

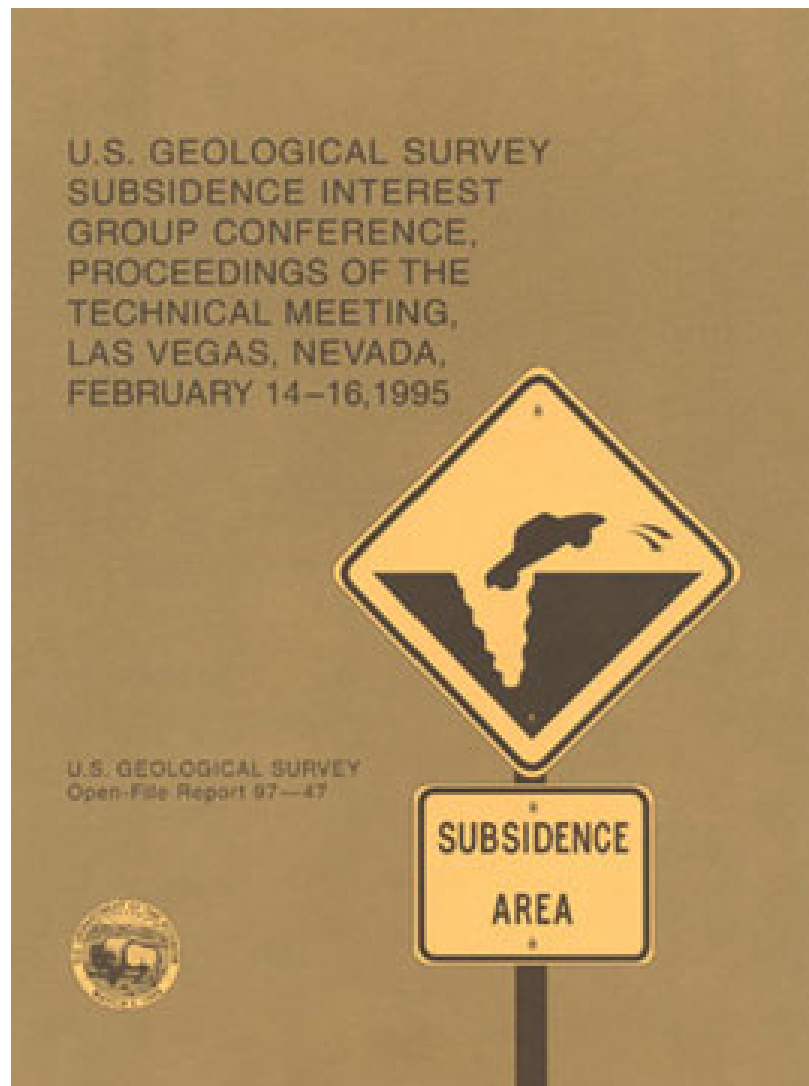


Figure 1.8: USGS subsidence interest group conference (from the Internet).

1.7 Ultimate Potentials of the Petroleum Applications of InSAR

There are both technology and business drives that motivate this research in reservoir compaction and surface subsidence, using InSAR measurements and numerical modeling.

Business drive: there are four major implications of reservoir compaction and surface subsidence on the economic performance of a reservoir:

1. Reservoir compaction and surface subsidence are very common geohazards. They may result in well failure and platform sinking, which are very costly to repair. To reduce the financial loss due to compaction and subsidence, it is important to characterize and predict them through field observation and numerical modeling.
2. For oil/gas fields located at low surface level, subsidence may pose severe environmental problems. For example, the subsidence occurred surrounding Lake Maracaibo causes the risk of water flooding from the lake. Another example is Groningen gas fields in the Netherlands, where the Earth surface level ($-1 \sim 2 \text{ m}$) in some location is already below the sea level.
3. Porosity loss as a result of reservoir compaction may have a significant impact on the calculation of reserves. For example, for a reservoir with original porosity of 30%, an absolute porosity loss of 6% represents 20% decrease of reserves.
4. In some low-pressure reservoirs, such as the heavy oil fields at Lake Maracaibo, Venezuela, reservoir compaction is a major drive mechanism for petroleum production.

Technology drive: reservoir compaction and surface subsidence have important potential applications in reservoir characterization and monitoring. Traditionally, reservoir monitoring is carried out through 4D seismic. In this thesis, we ask ourselves the following questions: (1) What can InSAR do less costly than 4D seismic can do? (2) What can InSAR do that 4D seismic cannot do? (3) What can “InSAR + 4D seismic” do that 4D seismic cannot do? Our major findings are the following:

1. For the traditional “geomechanics + flow simulation” workflow of subsidence prediction, InSAR provides massive data for validation. Previously, those

types of predictions can only be validated at few points where geodetic survey data are available. In Chapter 3, we present an example in the Belridge and Lost Hills fields where such massive subsidence distribution data are obtained from InSAR.

2. InSAR can be used as a stand-alone tool for reservoir characterization and monitoring:
 - The magnitude and patterns of subsidence are often good indications of reservoir shape, size and depth, besides being affected by reservoir rock and fluid properties and production history. In Chapter 3, we show that the large subsidence in Lost Hills compared to that of Belridge, is caused by its shallow reservoir depth, large reservoir thickness, and large reservoir rock compressibility, albeit Lost Hills has a much smaller production volume than Belridge. We also suggest that the asymmetry of subsidence in the Lost Hills field is caused by the asymmetric distribution of production volume inside the field.
 - Subsidence pattern may also be a good indication of permeability anisotropy. In Chapter 4, we perform numerical simulations for an imaginary reservoir that is homogeneous and isotropic except that the permeability may be anisotropic. We perform numerical simulations for different combinations of permeability anisotropy and boundary conditions. We find that subsidence pattern is affected by both factors. Since we often have fairly good knowledge about the tectonic settings and boundaries of a reservoir from geology, using subsidence from InSAR, we may be able to infer information about permeability anisotropy, which is otherwise very difficult to obtain.
 - Finally, subsidence pattern may be an indication of bypassed oil. For shallow reservoirs, if the compaction heterogeneity is not elastically blurred when expressed at the surface, it is hopeful to identify bypassed oil from the pattern of subsidence.
3. InSAR can also be used together with 4D seismic for reservoir monitoring. In a realistic producing reservoir, compaction and seismic velocity changes often coexist. However, traditionally, reservoir compaction and 4D seismic have been treated as two separate technical areas, the former by geomechanics and

the latter by seismic imaging. Rock physics that treats rock in its entirety provides a natural link between seismic attributes, reservoir properties and conditions. In this thesis, we study both the geomechanical mechanism and the seismic response of reservoir compaction, and demonstrate the implications it has upon reservoir characterization and monitoring:

- Traditionally, 4D seismic changes are interpreted in terms of pressure and saturation changes in the reservoir, while porosity is assumed to be constant during production. This is often inaccurate or incorrect. By using compaction as an additional input/constraint, we can improve the accuracy of 4D seismic interpretations. In Chapter 5, we will show how to integrate 4D seismic and geomechanics, to interpret 4D seismic signatures in terms of not only pressure and saturation changes, but also porosity changes.
- As we show in Chapter 5, using 4D seismic and geomechanics, we can predict porosity loss in a reservoir. On the other hand, this porosity loss in the reservoir is related to surface subsidence. If we know how the two are related, then the surface subsidence from InSAR can be used as an independent source for checking the validity of the porosity loss prediction from 4D seismic. In Chapter 3, we will show the relationship between absolute volume loss on the ground (subsidence) and the absolute volume loss in the reservoir (compaction, or porosity loss). This relationship provides a way to calculate porosity loss from surface subsidence, and hence provides an integral constraint on the 4D seismic prediction of porosity loss.

1.8 Description of Thesis Chapters

In this thesis, we present the observation, modeling, and implications of production-induced reservoir compaction and surface subsidence, using differential InSAR, reservoir simulation, and rock physics. The thesis includes 5 chapters. The chapters are:

Chapter 1: Introduction to production-induced reservoir compaction and surface subsidence. We review the phenomenon, observation, modeling, inversion, and monitoring of surface subsidence. We describe in detail the new technique of InSAR for

measuring surface subsidence, and discuss the ultimate potentials of InSAR for petroleum applications.

Chapter 2: Biot's linear quasi-static poroelasticity theory, as applied to the modeling of reservoir compaction and surface subsidence. We compare the original formulation with a few simplified forms of the Biot's theory. We also present a simplified form of the Biot's theory for "disk-shaped" reservoirs, which is used in Chapter 3.

Chapter 3: InSAR measurement of production-induced surface subsidence in Belridge and Lost Hills oil fields, California, and numerical modeling that relates observed subsidence to reservoir production history. We develop a method for calculating the "volume loss ratio", which is the ratio of absolute volume loss on the ground (subsidence) to the absolute volume loss in the reservoir (compaction). We discuss the implications of InSAR in reservoir monitoring.

Chapter 4: Investigation of the relationship between reservoir compaction and reservoir properties, through reservoir simulation. We show the combined effect of permeability anisotropy and boundary conditions on the geometric patterns of resulting surface subsidence. We demonstrate through an example that, in principle, InSAR can be used as a stand-alone tool for reservoir monitoring.

Chapter 5: Investigation of 4D seismic response to reservoir compaction, using published Laboratory pressure-porosity and pressure-velocity data. We used laboratory measurements of porosity, pressure, and velocity on hand-made clay-sand mixtures. Through this example, we demonstrate that by combining 4D seismic and geomechanics, we can predict porosity loss in a reservoir due to production. This prediction can be constrained by InSAR measured subsidence, using the "volume loss ratio" we developed in Chapter 3.

1.9 References

- Barends, F.B.J., Brouwer F.J.J., and Schroder, F.H., 1995, *Land Subsidence*, A.A.Balkema, Rotterdam.
- Biegert, E., Berry, J., and Oakley, S., 1998, Oil field subsidence monitoring using spaceborne interferometric SAR --- a Belridge 4-D case history, from the Internet at

- http://www.atlsci.com/library/Oil_field_Subsidence_Monitoring_using_Spaceborne_Interferometric_SAR.html
- Boade, R., Chin, L., and Siemers, S., 1988, Forecasting of Ekofisk reservoir compaction and subsidence by numerical simulation, 20th *Offshore Technology Conference*, Houston, Texas.
- Bowersox, J.R., and R.A. Shore, 1990, Reservoir compaction of the Belridge diatomite and surface subsidence, South Belridge field, Kern County, California, in *Structure, Stratigraphy and hydrocarbon occurrence of the San Joaquin Basin, California*, edited by J.G.Knespert, and S.A.Reid, Pacific Sections of the S.E.P.M and A.A.P.G., Bakersfield, CA, pp. 225-230.
- Brighenti, G., Borgia, G.C. and Mesini, E., 1995, Subsidence studies in Italy, in *Subsidence due to fluid withdrawal*, edited by Chilingarian et al., Elsevier Science, pp. 215-284
- Carnec, C., et al., 1995, Measurement of land subsidence by means of differential S.A.R. interferometry, in *Land subsidence*, edited by F.B.J.Barends et al., A.A.Balkema, Rotterdam, pp. 139-148
- Chin, L, Raghavan, R., and Thomas, L, 1998a, Fully coupled analysis of well responses in stress-sensitive reservoirs, *SPE 48967*.
- Chin, L, Raghavan, R., and Thomas, L, 1998b, Fully-coupled geomechanics and fluid-flow analysis of wells with stress-dependent permeability, *SPE 48857*.
- Chin, L, and Thomas, L, 1999, Fully coupled analysis of improved oil recovery by reservoir compaction, *SPE 56753*.
- Colazas, X.C. and Strehle, R.W., 1995, Subsidence in the Wilmington oil field, Long Beach, California, USA: in *Subsidence due to fluid withdrawal*, edited by G.V. Chilingarian et al., Elsevier Science, pp. 285-336
- Coulson, S.N., 1997, SAR interferometry with ERS, *the third ESA ERS symposium*, Florence, Italy. See <http://jupiter.esrin.esa.it/pub/florence>
- De Rouffignac, E.P., P.L.Bondor, J.M.Karanikas, and S.K.Hara, 1995, Subsidence and well failure in the South Belridge diatomite field, *SPE 29626*, pp.153-167.
- Fielding, E.J., Blom, R.G. and Goldstein, R.M., 1998, Rapid subsidence over oil fields measured by SAR interferometry, *Geophysical Research Letters*, vol. 25, no. 17, pp. 3215-3218
- Fredrich, J., Arguello, J., Thorne, B., Wawersik, W., Deitrick, G., De Rouffignac, E., Myer, L., Bruno, M., 1996, Three-dimensional geomechanical simulation of reservoir compaction and implications for well failures in the Belridge diatomite, *SPE 36698*.
- Gabriel, A.G., Goldstein, R.M., and Zebker, H.A., 1989, Mapping small elevation changes over large areas: differential radar interferometry, *J. Geophys. R.*, 94, pp. 9183-9191.

- Hansen, K., Prats, M., and Chan, C., 1993, Finite-element modeling of depletion-induced reservoir compaction and surface subsidence in the South Belridge oil field, California, *SPE* 26074.
- Hansen, K., Prats, M., and Chan, C., 1995, Modeling of reservoir compaction and surface subsidence at South Belridge, *SPEPF* (Aug 1995), pp. 134-143.
- Hansen, K., and Purcell, W., 1986, Earth stress measurements in the South Belridge oil field, Kern County, California, *SPE* 15641.
- Katz, S.A., Khilyuk, L.F. and Chilingarian, G.V., 1994, Interrelationships among subsidence owing to fluid withdrawal, gas migration to the surface and seismic activity: Environmental aspects of oil production in seismically-active areas. *J. Pet. Sci. Eng.*, 11, pp. 103-112.
- Leal, J., Murria, J. and Pedroza, M., 1995, Recent developments in subsidence monitoring and prediction in the Costa Oriental oil fields, Venezuela: in *Land subsidence*, edited by F.B.J.Barends et al., A.A.Balkema, Rotterdam, pp. 179-186.
- Massonet, D., et al, 1993, The displacement field of the Landers earthquake mapped by Radar interferometry. *Nature*, 364, pp.138-142.
- Massonet, D. and Feigl, K., 1998, Radar interferometry and its application to changes in the earth's surface, *Review of Geophysics*, vol. 36, no. 4, pp. 441-500.
- Piau, J-M., 1994, Compaction and subsidence of petroleum reservoirs, in *Mechanics of porous media*, edited by P. Charlez, A.A. Balkema, pp. 215-244.
- Poland, J.F. (chairman and editor), 1984, *Guidebook to studies of land subsidence due to groundwater withdrawal, prepare for the international hydrological programme*, working group 8.4, UNESCO.
- Prebost, J., and Chin, L., 1994, A constitutive model for simulating reservoir compaction under a constrained stress path that leads to high shear, in *Computer methods and advances in Geomechanics*, edited by Siriwardane & Zaman, A.A. Balkema, Rotterdam.
- Raghavan, R., 1972, A review of the consolidation and rebound processes in one dimensional porous columns, *SPE* 4078.
- Shwartz, D., 1988, Characterizing the lithology, petrophysical properties, and depositional setting of the Belridge Diatomite, South Belridge field, Kern County, California, in *Studies of the Geology of the San Joaquin Basin*, Edited by S.A.Graham, Pacific Section S.E.P.M., vol. 60, pp 281-301.
- Sulak, R.M., 1991, Ekofisk: the first 20 years, *J. Pet. Technol.*, 43(10): pp. 1265-1271.
- Ushijima, K., Mizunaga, H., and Tanaka, T., 1999, Reservoir monitoring by a 4-D electrical technique, *The leading edge*, December 1999.

Van der Kooij, M., 1997, Land subsidence measurements at the Belridge oil fields from ERS InSAR data, in the third ESA ERS symposium, Florence, Italy, at <http://earth1.esrin.esa.it/florence/papers/data/vanderkooij1/index.html>.

Zebker, H. A., P.A. Rosen, R.M.Goldstein, A.Gabriel, and C.L.Werner, 1994, On the derivation of coseismic displacement fields using differential radar interferometry: the Landers earthquake, *J. Geophys. R.*, (99) B10, pp. 19,617-19,634.

Chapter 2

Biot's Linear Quasi-Static Isotropic Poroelasticity

2.1 Abstract

In this chapter, we review the formulation of Biot's linear isotropic quasi-static poroelasticity theory, which is the theoretical basis for numerical simulation of reservoir compaction and surface subsidence in poroelastic media. We also compare the original formulation of the Biot theory with a few of its simplified forms. One of the simplified forms is frequently used for reservoir simulation. Finally, we present *Segall's* [1992] result on production-induced surface deformation for axisymmetric reservoirs. This result can be further simplified for disk-shaped reservoirs, which will be used in Chapter 3.

2.2 The Mechanical Description

This and the following two sections give a brief presentation of the formulation of Biot's linearized quasi-static isotropic poroelasticity. For a complete discussion, we refer the reader to the original paper by *Biot* [1941], the reformulation by *Rice & Cleary* [1976], and the review paper by *Detournay & Cheng* [1993]. Here we follow the notations used in *Detournay & Cheng* [1993]. The reader is also referred to the PoroNet website (<http://www.ce.udel.edu/faculty/cheng/poronet/>) for more references on poroelasticity.

The Biot theory of a fluid-filled porous material is constructed on the conceptual model of a coherent solid skeleton and a freely moving pore fluid. There are two underlying assumptions: (1) the medium is a continuum; (2) both the solid and fluid phases are fully connected. Consistent with the classical continuum approach, any quantity that appears in the theory is taken to be averaged over a certain length scale l . This length scale l , which underpins the continuum model, is assumed to be large with

respect to the length scale of the microstructure, yet small enough to allow the introduction of genuine macroscopic scale material heterogeneity.

The mechanical description of such material includes two sets of quantities --- “variables” and “parameters”, which we will discuss in detail below.

2.2.1 “Variables” in the Biot Theory

The first step to formulate the theory of a porous rock is to define some basic kinematic and dynamic quantities to describe a fluid-filled porous rock. These quantities are independent of the exact properties of rock. In the next section, we will present the formulas that link those kinematic and dynamic quantities together, which characterize the material properties of that rock.

Table 2.1 is an attempt to group into different categories the set of basic kinematic and dynamic quantities that describe a porous rock. Individual definitions of these variables are given in Table 2.2. It has to be pointed out that the grouping is rather for convenience than being strict in physical nature. For example, the displacement vector u in the table really describes the composite porous material and not only the solid frame, and γ (external source --- production or injection wells) is typically not considered “strain”. However, this grouping does bring some convenience as will be demonstrated later. Notice that the displacement-type quantities and strain-type quantities are closely related by a compatibility equation (for “solid”) and a fluid mass balance equation (for “fluid”):

$$\varepsilon_{ij} = \frac{1}{2}(u_{i,j} + u_{j,i}) \quad (1)$$

$$\frac{\partial \zeta}{\partial t} + q_{i,i} = \gamma \quad (2)$$

Also notice that (σ_{ij}, p) are conjugates of $(\varepsilon_{ij}, \zeta)$ in that the work increment associated with strain increment $d\varepsilon_{ij}$, $d\zeta$ in the presence of σ_{ij} , p equals the work increment associated with stress increment $d\sigma_{ij}$, dp in the presence of ε_{ij} , ζ :

$$dw = \sigma_{ij} d\varepsilon_{ij} + p d\zeta = \varepsilon_{ij} d\sigma_{ij} + \zeta dp \tag{3}$$

Finally in the Biot model, the descriptions of stress (p) and strain (ζ) in the fluid are both scalars, thus it is limited to their isotropic component. For example, shear on the solid-fluid contact is ignored. This restricts the time scale to be long (quasi-static).

Table 2.1: Basic kinematic and dynamic quantities that describe a porous rock.

	Solid		Fluid	
	Internal	External	Internal	External
Displacement-type	u_i displacement		q_i fluid discharge	
Strain-type	ε_{ij} small strain		ζ fluid content	γ external fluid source
Stress-type	σ_{ij} stress	F_i body force on solid	p pore pressure	f_i body force on fluid

Table 2.2: “Variables” in the Biot theory.

Symbol	Unit	Definition	Comment
u_i	m	solid displacement vector --- with respect to a reference configuration	
q_i	m/s	specific discharge vector --- motion of fluid relative to solid. It is the rate of fluid volume crossing a unit area of porous solid in $+x_i$ direction	
ε_{ij}	<i>dimensionless</i>	small strain tensor	+ is extension
ζ	<i>dimensionless</i>	variation of fluid content --- variation of fluid volume per unit volume of porous material due to diffusive fluid mass transport	+ is “gain” of fluid by the porous media
γ	bbl/day	source/sink from production/injection wells	
σ_{ij}	MPa	total stress tensor --- total force in the x_j direction per unit area whose normal is x_i direction	+ is tension
F_i	MPa	force acting on the solid	
p	MPa	pore pressure	
f_i	MPa	force acting on fluid	

2.2.2 “Parameters” in the Biot Theory

“Parameters” are quantities that characterize the properties of a reservoir, reservoir rocks, and reservoir fluids. Table 2.3 lists some important parameters.

Table 2.3: “Parameters” in the Biot theory.

reservoir geometry	dimension boundary
rock properties	moduli (rock compressibility, ...) density ρ permeability k porosity ϕ
fluid properties	moduli (fluid compressibility) density ρ viscosity μ

2.3 Formulation of Biot’s Linear Isotropic Quasi-static Poroelasticity

2.3.1 Constitutive Laws

Constitutive laws, or stress-strain relationships, determine the properties of material. In Biot’s theory, there are two assumptions for constitutive laws: (1) linearity, i.e., stresses and strains are linearly related to each other, and (2) reversibility of the deformation process, i.e., no energy is dissipated in a closed loading cycle.

We introduce the constitutive laws of poroelasticity by comparing them with the constitutive laws of elasticity (Table 2.4). In Table 2.4, to get the volumetric response formulation (*), there are a few definitions that need to be introduced. First, stress can be decomposed into volumetric and deviatoric components:

$$\sigma_{ij} = \left(\sigma_{ij} - \frac{\sigma_{kk}}{3} \delta_{ij} \right) + \frac{\sigma_{kk}}{3} \delta_{ij} = (\sigma_{ij} + P \delta_{ij}) - P \delta_{ij} = s_{ij} - P \delta_{ij} \quad (4a)$$

where s_{ij} is the deviatoric stress, $P = -\frac{\sigma_{kk}}{3}$ is the mean pressure (or negative of mean stress).

Table 2.4: Constitutive laws of elasticity and poroelasticity.

	Poroelasticity	Elasticity
Variables	$\sigma, p \text{ -- } \varepsilon, \zeta$	$\sigma \text{ -- } \varepsilon$
Independent moduli	4 independent moduli (K, G, H', R') 1 deviatoric (G) 3 volumetric (K, H', R') K is the bulk modulus, G is the shear modulus, of the dry rock. H', R' are two constants introduced by <i>Biot</i> [1941], which describe the coupling between fluid and solid (see <i>Detournay & Cheng</i> , 1993).	2 independent moduli (K, G)
Formulation	solid: volumetric + deviatoric $\varepsilon_{ij} = \frac{\sigma_{ij}}{2G} - \left(\frac{1}{6G} - \frac{1}{9K}\right)\sigma_{kk}\delta_{ij} + \frac{1}{3H'}p\delta_{ij}$ fluid: volumetric only $\zeta = \frac{\sigma_{kk}}{3H'} + \frac{p}{R'}$	solid: volumetric + deviatoric $\varepsilon_{ij} = \frac{\sigma_{ij}}{2G} - \left(\frac{1}{6G} - \frac{1}{9K}\right)\sigma_{kk}\delta_{ij}$ fluid: (no equations for fluid)
Volumetric response(*)	solid: $\varepsilon = -\left(\frac{P}{K} - \frac{p}{H'}\right)$ fluid: $\zeta = -\left(\frac{P}{H'} - \frac{p}{R'}\right)$ (poroelastic: solid-fluid coupled --- deformation of either phase depends on stress/pressure of both phases)	$\varepsilon_{\alpha\alpha} = \frac{1}{K}\sigma_0$ (in which, $\sigma_0 = \frac{1}{3}\sigma_{\alpha\alpha}$ is the mean stress)
Deviatoric response	$e_{ij} = \frac{1}{2G}s_{ij}$ (purely elastic)	$e_{ij} = \frac{1}{2G}s_{ij}$ (purely elastic)

Similarly, for strain,

$$\varepsilon_{ij} = \left(\varepsilon_{ij} - \frac{\varepsilon_{kk}}{3}\delta_{ij}\right) + \frac{\varepsilon_{kk}}{3}\delta_{ij} = \left(\varepsilon_{ij} - \frac{\varepsilon}{3}\delta_{ij}\right) + \frac{\varepsilon}{3}\delta_{ij} = e_{ij} + \frac{\varepsilon}{3}\delta_{ij} \quad (4b)$$

where e_{ij} is the deviatoric strain, ε is the volumetric strain.

The decomposition of stress and strain into volumetric and deviatoric components is displayed in Table 2.5.

Table 2.5: Stress and strain “variables”.

	Solid	Fluid
Strain type	ϵ_{ij} can be decomposed into (e_{ij}, ϵ)	ζ
Stress type	σ_{ij} can be decomposed into (s_{ij}, P)	p

2.3.2 Volumetric Responses of Poroelasticity

The volumetric responses of a poroelastic material as shown in Table 2.4 are:

$$\text{solid: } \epsilon = -\left(\frac{P}{K} - \frac{p}{H'}\right) \quad (5a)$$

$$\text{fluid: } \zeta = -\left(\frac{P}{H'} - \frac{p}{R'}\right) \quad (5b)$$

Table 2.6: Volumetric responses under drained and undrained conditions.

	General	Drained: $p=0$	Undrained: $\zeta=0$
p		$p=0$	$p=BP$
ϵ	$\epsilon = -\left(\frac{P}{K} - \frac{p}{H'}\right)$	$\epsilon = -P/K$	$\epsilon = -P/K_u$
ζ	$\zeta = -\left(\frac{P}{H'} - \frac{p}{R'}\right)$	$\zeta = \alpha\epsilon$	$\zeta=0$
Independent moduli	K, H', R'	K, K_u, α	

There are two limiting behaviors for drained and undrained conditions. For drained conditions, $p = 0$ (could be relaxed to p in equilibrium), then $\zeta = \alpha\epsilon$, in which $\alpha = K/H'$ is the Biot's coefficient. Therefore, Biot's coefficient has the physical interpretation of being the volume change ratio of fluid and porous media under drained conditions, and must be less than 1. In addition, when $p = 0$, $\epsilon = -P/K$, ϵ is proportional to P . For

undrained conditions, $\zeta = 0$, then $p = BP$, p is proportional to P , in which $B = R'/H'$ is the Skempton's coefficient. $\varepsilon = -P/K_u$, ε is proportional to P , in which $K_u = K(1 + KR'/(H'^2 - KR'))$.

It is easy to see from Table 2.6 that for both the two limiting cases, ε is proportional to P , which means they behave like elastic, with undrained being stiffer ($K_u > K$).

It is then possible to rewrite the volumetric responses using the basic set of moduli (K, K_u, α, G):

$$\text{Deviatoric: solid: } e_{ij} = \frac{1}{2G} s_{ij} \quad (6a)$$

$$\text{Volumetric: solid: } \varepsilon = -\frac{1}{K} (P - \alpha p) \quad (6b)$$

$$\text{fluid: } \zeta = -\frac{\alpha}{K} (P - \frac{p}{B}), \text{ in which } B = \frac{K_u - K}{\alpha K_u} \quad (7)$$

2.3.3 Governing Equations

The set of governing equations to describe the porous rock includes:

1) Constitutive equations:

The constitutive equations are now rewritten in terms of four independent moduli (G, α, ν, ν_u), which are the shear modulus of the dry rock; the Biot's coefficient; the drained Poisson's ratio; and the undrained Poisson's ratio, respectively.

Consider first the response for the porous solid. Selecting the pore pressure p as the coupling term yields the strain-stress relation

$$2G\varepsilon_{ij} = \sigma_{ij} - \frac{\nu}{1+\nu} \sigma_{kk} \delta_{ij} + \frac{\alpha(1-2\nu)}{1+\nu} p \delta_{ij} \quad (8a)$$

and the stress-strain relation

$$\sigma_{ij} + \alpha p \delta_{ij} = 2G\varepsilon_{ij} + \frac{2G\nu}{1-2\nu} \varepsilon \delta_{ij} \quad (8b)$$

On the other hand, if ζ is adopted as the coupling term, the constitutive equations become

$$2G(\varepsilon_{ij} - \frac{B}{3}\zeta\delta_{ij}) = \sigma_{ij} - \frac{\nu_u}{1+\nu_u}\sigma_{kk}\delta_{ij} \quad (8c)$$

$$\sigma_{ij} = 2G\varepsilon_{ij} + \frac{2G\nu_u}{1-2\nu_u}\varepsilon\delta_{ij} - \alpha M\zeta\delta_{ij} \quad (8d)$$

There are two different forms of the response for the pore fluid, depending on whether the mean stress or the volumetric strain is used as the coupling term

$$2G\zeta = \frac{\alpha(1-2\nu)}{1+\nu}(\sigma_{kk} + \frac{3}{B}p) \quad (9a)$$

$$p = M(\zeta - \alpha\varepsilon) \quad (9b)$$

Relationships between the basic set (G , α , ν , ν_u) and the extended set of moduli:

$$B = \frac{3(\nu_u - \nu)}{\alpha(1-2\nu)(1+\nu_u)} \quad (10a)$$

$$M = \frac{2G(\nu_u - \nu)}{\alpha^2(1-2\nu)(1-2\nu_u)} \quad (10b)$$

2) Darcy's law:

$$q_i = -\kappa(p_{,i} - f_i) \quad (11a)$$

In which

$$\kappa = k / \mu \quad (11b)$$

where k is the permeability of the material, and μ is the viscosity of the fluid.

3). Balance laws (solid equilibrium and fluid mass balance):

$$\sigma_{ij,j} = -F_i \quad (12)$$

$$\frac{\partial \zeta}{\partial t} + q_{i,i} = \gamma \quad (13)$$

2.3.4 Field Equations

From the above set of governing equations, through combination and reorganization, the number of variables can be reduced to form two types of very useful field equations, i.e., Navier type (displacement-type) and diffusion type (pressure-type).

Navier (displacement-type):

$$G\nabla^2 u_i + \frac{G}{1-2\nu} u_{k,ki} = \alpha p_{,i} - F_i \quad (14a)$$

$$G\nabla^2 u_i + \frac{G}{1-2\nu_u} u_{k,ki} = \alpha M \zeta_{,i} - F_i \quad (14b)$$

Diffusion (pressure-type):

$$\frac{\partial p}{\partial t} - \kappa M \nabla^2 p = -\alpha M \frac{\partial \varepsilon}{\partial t} + M(\gamma - \kappa f_{i,i}) \quad (15a)$$

$$\frac{\partial \zeta}{\partial t} - c \nabla^2 \zeta = \frac{\eta c}{G} F_{i,i} + \gamma - \kappa f_{i,i} \quad (15b)$$

Where η is the poroelastic stress coefficient:

$$\eta = \frac{\alpha(1-2\nu)}{2(1-\nu)} \quad (15c)$$


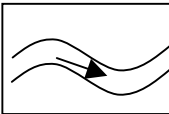
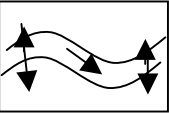
and c is the diffusivity coefficient:

$$c = \frac{2\kappa G(1-\nu)(\nu_u - \nu)}{\alpha^2(1-2\nu)^2(1-\nu_u)} \quad (15d)$$

2.4 Comparisons Among Several Formulations

In this section, the formulations of elasticity, reservoir simulation (here we only discuss traditional reservoir simulation such as presented in *Aziz & Settari, 1979*), and static poroelasticity are compared. The keys for comparison are: (1) differences in “variables” determine differences in coupling. For example, elasticity couples (σ, ϵ) , poroelasticity couples $(\sigma, p, \epsilon, \zeta)$, reservoir simulation couples (p, ζ) . (2) differences in “parameters” determines material properties. For example, heterogeneity ($k = k(x,y,z)$), anisotropy ($k_x \neq k_y$), and nonlinearity ($k = k(p)$).

Table 2.7: Some common situations and the theory commonly used corresponding to those situations.

Illustration	Situation	Description of material
	earthquake waves in the Crust	elastic solid
	hydrogeology, geochemistry, reservoir simulation	porous medium through which fluids flow
	reservoir simulation in stress-sensitive reservoirs	a coupled poroelastic or thermoporoelastic system

In physical sciences, materials are often described using simplified models. Common models that we use include: (1) non-deformable objects such as a mass point or a rigid body. (2) deformable objects, which include solid, fluid (no resistance to shear), and porous material. Behavior of a solid is sometimes described by elasticity. Behavior of a

fluid is described using fluid mechanics. Behavior of a porous material may be described by poroelasticity. Reservoir simulation uses a simplified poroelastic model to describe the reservoir.

2.4.1 Elastic and Poroelastic Formulations

We have compared the equations of elasticity and poroelasticity in a previous section. Here we investigate them in more detail. An equation for linear poroelasticity is

$$2G\varepsilon_{ij} = \sigma_{ij} - \frac{\nu}{1+\nu}\sigma_{kk}\delta_{ij} + \frac{\alpha(1-2\nu)}{1+\nu}p\delta_{ij} \quad (16)$$

It is easy to identify that the extra term in Equation (16), compared to elasticity, is the fluid pressure term p .

The poroelasticity theory was developed from soil consolidation (Terzaghi) and rock deformation (Biot). There are two parts of a porous material: the solid part and the fluid part. Therefore, the porous material theory should be related equally to both the theory of solids (e.g., elasticity) and the theory of fluids (e.g., fluid mechanics). However, for historical reasons, porous material theory is more or less considered an extension of the theory of solids, instead of an extension of the theory of fluids. It is natural, because the Earth's crust is mostly solid. Therefore as a first order approximation, it is natural to think of it as solid. Hence the fluid part --- a small fraction in the crust --- is neglected. For example, in earthquake studies, people used to only think about how fault slips and breaks. It has only been realized in recent years that fluids (the extra term " p ") play a critical role in many crustal processes [e.g., Nur, 1972].

2.4.2 Reservoir Simulation and Poroelasticity

Table 2.8 compares the formulations of poroelasticity and reservoir simulation. As an example of the derivation denoted by (**) in Table 2.8, let us consider the formulation by Aziz & Settari [1979]. For single-phase flow, the equations are (the equation numbers in the parentheses correspond to the equation numbers in the original book):

(2.5) Mass balance: $-\nabla \cdot (\rho \vec{u}) = \frac{\partial}{\partial t}(\rho \phi) + \tilde{q}$

(2.28) Darcy's law: $\vec{u} = -\frac{k}{\mu}(\nabla p - \gamma \vec{N}z)$

(2.39) Constitutive Equations (equations of state): $\rho = \rho^0(1 + c_f(p - p^0))$

(2.41) Constitutive Equations (equations of state): $\phi = \phi^0(1 + c_R(p - p^0))$

Table 2.8: Comparison between poroelasticity and reservoir simulation.

		Poroelasticity	Reservoir simulation
Governing Equations	Mass balance and solid equilibrium	Solid: $\sigma_{ij,j} = -F_i$ Fluid: $\frac{\partial \zeta}{\partial t} + q_{i,i} = \gamma$ (*1)	Solid: (no equations) Fluid: $\frac{\partial \zeta}{\partial t} + q_{i,i} = \gamma$ (*1)
	Momentum balance	Darcy's law: $q_i = -\kappa(p_{,i} - f_i)$ (*2)	Darcy's law: $q_i = -\kappa(p_{,i} - f_i)$ (*2)
	Energy balance	None if isothermal	None if isothermal
	Constitutive equations	Solid: $2G\varepsilon_{ij} = \sigma_{ij} - \frac{\nu}{1+\nu}\sigma_{kk}\delta_{ij} + \frac{\alpha(1-2\nu)}{1+\nu}p\delta_{ij}$ Fluid: $2G\zeta = \frac{\alpha(1-2\nu)}{1+\nu}(\sigma_{kk} + \frac{3}{B}p)$ (*3) therefore, $\frac{\partial}{\partial t}\zeta = f(\sigma_{kk}, p, t)$	Solid: (no equations) Fluid: $\frac{\partial \zeta}{\partial t} = f(p)$ therefore, $\frac{\partial}{\partial t}\zeta = f(p, t)$ (*3)
Field equation	Diffusion equation (*1,2,3) $\rightarrow f(\sigma_{kk}, p, \gamma) = 0$ in Rice & Cleary [1976], further combined with $\nabla^2(P + \sigma) = 0$ and obtain: $\frac{\partial m}{\partial t} = \nabla^2 m$	(*1,2,3) $\rightarrow f(p, \gamma) = 0$ (**)	

The following observations can be made from the above discussion:

(1). Compared to poroelasticity, which is a coupled system of solid-fluid, elasticity does not include the fluid, and reservoir simulation does not account sufficiently for the solid-fluid interaction (there is only one factor C_r that represents solid effect --- which is insufficient for stress sensitive reservoirs).

(2). Reservoir simulation uses the same set of governing equations as poroelasticity, but with significant simplifications. For example, in poroelasticity, (σ_{ij}, p) are 10 variables. In reservoir simulation, the solid (σ_{ij}) is not considered, and p is only 1 variable. Even if only an average σ is used in poroelasticity, the number of variables is twice that of reservoir simulation. Nevertheless, the simplification makes it possible for reservoir simulation to account for very complicated reservoir geometry, multiphase flow, well treatment, and so on. The term “coupled reservoir simulation and poroelasticity” is frequently used only because there are many mature reservoir simulation code and stress code available in the scientific community, which were developed independently.

2.5 Surface Deformation for Axisymmetric and Disk-Shaped Reservoirs

Segall [1992] developed the poroelastic solution for compaction and subsidence in axisymmetric reservoirs based on Biot’s theory of poroelasticity. *Geertsma*’s solution [1973] for disk-shaped reservoir with uniform pressure drop was recovered as a special case. In the following we present *Segall*’s results.

Segall derived with *Biot*’s constitutive equations (Equations 8a, 9a) for a linear poroelastic medium, assuming material isotropy. For axisymmetric configurations, he found that the deformation for an arbitrary radial pressure distribution is:

$$u_i(r, z) = \frac{\alpha}{\mu} \int_0^\infty \int_0^\infty p(\rho, d) g_i(r, z; \rho, d) d\rho dd \quad (17)$$

In which p is the pore pressure drop, and g is the Green’s function. Equation (17) can be further simplified for uniform pressure drop in a disk-shaped reservoir, as published

earlier by *Geertsma* [1973], which we will use in Chapter 3. We will discuss in more detail *Geertsma*'s formula in the next chapter.

2.6 Conclusions

In this chapter, we investigated in detail the formulation of Biot's linearized quasi-static poroelasticity, which is often used to describe the stress-strain behavior of rocks and reservoirs. We compared the original formulation of the Biot theory with a few of its simplified forms. One of the simplified forms is frequently used for reservoir simulation. We also presented a solution to Biot's formulation for axisymmetric reservoirs. This form will be used in the next chapter.

2.7 References

- Aziz, K. and Settari, A., 1979, *Petroleum reservoir simulation*, Applied science publishers ltd.
- Biot, M.A., 1941, General theory of three-dimensional consolidation, *Journal of Applied Physics*, vol. 12, pp. 155-164.
- Detournay, E. and Cheng, A.H-D., 1993, fundamentals of poroelasticity, in *Comprehensive rock engineering --- Principles, practice and projects, volume 2, Analysis and design methods*, edited by J.A. Hudson, Pergamon press, pp. 113-172.
- Geertsma, J., 1973, Land subsidence above compacting oil and gas reservoirs, *Journal of Pet. Tech.*, pp. 734-744.
- Nur, A., 1972, Aftershocks caused by pore fluid flow? *Science*, vol. 175, pp. 885-887.
- Rice, J.R. and Cleary, M.P., 1976, Some basic stress diffusion solutions for fluid-saturated elastic porous media with compressible constituents, *Review of Geophysics and Space Physics*, vol.14, no.2, pp. 227-241.
- Segall, P., 1992, Induced stresses due to fluid extraction from axisymmetric reservoirs: *Pure and applied geophysics*, 139, pp. 535-560.

Chapter 3

Production-Induced Surface Subsidence in the Belridge / Lost Hills Oil Fields, Measured by InSAR

3.1 Abstract

Land subsidence over the Belridge and Lost Hills oil fields, California, was measured using spaceborne Interferometric Synthetic Aperture Radar (InSAR). During the 105-day period between November 5, 1995 and February 17, 1996, the subsidence in the center of the Lost Hills field reached 15 *cm*. We assume that this surface subsidence resulted from the vertical shrinkage of the reservoir, which in turn was due to oil production and the resulting pore pressure drop. We model this mechanical effect using an elastic deformation theoretical solution with input constants taken from relevant experiments. The modeled surface deformation matches the InSAR measured values. This result indicates that it is possible, in principle, to monitor hydrocarbon production using satellite-based measurements of earth deformation. We also investigated the ratio between absolute volume loss on the surface (subsidence) and absolute volume loss in the reservoir (compaction). When both surface subsidence data and 4D seismic data are available, this volume loss ratio may be used as an integral constraint on the prediction of porosity loss from 4D seismic.

3.2 Introduction

Land subsidence above compacting oil and gas reservoirs has been observed worldwide and has significant, and often negative, effect on the field infrastructure and management. A few of the well-known cases are subsidence at Wilmington oil field, California; Groningen gas field, the Netherlands; Bolivar Coastal oil fields, Venezuela; Po Delta gas field, Italy [Barends *et al.*, 1995]. Another example is Belridge and Lost Hills oil fields, central California. In those two fields, oil production from the shallow, thick, very soft diatomite reservoirs has led to substantial surface subsidence and well failure [Bruno and Bovberg, 1992; Bowersox and Shore, 1990; Dale *et al.*, 1996]. Efforts to mitigate the effect of subsidence (e.g., via water injection) have only been partly successful because well failure persisted [Wallace and Pugh, 1993; Fast *et al.*, 1993].

In all these cases worldwide, subsidence coincides with hydrocarbon production. It is fair to assume that this subsidence is the surface imprint of the vertical shrinkage of the reservoir due to hydrocarbon withdrawal. This reservoir shrinkage may result from the increased effective stress due to pore pressure drop associated with production.

The new InSAR technique provides massive, high-precision, and real-time data of surface deformation. If this deformation is due to hydrocarbon production, the InSAR technique gives us an opportunity to monitor this production in time and space. Such monitoring is important for oil field development and management.

In this chapter we show, using the Belridge and Lost Hills field example, that such monitoring is in principle possible. We first review the geology and production history of the Belridge / Lost Hills oil fields. We then process InSAR data to obtain the subsidence in the fields during a period of 105 days. This measured subsidence is modeled using a simple theoretical solution. Finally we discuss the application of InSAR on oil field monitoring and development.

3.3 Geology and Production History of Belridge / Lost Hills Fields

Belridge and Lost Hills oil fields are located in Kern County, California, in the San Joaquin Valley (Figure 3.1). Petroleum and agriculture are the two most important economic resources in the county. In the two fields, during several decades of production, removal of fluids from the shallow, thick, low strength diatomite reservoir has led to substantial reservoir compaction, causing surface subsidence and well failure. Diatomite is often characterized by very high porosity (to 60%), high oil saturation (to 60%), and low matrix permeability (0.1 to 5 *mD*). The diatomite may be naturally fractured, but not extensively, and generally requires massive hydraulic fracture stimulation to support economic oil production [Bruno and Bovberg, 1992].

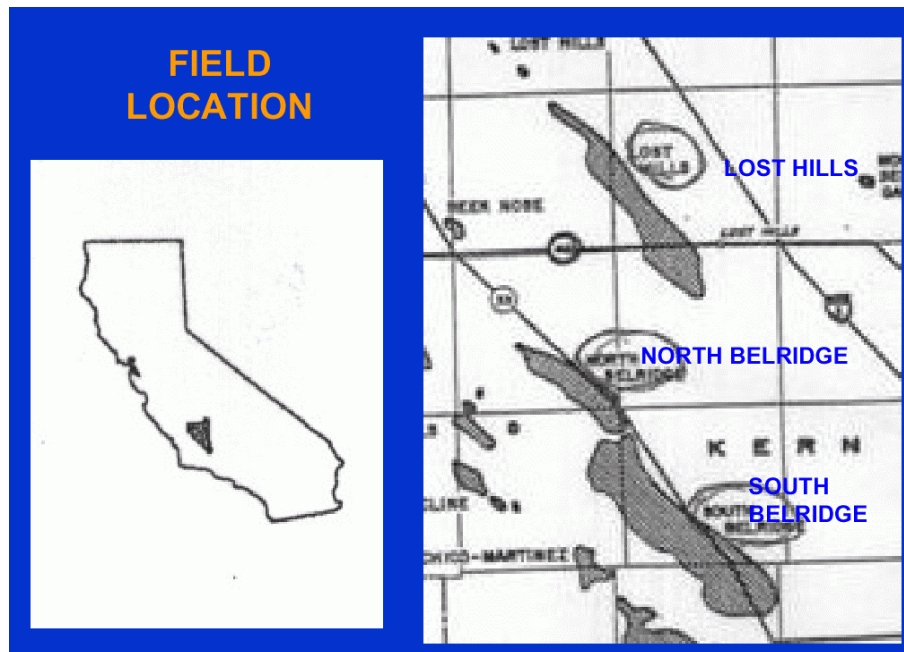


Figure 3.1: Location of Belridge and Lost Hills oil fields.

Besides Belridge and Lost Hills fields, there are a few other oil fields in the San Joaquin Valley (Table 3.1). Some of these fields are among the nation's largest oil fields. These reservoirs are characterized by relatively soft and porous formation material (such as diatomite), and relatively shallow and thick producing intervals. Reservoir compaction and surface subsidence have been associated with oil and gas production from several of these fields during the past 50 years. In the most extreme example, portions of the

Belridge field subsided more than 9 feet during the mid-1980s, resulting in damage to more than 400 wells operated by several oil companies. The surface above the Lost Hills field has been subsiding since the early 1950's, and accelerated due to expanded well development in the late 1980's [Bruno and Bovberg, 1992].

Production history is available for the Belridge and Lost Hills oil fields. Table 3.2 shows the total production in the Belridge (North and South) and Lost Hills oil fields compiled from various publications of the *California Division of Oil and Gas* (missing production data for year 1992, 1996, 1997 in the Stanford Earth Sciences library). In terms of production, the Belridge fields are much larger than the Lost Hills field.

Table 3.1: Twenty-five largest oil fields of the United States ranked by cumulative production [International Petroleum Encyclopedia, 1989].

RANK	Field Name (*San Joaquin field)	Discovery Year	State	Cumulative Production (1000 bbls)	Production in 1988 (1000 bbls)
1	Prudhoe Bay	1967	AL	6,053,018	576,335
2	East Texas	1930	TX	5,008,747	40,957
3	Wilmington	1932	CA	2,292,229	29,921
4	Midway-Sunset *	1894	CA	1,879,347	57,497
5	Wasson	1936	TX	1,711,898	28,656
6	Panhandle	1921	TX	1,423,286	7,812
7	Kelly-Snyder	1948	TX	1,234,962	11,592
8	Kern River *	1899	CA	1,204,479	46,899
9	Yates	1926	TX	1,171,820	33,540
10	Sho-Vel-Tum	1905	CK	1,167,379	18,398
11	Huntington Beach	1920	CA	1,066,368	5,816
12	Slaughter	1936	TX	1,029,800	20,364
13	Long Beach	1921	CA	909,757	2,466
14	Ventura	1919	CA	894,742	7,072
15	Elk Hills	1911	CA	893,374	39,144
16	Hawkins	1940	TX	821,644	8,244
17	Oklahoma	1928	CK	816,170	802
18	Glodsmith	1934	TX	755,516	7,248
19	Coalinga *	1890	CA	753,845	10,212
20	Tom O'Connor	1934	TX	747,848	10,380
21	Conroe	1931	TX	727,215	3,864
22	Hastings	1934	TX	697,237	3,084
23	South Belridge *	1911	CA	677,083	60,583
24	Spraberry Trend	1951	TX	653,388	22,212
25	Buena Vista *	1909	CA	647,274	1,574
San Joaquin Valley Fields Only *				6,055,402	215,909
California Fields Only				11,218,498	261,184

Table 3.2: Production history of Belridge and Lost Hills oil fields (bbl).

Year	North Belridge	South Belridge	Lost Hills
1984	1,090,000	46,400,000	5,190,000
1988	3,650,000	60,300,000	5,600,000
1989	2,590,000	56,800,000	6,010,000
1990	2,840,000	54,700,000	6,640,000
1991	2,730,000	55,300,000	8,000,000
1993	2,180,000	46,700,000	10,200,000
1994	2,070,000	43,800,000	12,800,000
1995	2,010,000	41,600,000	12,000,000
1998	2,120,000	43,500,000	11,500,000

Table 3.3: Key parameters for diatomite formation.

	North Belridge	South Belridge	Lost Hills
Geometrical properties			
size	4 x 0.8 mile	9.5 x 1.5 mile	12 x 1 mile
thickness	1320 ft	500 ft	1000 ft
average depth	2200 ft	1000 ft	300 ft
Reservoir properties			
rock compressibility of producing formations	~ 20 % production from diatomite: Static Young's modulus: $E = 0.05 \text{ GPa}$ ~ 80 % production from sandstone: $E = 10 \text{ GPa}$		most from diatomite: $E = 0.05 \text{ GPa}$
porosity	45%	50%	25~45%
permeability	16~2400 mD	1.5 mD	100~2000 mD
viscosity	8 cp	5500 cp	96 cp
Production parameters			
initial reservoir pressure	500~600 psi	960 psi	50~850 psi
production in 70 days in 1992	424,000 bbl	9,081,000 bbl	1,983,000 bbl

In Table 3.3 we compiled some key geologic and reservoir parameters for Belridge and Lost Hills oil fields, using published data from the *California Division of Oil and Gas*. We observe that Lost Hills field has similar geometrical size as Belridge field, similar porosity, but is shallower, thicker, and has higher permeability and lower

viscosity. Both fields have the soft diatomite as reservoir rock, however, in Belridge, a larger portion of oil are produced from stiffer sandstones.

3.4 Subsidence from InSAR

Differential Synthetic Aperture Radar Interferometry (differential InSAR) is a newly emerged technique that allows for high-precision (a centimeter range) surface deformation over large areas [Massonet *et al.*, 1993; Massonet and Feigl, 1998; Zebker *et al.*, 1994; Gabriel *et al.*, 1989; Amelung *et al.*, 1999].



Figure 3.2: Satellite intensity image of Lost Hills oil field. It is visible in the image three dark lines: the straight line on top is highway 46, the straight line to the upper right is highway 5, and the curved line is the California Aqueduct. The altitude of ERS satellite is almost 800 km above the ground, but still characteristic on the surface is clear to see.

We use two synthetic aperture radar (SAR) images acquired by the European Earth Remote-Sensing (ERS) satellites with a temporal separation of 105 days to form a change interferogram (see the description of this procedure in, e.g., *Massonet and Feigl, 1998*). The radar parameters are shown in Table 3.4.

Table 3.4: Satellite parameters of the two interferograms.

Orbit#	Date	Orbit#	Date	Elapsed time	Perp baseline (m)
20191	11/05/95	24020	02/17/96	105 days	227

Figure 3.2 is a satellite intensity image of the Lost Hills field. A satellite intensity image is essentially a map of reflection intensity of different portions of ground. The bright regular regions in the middle are agricultural fields; the dark portion to the lower left is a hilly area. It is also easy to see three dark lines in the image. The one on the top is highway CA46, the one to the upper right is Interstate 5, and the curved line to the mid-right is the California Aqueduct.

A change interferogram obtained from the described procedure represents the phase change between two signals reflected from the same point on the surface but at different time. The more the subsidence the larger the phase change. The radar wavelength of ERS satellites is 56 mm and, therefore, one cycle of phase corresponds to 28 mm (half wavelength) of radar line-of-sight displacement. The look angle of the ERS satellites is 23°. As a result, the vertical ground displacement that corresponds to a cycle is 30.4 mm ($28 \text{ mm} / \cos 23^\circ$).

Because the phase is periodical (2π), the change interferogram requires unwrapping to obtain the absolute surface deformation occurring between the two points in time. In this study we used a new unwrapping algorithm [*Chen and Zebker, 2000*], which gave improved results as compared to previous studies of the same area [*Fielding et al., 1998; van der Kooij et al., 1997*].

The interferogram corresponding to the 105-day period under examination is shown in Figure 3.3. The fringes form bowl-shaped patterns over Lost Hills and Belridge fields. One bowl-shaped fringe in this figure corresponds to 2π of the phase and 30.4 mm

vertical surface displacement. The number of the fringes over the Lost Hills field is between 4 and 5 and the resulting maximum subsidence is between 122 and 152 *mm*.

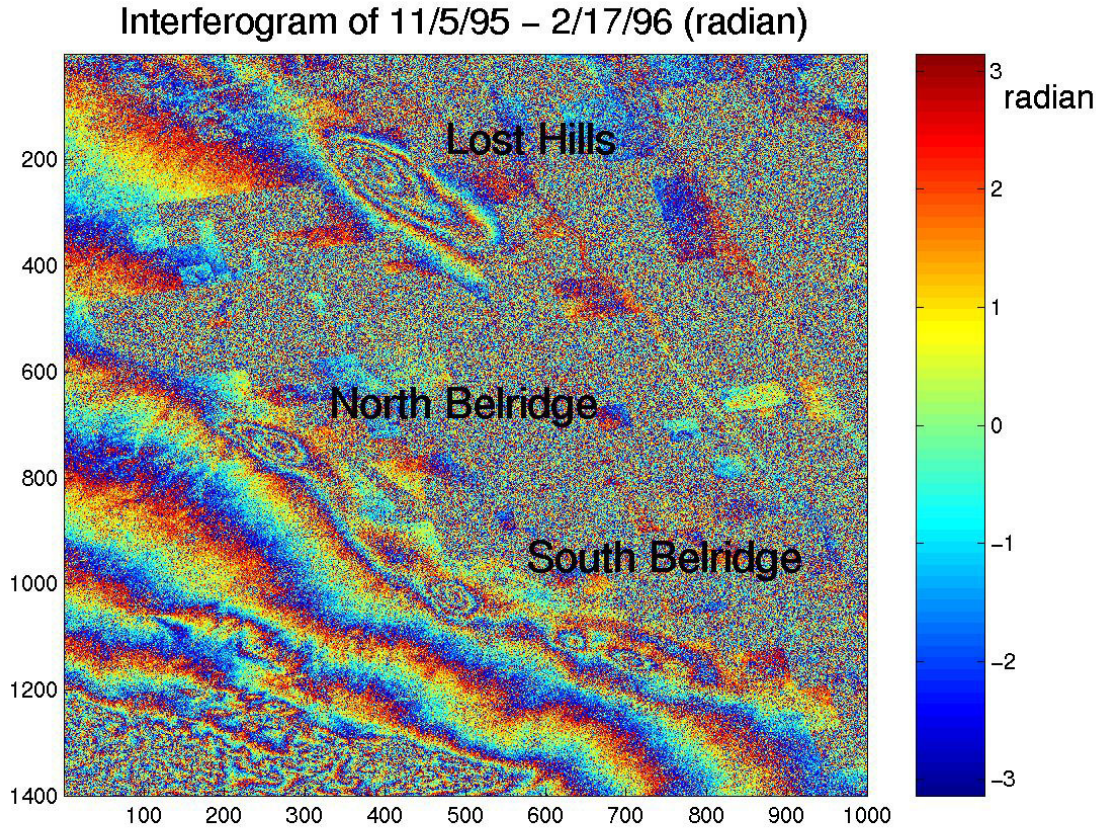


Figure 3.3: Interferograms of Belridge and Lost Hills oil field. The time lapse is 105 days (11/5/99 – 2/17/96). The perpendicular baseline is 227 meters, hence the image includes both deformation and topography information. Most noticeably, the large fringes to the bottom left are topography effects, while the “bowl” shaped fringes in the image are resulting from deformation.

The unwrapped interferogram is given in Figure 3.4 where the subsidence is color-coded. The first panel of Figure 3.5 zooms on the Lost Hills field. The maximum subsidence in the center of this field is about 15 *cm* – a dramatic value for the short period of 105 days.

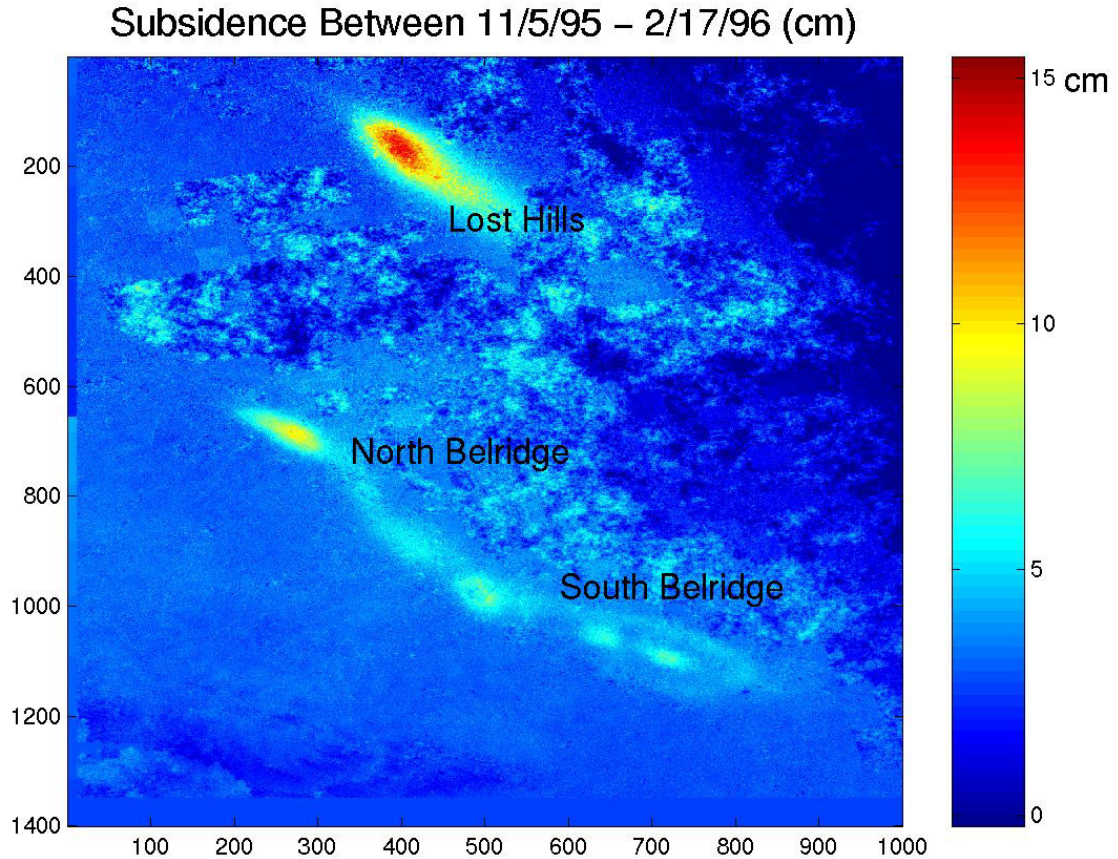


Figure 3.4: Unwrapped interferogram showing the subsidence in Belridge and Lost Hills oil fields occurred between 11/5/99 – 2/17/96 (105days). The scale is in centimeters. The maximum subsidence reached 15 cm at the center of Lost Hills field.

3.5 Subsidence from Oil Production

Reservoir deformation due to pore fluid withdrawal and pore pressure drop is a complicated poroelastic/plastic process that often involves faulting and micro-earthquakes [e.g., *Segall et. al*, 1994]. To model this deformation and the resulting surface subsidence, one needs detailed information about the poroelastic and plastic properties of the reservoir and overlaying rock. Also, implementing the full system of equations describing the process requires involved numerical simulation [e.g., *Settari and Mourits*, 1998; *Lewis and Shrefler*, 1998]. For more information, we refer the reader to Chapter 2.

In this study we use a simple model of surface deformation due to the shrinkage of a reservoir, which still allows us to highlight the principal features of the subsidence

process. The model [Geertsma, 1973] assumes that the reservoir is a circular disk of radius R and height h buried parallel to the flat earth surface at depth D . The elastic earth is treated as an elastic half-space with Poisson's ratio ν . Then the vertical component of the displacement of the surface u is

$$u(r) = (2\nu - 2)\Delta h R \int_0^{\infty} e^{-D\alpha} J_1(\alpha R) J_0(\alpha r) d\alpha \quad (1)$$

where r is the radial coordinate along the surface with the origin above the center of the reservoir; Δh is the reduction of the height of the reservoir due to its compaction; and α is the integration variable.

To determine the vertical deformation of the disk-shaped reservoir Δh , we assume that deformation is proportional to the change in the differential pressure acting on the reservoir, where the differential pressure is the difference between the overburden and pore pressure. The overburden pressure remains constant and, as a result, the reservoir's compaction is proportional to the pore pressure change ΔP .

The next assumption is that the reservoir's vertical deformation Δh is inversely proportional to the "static" Young's modulus E of the reservoir rock, which comes from laboratory high-strain deformation load-frame measurements. As a result,

$$\Delta h = h\Delta P / E. \quad (2)$$

de Rouffignac et al. [1995] present stress-strain curves for diatomite reservoir rock samples from South Belridge that are approximately linear in loading. The resulting average value of the static Young's modulus is about 0.046 *GPa*, which indicates that diatomite is extremely soft rock. We use the same E value for Lost Hills.

The same authors present production-data-based reservoir simulation results for South Belridge. From these results we estimate the approximate pore pressure drop over a 105-day period as 2.5 *psi* (160 *psi* of pore pressure drop for 20 years).

Next, we assume that the average reservoir thickness in Lost Hills is 300 *m*, according to *The California division of oil, gas and geothermal resources* [1984-1998]. Then the resulting Δh is 11 *cm*.

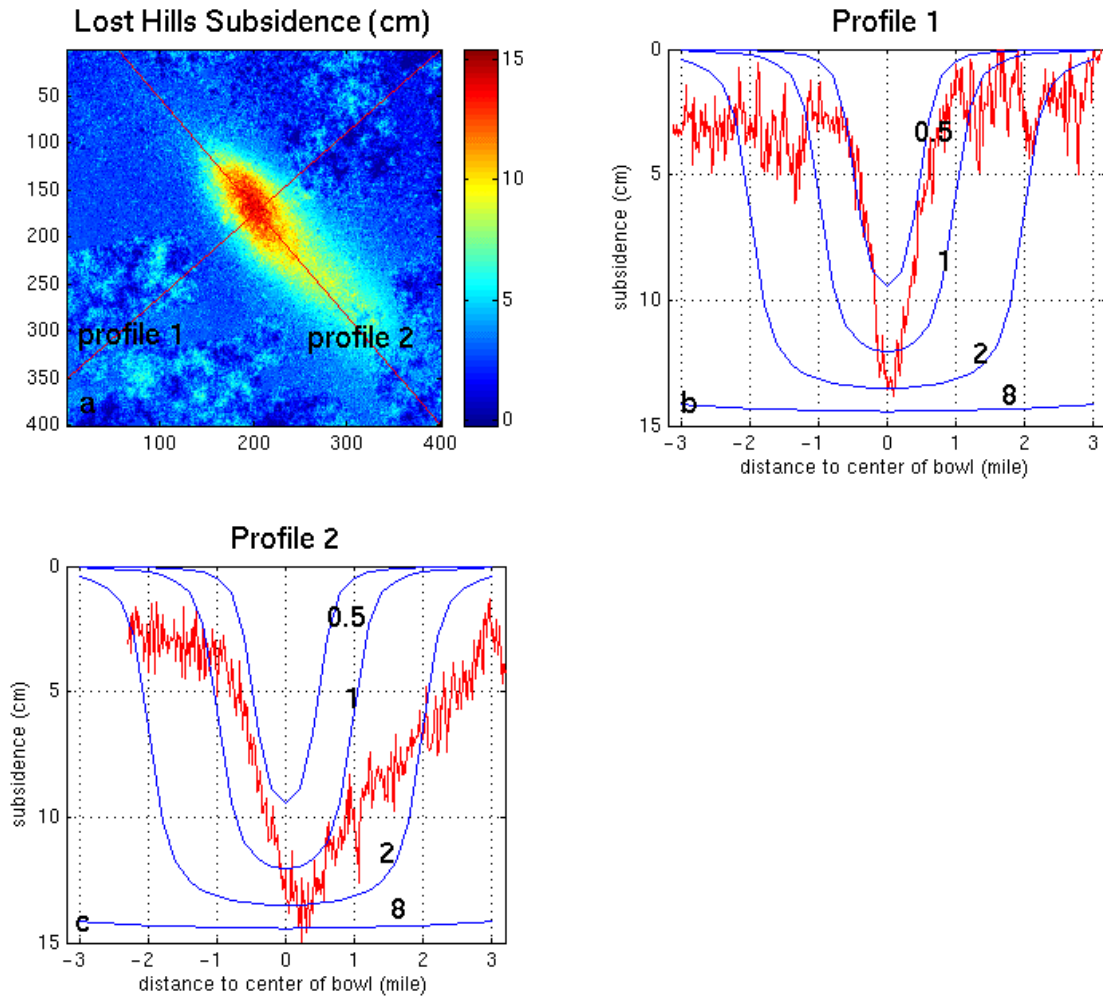


Figure 3.5: (a) InSAR observed subsidence in Lost Hills oil field occurred between 11/5/99 – 2/17/96 (105days). The dark lines show the locations of profile 1 and 2. The scale is in centimeters. (b). InSAR observed subsidence and theoretical subsidence along profile 1 for assumed reservoir radius of 0.5, 1, 2, and 8 miles, in Lost Hills field for the same period. (c) InSAR observed subsidence and theoretical subsidence along profile 2 for assumed reservoir radius of 0.5, 1, 2, and 8 miles, in Lost Hills field for the same period.

It is clear from Figure 3.1 that the Lost Hills reservoir is not circular but rather elliptical. Still, we will use the circular reservoir approximation and vary the reservoir radius to bound the estimate. Specifically, we use Equation (1) for $R = 0.5$; 1; 2; and 8

miles. We choose these values because the Lost Hills reservoir is 1 to 1.5 miles wide and about 16 miles long. Also, we use $D = 100$ m for the depth of burial of the Lost Hills reservoir [The California division of oil, gas and geothermal resources, 1984-1998]. We also choose $\nu = 0.3$ as an average Poisson's ratio in the shallow subsurface. The surface vertical displacement profiles for $R = 0.5$; 1; 2; and 8 miles are plotted versus the radial coordinate in Figure 3.5b and 3.5c. These displacement curves are superimposed on the subsidence profiles along the short (Figure 3.5b) and long (Figure 3.5c) axes of the elliptical subsidence bowl calculated from InSAR data.

The theoretical $R = 1$ and 2 mile profiles are close to the observed subsidence values. The $R = 8$ mile profile matches the peak of the observed subsidence. We conclude that, in general, the theoretical subsidence calculated from the production data is consistent with the InSAR data.

3.6 Discussion

3.6.1 Factors Affecting Surface Subsidence

The estimate given in the previous section shows that hydrocarbon production and surface subsidence can be quantitatively linked to each other. Therefore, it is possible, in principle, to monitor hydrocarbon production, and, in general, pore-fluid-related changes in the subsurface using InSAR data. Still, it is important to include additional and detailed production, and reservoir and rock property data into consideration.

Major factors that may affect surface subsidence include:

1. *Reservoir rock compressibility*
2. *Porosity, permeability, and fluid properties;*
3. *Reservoir size and thickness;*
4. *Reservoir depth;*
5. *Production volume.*

In the case of Belridge and Lost Hills fields, the large subsidence magnitude is mainly due to large reservoir rock compressibility, shallow reservoir depth, and large reservoir thickness.

Because of the shallow reservoir depth of Lost Hills field, heterogeneity in subsurface compaction is not blurred when transferred to the surface. It is seen in Figure 3.5 that subsidence is asymmetric along profile 2. This is possibly because production in Lost Hills takes place more in the Northwest portion than the Southeast portion of the field. Figure 3.6 is a well density map of the Lost Hills field. We see an apparent similarity in pattern between Figure 3.5a and Figure 3.6.

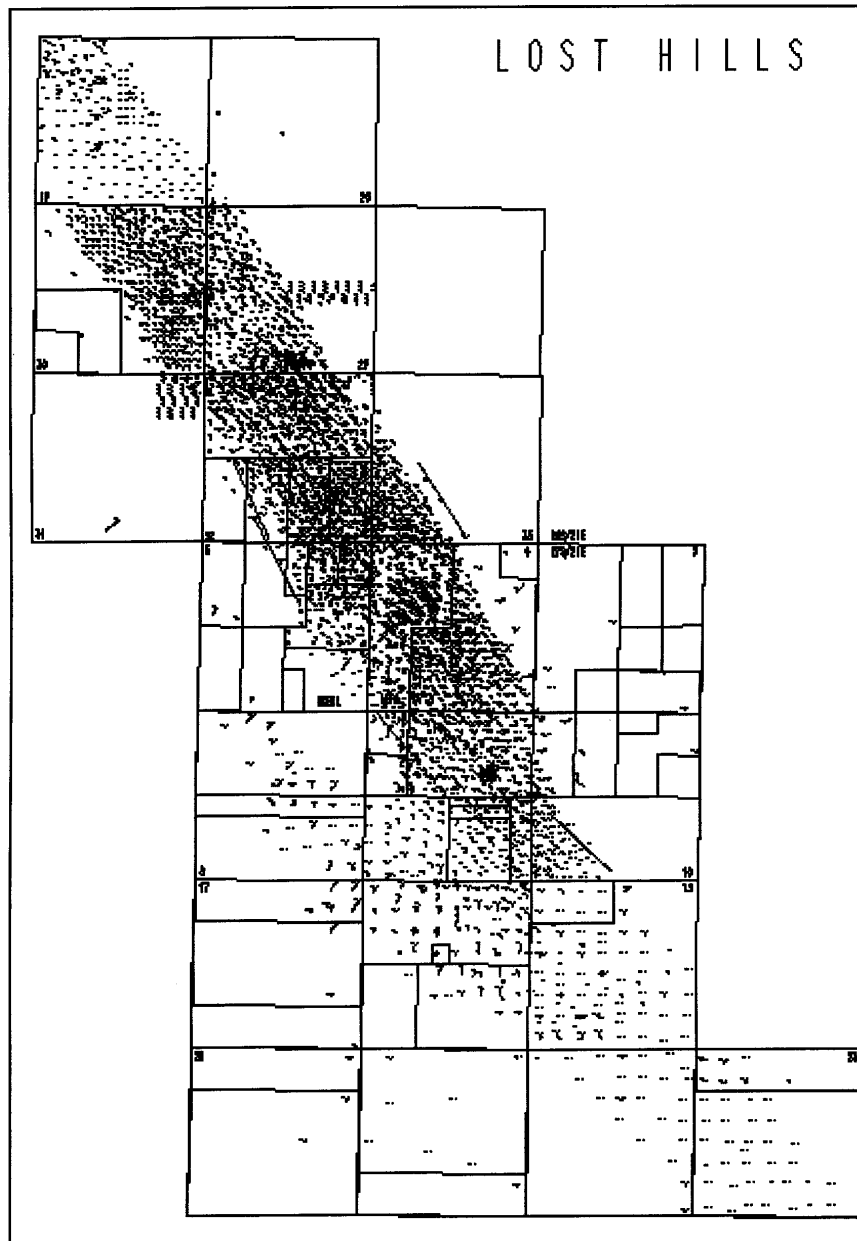


Figure 3.6: Well density map of Lost Hills oil field (courtesy of *Chevron USA*).

Reservoir rock compressibility, denoted C_m in *Geertsma's* model, plays an important role in affecting subsidence as well. Consider Figure 3.7 that shows the annual production in the Belridge (North and South) and Lost Hills oil fields compiled from various publications of *the California division of oil, gas and geothermal resources* [1984-1998]. It is apparent that Lost Hills field has produced oil at a much slower rate than South Belridge field. Logically, it would be reasonable that more subsidence should occur in Belridge than in Lost Hills. However, Figure 3.3 shows the opposite effect. This effect can be explained by the fact that Lost Hills has similar size as South Belridge, similar porosity, but is shallower, thicker, has higher permeability, and contains oil of lower viscosity. In addition, South Belridge produces only about 20% of its total production from soft diatomite [Bowersox, 1990], while most of the production in Lost Hills comes from diatomite. It is hence understandable why a significantly smaller production rate in Lost Hills caused subsidence comparable to or even larger than the subsidence in South Belridge.

Geertsma [1973] compiled the range of values for C_m in different rocks (Table 3.5), based on laboratory measurements. C_m depends on a number of factors, such as rock type, degree of cementation, porosity, and depth of burial. The lowest compressibility for sandstone formations is $0.16 \cdot 10^{-5} \text{ cm}^2/\text{kg}$, the compaction coefficient of pure quartz. The lower limit for limestones corresponds to the value for calcite, i.e., $0.08 \cdot 10^{-5} \text{ cm}^2/\text{kg}$. As a reference, the static Young's modulus of Belridge diatomite used in this study is 0.046 *GPa*, which corresponds to $C_m = 20 \cdot 10^{-5} \text{ cm}^2/\text{kg}$. This value falls into the same range as soft unconsolidated sandstones.

From the above discussion, we can see that reservoir properties such as rock compressibility, are essential factors in forming the final pattern of surface subsidence. Therefore, it may be possible to infer those important reservoir properties from high resolution InSAR data.

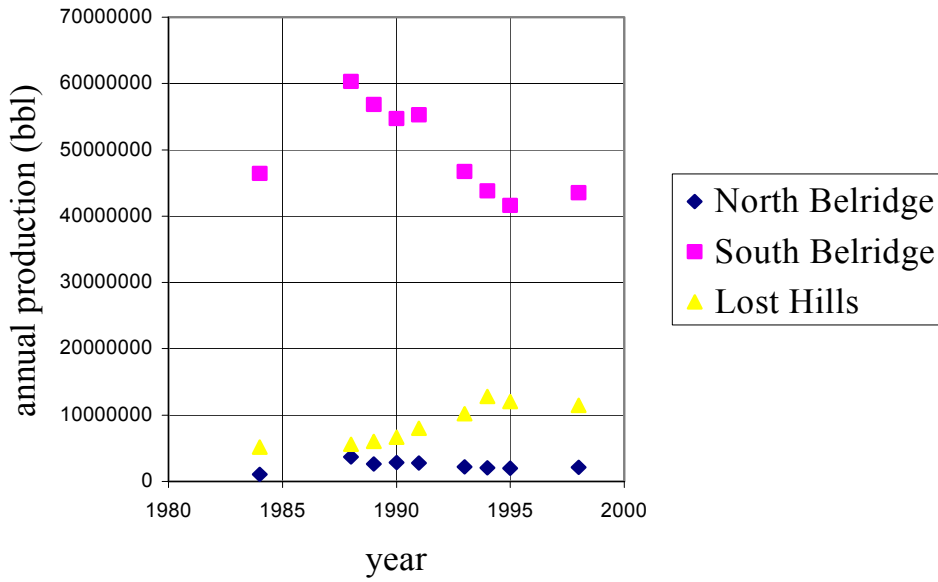


Figure 3.7: Annual production volume of the Belridge (North and South) and Lost Hills oil fields in barrels.

Table 3.5: C_m values (cm^2/kg) for sandstones and carbonates (compiled from Geertsma, 1973). Larger C_m values correspond to softer rocks.

Sandstone For effective vertical stress range: 100 ~ 200 kg/cm ³ (corresponds to depth of burial 1000 m)	well consolidated: $0.4 \sim 1.8 * 10^{-5}$
	semi-consolidated: $1.5 \sim 4 * 10^{-5}$
	unconsolidated: $3 \sim 45 * 10^{-5}$
Sandstone For effective vertical stress range: 300 ~ 600 kg/cm ³ (corresponds to depth of burial 3000 m)	well consolidated: $0.2 \sim 1.2 * 10^{-5}$
	semi-consolidated: $1 \sim 3.5 * 10^{-5}$
	unconsolidated: $5 \sim 20 * 10^{-5}$
Carbonate For effective vertical stress range: 100 ~ 200 kg/cm ³ (corresponds to depth of burial 1000 m)	well consolidated: $0.2 \sim 1.2 * 10^{-5}$
	vuggy carbonate, soft limestone: $1 \sim 5 * 10^{-5}$
Carbonate For effective vertical stress range: 300 ~ 600 kg/cm ³ (corresponds to depth of burial 3000 m)	well consolidated: $0.2 \sim 1 * 10^{-5}$
	vuggy carbonate, soft limestone: $1 \sim 4 * 10^{-5}$

3.6.2 Relationship Between Subsurface Compaction and Surface Subsidence

The magnitude and pattern of subsurface compaction and surface subsidence are often different. Compare Figures 3.1 and 3.4, we see that the size of subsidence bowl is much smaller than the size of reservoir. For example, in Lost Hills, the size of subsidence bowl is approximately 1 X 3 miles, while the size of the reservoir is 1 X 12 miles.

Reservoir depth is possibly the most important factor in determining the relationship between subsurface compaction and surface subsidence. For a shallow reservoir, the heterogeneity in subsurface compaction may be impressed in the heterogeneity of surface subsidence. However, for a deep reservoir, details in the subsurface may be averaged and blurred when transferred to the surface.

Traditionally, reservoirs are monitored using 4D seismic. In Chapter 5, we will discuss how 4D seismic data can be used together with geomechanical data to predict porosity loss in reservoirs. In the following, we will investigate the relationship between volume loss on the ground and in the reservoir. Since volume loss on the ground can be obtained by integrating surface subsidence (which is truly independent information besides seismic data), this relationship may be used as an integral constraint on porosity loss prediction from seismic data.

We first calculate the volume loss on the ground from SAR data and that in the subsurface from geomechanical data, for the Lost Hills field.

By integrating surface subsidence from SAR in Lost Hills, we obtain

$$\text{Volume Loss on ground} = 1.95 * 10^6 \text{ m}^3 \quad (3)$$

On the other hand, using values of reservoir compaction and size of Lost Hills field from the previous sections, we obtain

$$\begin{aligned} \text{Volume Loss in reservoir} &= \text{vertical compaction} * \text{reservoir size} \\ &= 3.54 * 10^6 \text{ m}^3 \end{aligned} \quad (4)$$

Therefore, the ratio of volume loss on ground over in the reservoir is

$$\text{Volume Loss Ratio} = 0.55 \quad (5)$$

Intuitively, volume loss on the ground should be smaller than that in the subsurface, because cap rocks above the reservoir “absorb” some of the volume loss.

We can also use *Geertsma’s* model [1973] to investigate the theoretical values of this volume loss ratio as a function of the ratio of reservoir depth over reservoir radius. The result is shown in Figure 3.8. Intuitively, the lower bound of the volume loss ratio should be 0, when the reservoir is infinitely deep (reservoir depth = infinity); the upper bound of the volume loss ratio should be 1, when the reservoir is infinitely shallow (reservoir depth = 0). Figure 3.8 describes this behavior.

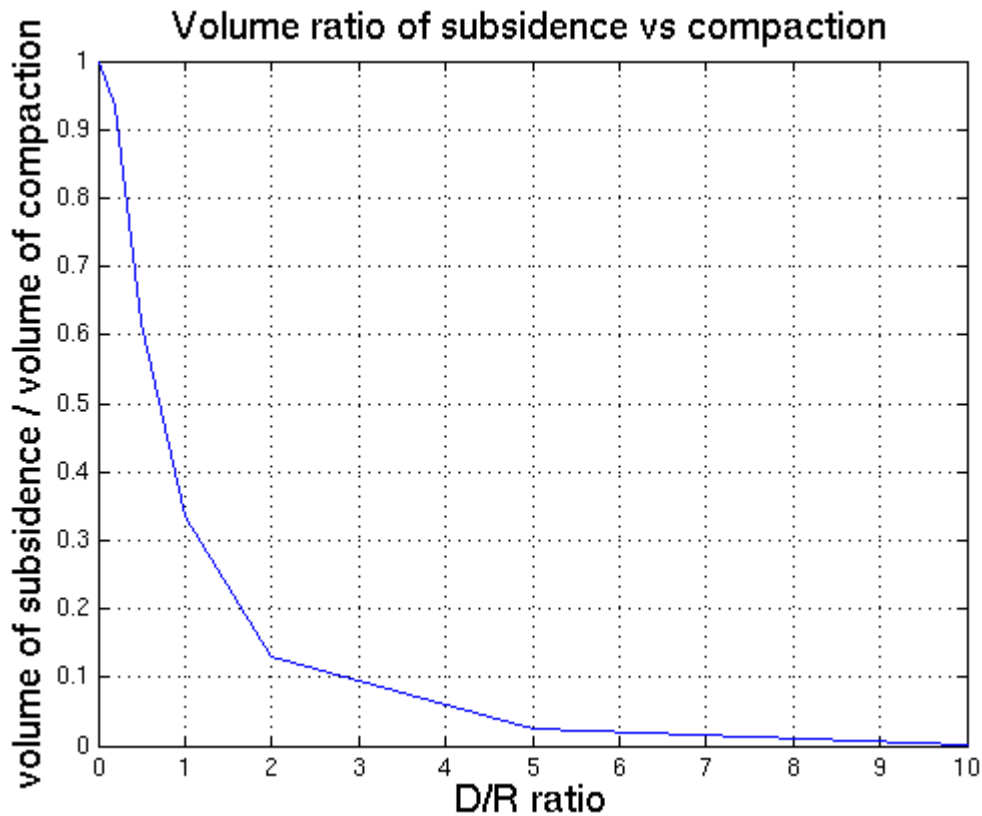


Figure 3.8: Theoretical values of volume loss ratio as a function of the ratio of reservoir depth over reservoir radius, calculated from *Geertsma’s* model [1973].

3.7 Conclusions

The case study in this chapter shows that applying physical modeling to the interpretation of InSAR data help determine important reservoir properties as well as fluid movement in the subsurface. Therefore, InSAR measurements can be an alternative or supplement to the expensive and time-consuming 4-D seismic reservoir monitoring technique.

3.8 Acknowledgments

Howard Zebker helped obtain SAR data and provided help for InSAR data processing; Curtis Chen provided software for phase unwrapping; Mamta Sinha helped with data processing. This work was supported by DOE grant DE-FG03-98ER14904.

3.9 Appendix : InSAR Basics

3.9.1 Where to Look

InSAR techniques for measuring small deformation by now have been well documented in the literature.

Theory of 2-pass interferometry can be found in the 1993 Nature paper of *Massonnet et al.*, “The displacement field of the Landers earthquake mapped by radar interferometry” [*Nature*, v. 364, p. 138-142, 1993].

Theory of 3-pass interferometry can be found in the 1994 JGR paper of *Zebker et al.*, “On the derivation of coseismic displacement fields using differential radar interferometry: The Landers earthquake” [*JGR*, v. 99, p 19617-19634, 1994].

A review paper by *Massonnet, D. and K.L. Feigl* titled “Radar interferometry and its application to changes in the earth's surface” [*Reviews of Geophysics*, v. 36, p. 441-500, 1998] is a fairly thorough discussion on the origin, theory, implementation and application of InSAR technique and contains over two hundred papers in its reference list.

3.9.2 Basic Concepts

Synthetic Aperture Radar is a microwave-coherent imaging system that has day, night and all-weather capabilities. In repeat-pass SAR interferometry, or InSAR, two SAR datasets of the same area acquired from almost identical perspective are co-registered and combined into a so-called interferogram. Using InSAR technique, a detailed and accurate 3-D relief map of the earth's surface can be produced [Zebker *et al.*, 1994].

An extension of the basic InSAR technique, denoted differential InSAR since the phase measurement of interest results from the difference of two interferograms, allows the detection of very small (cm, mm level) movement of land surface features. The power of the differential InSAR lies in its capability of providing the high-resolution and large area coverage with an almost unprecedented accuracy [Zebker *et al.*, 1994, van der Kooij, 1997].

3.9.3 Brief Theory

There are mainly two types of InSAR techniques: 2-pass interferometry and 3-pass interferometry. Of the two different approaches, each has its own advantages and disadvantages. One of the most favorable advantage 3-pass interferometry has over its 2-pass counterpart is that it does not require a digital elevation model (DEM). Here we follow Zebker *et al.* [1994] and discuss briefly the theory of 3-pass interferometry which is utilized in the preparation of this thesis. To make it more intuitive, we assigned time t , $t+2$ and $t+100$ to the three antenna locations A1, A2 and A2' (Figure 3.9), but in general they can be other time spans too.

Assume at time t a satellite flew through point A1 and “looked” at ground point P, which means a signal was sent from A1, arrived at P, and reflected back to A1, hence the round-trip distance is 2ρ . Then at a later time $t+2$, the same satellite flew through point A2 and “looked” at ground point P again, and the round trip distance is $2(\rho + \delta\rho)$.

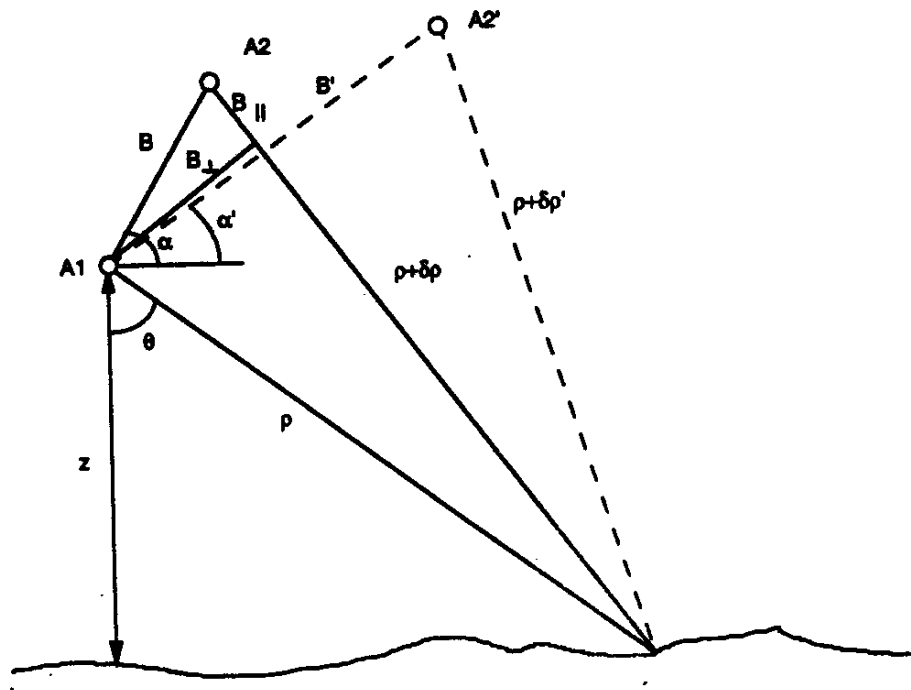


Figure 3.9: Radar imaging geometry. The solid lines show that radar signal paths for the first interferogram pair formed by antennas at A1 and A2. Dashed lines show signal path for second interferogram acquired over the same site but with antennas located at A1 and A2' (from Zebker, 1994).

For the two round-trip distances taken as 2ρ and $2(\rho + \delta\rho)$, the measured phase difference ϕ will be

$$\phi = \frac{4\pi}{\lambda} \delta\rho \tag{6}$$

when the assumption that each resolution element on the ground behaves the same for each observation is made (which is called “temporally correlated” --- more on this in Zebker *et al.*, 1994).

A few more steps will lead to $\delta\rho = B_{\parallel}$, and the key in the derivation is that z (for ERS-1/2, around 800 km) is much larger than B (usually less than 500 m to be useful) in reality. Therefore

$$\phi = \frac{4\pi}{\lambda} B_{//} \quad (7)$$

Let us next assume at time $t+100$, the same satellite flew through A2' and looked at ground point P again. If there were deformation during the time between t and t and $t+100$, then the phase difference between A1-P and A2'-P would be

$$\phi' = \frac{4\pi}{\lambda} (\delta d + B'_{//}) \quad (8)$$

in which δd denotes deformation. Comparing (2) and (3), it is easy to see that deformation δd is

$$\delta d = \frac{\lambda}{2} \frac{\phi' - \frac{B'_{//}}{B_{//}} \phi}{2\pi} \quad (9)$$

For ERS-1 and ERS-2 satellites, $\frac{\lambda}{2} = 28 \text{ mm}$, hence a fringe (2π of phase difference) corresponds to 28 mm of deformation.

3.9.4 Quick Facts

Standard applications of InSAR are measuring topography and deformation. Here we list some facts about InSAR in measuring deformation.

1. *Horizontal resolution*: several tens of meters
2. *Vertical accuracy*: cm / mm level
3. *Coverage*: large area of coverage (hundreds of square kilometers)
4. *Observation cadence*: ~ 1 pass / month for ERS satellites
5. *Data availability*: available from several space agencies in the US, Europe, Canada, and Japan (e.g., European space agency launched ERS-1 in 1991,

ERS -2 in 1995 and is planning to launch ENVISAT in 2000, all of which provides high-quality SAR data).

6. *Software availability*: there are many InSAR software packages available, a large portion of them are public domain packages (e.g., the Stanford InSAR package is a full-capability InSAR package available in public domain).

In comparison, traditional (detailed surveying and tide gauges, GPS) geodetic measurements:

1. Measure changes in the locations of a limited set of benchmarks
2. Require a large number of individual observations to map the subsidence distribution
3. Require ground access
4. Generally costly to acquire

3.9.5 Previous Applications

InSAR techniques have been successfully applied to measuring small deformations in many different areas such as earthquakes, glaciers, landslides, and volcanoes.

3.10 References

- Amelung, F., D.L.Galoway, J.W.Bell, H.A.Zebker, and R.J.Laczniak, 1999, Sensing the ups and downs of Las Vegas: InSAR reveals structural control of land subsidence and aquifer-system deformation, *Geology*, v. 27, pp. 483-486.
- Barends, F.B.J., F.J.J Brouwer, and F.H. Schroder, 1995, *Land subsidence*, A.A.Balkema, Rotterdam.
- Bowersox, J.R., and R.A. Shore, 1990, Reservoir compaction of the Belridge diatomite and surface subsidence, South Belridge field, Kern County, California, in *Structure, Stratigraphy and hydrocarbon occurrence of the San Joaquin Basin, California, Pacific Sections of the S.E.P.M and A.A.P.G., Bakersfield, CA*, edited by J.G.Knespert, and S.A.Reid, pp. 225-230.
- Bowersox, J., 1990, Geology of the Belridge diatomite, Northern South Belridge field, Kern County, California, in *Structure, Stratigraphy and hydrocarbon occurrence of the San Joaquin Basin, California, Pacific Sections of the S.E.P.M and A.A.P.G., Bakersfield, CA*, edited by J.G.Knespert, and S.A.Reid, pp. 215-223.

- Bruno, M.S., and C.A. Bovberg, 1992, Reservoir compaction and surface subsidence above the Lost Hills field, California, in *Rock Mechanics: proceedings of the 33rd U.S. symposium*, edited by Tillerson, and Wawersik, pp. 263-272, Balkema, Rotterdam.
- California Division of oil, gas and Geothermal resources, 1984-1998, *preliminary report of California oil and gas production statistics*.
- Chen, C. and H. Zebker, 2000, Network approaches to two dimensional phase unwrapping: intractability and two new algorithms, *Journal of the Optical Society of America*, volume 17, pp. 401-414.
- Dale, B.A., G.M.Narahara, and R.M. Stevens, 1996, A case history of reservoir subsidence and wellbore damage management in the South Belridge diatomite field, *SPE 35658*, pp. 101-113.
- De Rouffignac, E.P., P.L.Bondor, J.M.Karanikas, and S.K.Hara, 1995, Subsidence and well failure in the South Belridge diatomite field, *SPE 29626*, pp.153-167.
- Fast, R.E., A.S.Murer, and L.G. Zambrano, 1993, Lost Hills diatomite simulation study: predicting waterflood performance in a low-permeability compacting reservoir, *SPE 26627*, pp. 193-204.
- Fielding, E.J., R.G. Blom, and R.M. Goldstein, 1998, Rapid subsidence over oil fields measured by SAR interferometry, *Geophysical Research Letters*, vol. 25, no 17, pp. 3215-3218.
- Gabriel, A.G., R.M. Goldstein, and H.A. Zebker, 1989, Mapping small elevation changes over large areas: differential radar interferometry, *J. Geophy R.*, 94, pp. 9183-9191.
- Geertsma, J., 1973, Land subsidence above compacting oil and gas reservoirs, *Journal of Pet. Tech.*, pp. 734-744.
- Lewis, R.W., and B.A.Shrefler, 1998, *The finite element method in the static and dynamic deformation and consolidation of porous media*, John Wiley & Sons.
- Massonet, D., M.Rossi, C.Carmona, F.Adragna, G.Peltzer, K.Feigl, and T.Rabaute, 1993, The displacement field of the Landers earthquake mapped by Radar interferometry, *Nature* 364, pp. 138-142.
- Massonet, D. and K. Feigl, 1998, Radar interferometry and its application to changes in the earth's surface, *Review of Geophysics*, volume 36, number 4, pp. 441-500.
- Segall, P., J.Grasso, and A. Mossop, 1994, Poroelastic stressing and induced seismicity near the Lacq gas field, Southwestern France, *J. Geophy R.*, 99, pp. 15,423-15,438.
- Settari, A., and F.M. Mourits, 1998, A coupled reservoir and geomechanical simulation system, *SPE 50939*, pp. 219-226.

- Van der Kooij, M., 1997, Land subsidence measurements at the Belridge oil fields from ERS InSAR data, in the third ESA ERS symposium, Florence, Italy, at <http://earth1.esrin.esa.it/florence/papers/data/vanderkooij1/index.html>.
- Wallace, N.J., and E.D.Pugh, 1993, An improved recovery and subsidence mitigation plan for the Lost Hills field, California, *SPE* 26626, pp. 183-192.
- Zebker, H. A., P.A. Rosen, R.M.Goldstein, A.Gabriel, and C.L.Werner, 1994, On the derivation of coseismic displacement fields using differential radar interferometry: the Landers earthquake, *J. Geophys. R.*, (99) B10, pp. 19,617-19,634.

Chapter 4

Static Monitoring: Compaction/Subsidence as a Stand- Alone Monitoring Tool

4.1 Abstract

In this chapter, we study the “ear-shape” puzzle: the effect of permeability anisotropy and boundary conditions on the pattern of production-induced pressure depletion and surface subsidence. Using this example, we demonstrate that, in principle, InSAR can be used as a stand-alone tool for reservoir monitoring.

We study the effects by performing numerical simulations on an imaginary reservoir that is homogeneous and isotropic except that the permeability is anisotropic. The numerical simulations are performed for different combinations of permeability anisotropy and boundary conditions. We find that the subsidence pattern is affected by both factors. Since we often have fairly good ideas about the tectonic settings and boundaries of a reservoir from geology, using subsidence from InSAR, we may be able to infer information about permeability anisotropy, which is otherwise very difficult to obtain.

4.2 Introduction

InSAR can be used as a stand-alone tool for reservoir characterization and monitoring. A quick observation is that the magnitude and patterns of subsidence are often good indications of reservoir shape, size and depth. They are also affected by reservoir rock properties and production history. In Chapter 3, we have shown that the large subsidence in Lost Hills, as compared to Belridge, is due to its shallow reservoir depth, large reservoir thickness, and large reservoir rock compressibility, although Lost

Hills has a much more modest production volume than Belridge. We have also shown that the asymmetry of subsidence in the Lost Hills field is most likely caused by the asymmetric distribution of production volume inside the field.

In addition to the above factors, subsidence pattern may also be an indication of permeability anisotropy. Permeability anisotropy is often recognized in producing reservoirs and is known to have significant effects on production. Surface subsidence, which is the surface imprint of reservoir pressure depletion and compaction, may be used to detect permeability anisotropy in the reservoir. In this chapter, we will show how the combined effect of permeability anisotropy and boundary conditions form the pressure depletion pattern in producing reservoirs.

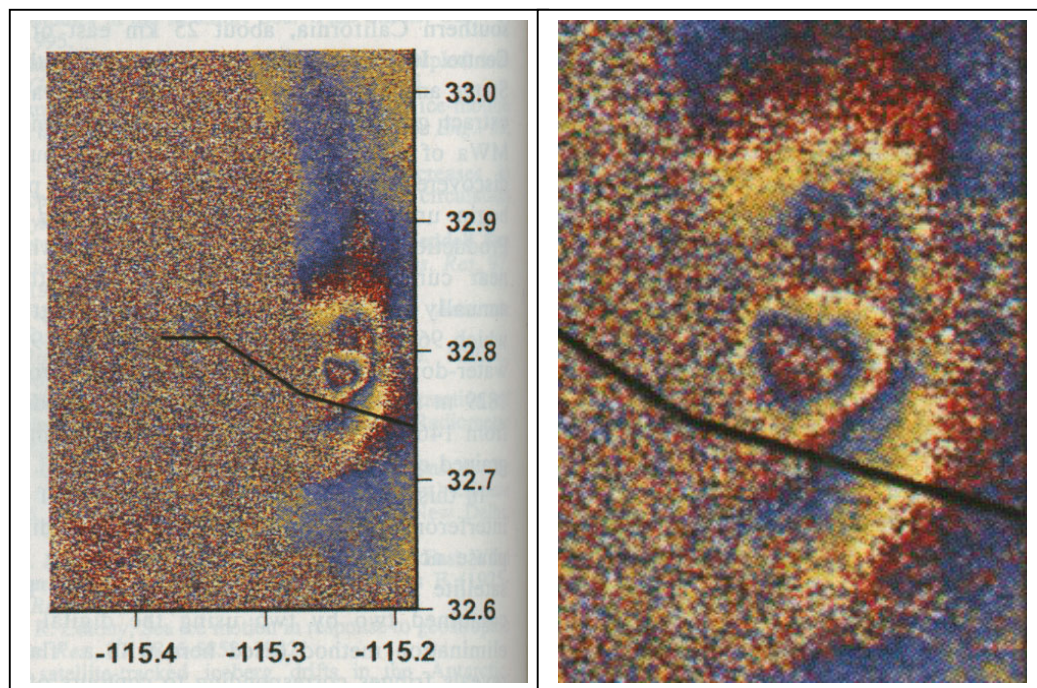


Figure 4.1: (left) Surface subsidence over a two-year period between 1992 and 1994 at East Mesa field caused by the activity of a geothermal plant (from *Massonnet et al.*, 1997). (right) Zoom in of the subsidence area.

Figure 4.1 is a 2D map showing the surface subsidence occurred at East Mesa geothermal field in California over a period of two years between 1992 and 1994 [*Massonnet et al.*, 1997]. The image is acquired using Satellite Radar Interferometry (InSAR), which is a technique for detecting surface deformation at very high resolution (100 m) and precision (cm level) [*Zebker et al.*, 1994]. The elliptical shape of subsidence

in East Mesa may be due to different reasons, one of them being permeability anisotropy in the reservoir. The question is, if the assumption is made that all reservoir properties are homogeneous and isotropic except permeability, then which diagonal of the ellipse has larger permeability?

When Nur challenged his audience with this question during the Stanford Rock Physics (SRB) annual meeting in 1999, there were two different guesses: (1). The N-S direction has larger permeability so that fluid is easier to flow along that direction to cause more pressure drop (2). The E-W direction has larger permeability so that fluid is easier to flow along that direction, and fluid in the near-well region can be easily replaced by fluid from far-well region, hence causing less pressure drop and surface subsidence.

The question has since been known within SRB as the “ear-shape (the subsidence pattern at East Mesa) puzzle”. The practical significance of the proposed question lies in the fact that permeability has long been one of the most difficult-to-obtain reservoir properties. If the above question can be correctly answered, then we may be able to get at least some qualitative or semi-quantitative information about permeability, under the situation when we do not have much knowledge about permeability, but do have some reasonable knowledge about other reservoir properties, with a little inexpensive help from subsidence obtained from SAR.

In this chapter we will show, by numerical analysis, that a complete answer will depend both on permeability anisotropy and on boundary conditions.

4.3 Numerical Simulation

If we assume that in a reservoir, production causes pore pressure drop, which again causes reservoir compaction and surface subsidence, then the key to answering the above puzzle will be to simulate the fluid flow behavior in reservoirs.

Over the years reservoir engineers have established a full suite of methods and tools for fluid flow simulation [e.g., *Aziz and Settari, 1979*]. In this chapter, we will solve the standard reservoir simulation equation in 2D for different combinations of permeability anisotropy and boundary conditions.

4.3.1 Setup

In petroleum engineering, the process of pore pressure depletion induced by oil production is often characterized by the following pore pressure diffusion equation [Aziz & Settari, 1979]:

$$\frac{\partial p}{\partial t} = c \nabla^2 p + Q \quad (1)$$

In this chapter, we solve the above equation in 2D for different combinations of permeability anisotropy and boundary conditions. In brief, the reservoir under study is square-shaped which contains single-phase fluid (oil), and the production well is placed at the center of the reservoir with fixed production rate. The parameters we used are shown in Table 4.1.

Table 4.1: Simulation setup for solving equation (1). The meanings of most of the parameters are straightforward; the meaning of “ γ ” will be explained in the next section.

1. reservoir geometry	
$L_x = L_y = 2100$ ft, $L_z = 500$ ft	(reservoir size)
$D_{top} = 8000$ ft	(top of reservoir)
2. reservoir properties	
$\phi = 0.2$	(porosity)
$C_f = 5.5 * 10^{-6}$ psi ⁻¹	(oil compressibility)
$\rho_o = 49.1$ lbm/ft ³	(oil density at SDT)
$\mu = 1$ cp	(oil viscosity)
3. simulation parameters	
$Q_{center} = 20000$ STB/day	(production rate)
$P_{init} = 3686.889$ psi	(initial pressure)
$P_{ref} = 14.7$ psi	(reference pressure)
$T = 50$ day	(total run time)
$D_t = 1$ day	(time step)
4. boundary condition	
$\gamma_1 = \gamma_2 = c1$	(see text)
$\gamma_3 = \gamma_4 = c2$	(see text)

4.3.2 Handling of Boundary Conditions

Typically there are three types of boundary conditions for pressure diffusion equations in petroleum applications: (1) prescribed zero flux condition for closed boundary; (2) prescribed finite flux condition or (3) prescribed constant pressure condition for open boundary. Both (1) and (2) are the Neuman boundary conditions; (3) is the Dirichlet boundary condition.

In this chapter, we select the two Neuman boundary conditions (1) and (2) for closed and open boundaries, respectively. The value of γ in table 4.1 is defined as the ratio of flux through the boundary to the flux through the grid line immediately next to the boundary. Therefore $\gamma = 0$ means closed boundary; $\gamma > 0$ means open boundary. γ_1 and γ_2 are for the two ends of x direction, γ_3 and γ_4 are for the two ends of y direction. In this chapter, we use $\gamma = 1$ to represent an open boundary.

4.4 Simulation Results

Figure 4.2 shows the simulation results, which are the pore pressure distribution after 50 days of production for our specific setup. In the following discussion, we will use “plate (1,1)”, “plate (1,2)”, ... , through “plate (3,4)” to denote the images contained in Figure 4.2, where the numbers inside the parentheses corresponds to the row and column numbers, respectively.

To study the first order effect, we assumed earlier that surface deformation is related to pore pressure drop. Therefore, the pore pressure images in Figure 4.2 can be qualitatively thought of as estimates of surface subsidence. One obvious observation is that, for that square-shaped reservoir, an anisotropic subsidence can be caused by either anisotropic permeability or anisotropic boundary condition. Since geology can often give us a fairly good idea about reservoir dimension and boundaries, the extra information of subsidence may help us gain a better understanding towards permeability, which is otherwise difficult to obtain.

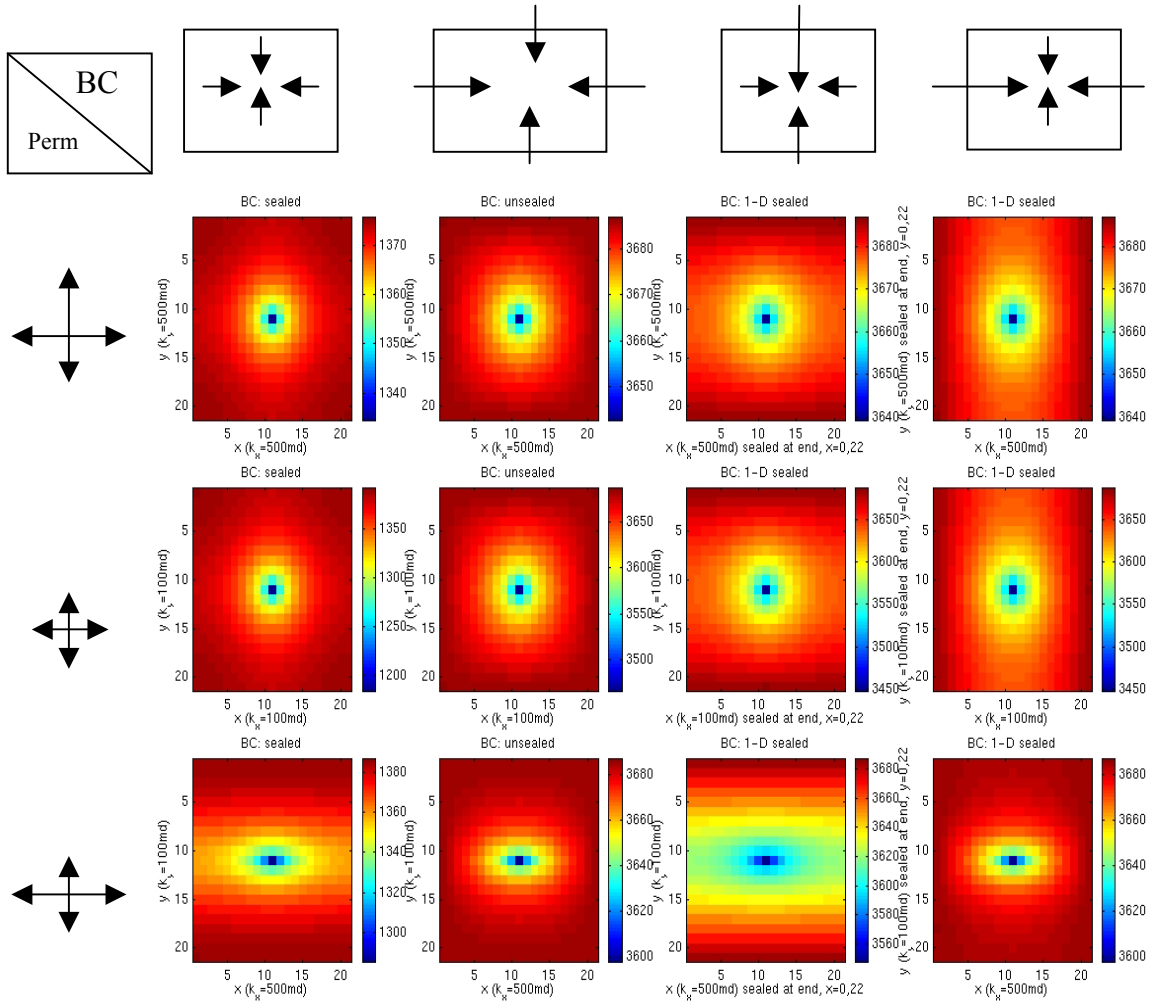


Figure 4.2: Pressure distribution after 50 days of production. The diagrams on top show boundary conditions --- an arrow that is completely inside the box represents closed boundary, and an arrow that crosses the box represents open boundary. The diagrams to the leftmost show permeability – a short arrow represents $k=100$ mD, and a long arrow represents $k=500$ mD. Therefore, for example, the image on the bottom right has the following setup: $k_x = 500$ mD, $k_y = 100$ mD, open boundary along x direction (here we use $\gamma_1 = \gamma_2 = 1$), close boundary along y direction (here we use $\gamma_3 = \gamma_4 = 0$).

4.4.1 Closed Boundary and Isotropic Permeability --- Plates (1,1) & (2,1) of Figure 4.2

Plates (1,1) and (2,1) both have isotropic permeability and closed boundaries in both x and y directions. It appears to be counter-intuitive that pressure drops more in plate (2,1) where $k_x = k_y = 100$ mD are smaller than in plate (1,1), because smaller

permeability means fluid is harder to flow. However, the reason for this counter-intuitive result is that the same constant production rate constraints are specified in both cases.

4.4.2 Open Boundary and Isotropic Permeability --- Plates (1,2) & (2,2) of Figure 4.2

Plates (1,2) and (2,2) both have isotropic permeability and open boundaries in both x and y directions. We observe that pressure drops more in plate (2,2) where permeabilities are smaller than those in plate (1,2).

In practice, an open boundary is often modeled as aquifer support or injection wells (sometimes production wells). Therefore, when injection rates at the boundary are carefully arranged, an open boundary reservoir may be equivalent to a closed boundary reservoir with injection wells sitting on the boundary.

If we think of plates (1,2) and (2,2) as closed reservoirs with injections wells located at the boundaries, then the above observation explains the phenomenon that, when permeability is low, it is more difficult to mitigate local compaction at production wells by fluid injection into adjacent wells. The same rule applies to high-viscosity fluid: if the fluid viscosity is very high, local compaction at production wells cannot be mitigated by fluid injection into adjacent wells [Donaldson, 1995].

4.4.3 Open Boundary and Anisotropic Permeability, Plate (3,2) of Figure 4.2

In plate (3,2), pressure drop is more significant along the x direction (the horizontal direction in the image), along which the permeability is larger.

As we mentioned in the introduction section, one argument is that pressure should drop less along the x direction, because the large permeability along the x direction will make it easier for the fluid at the near-well region to be replaced, hence maintain pore pressure. However, if we think of the open boundary reservoir as an infinite homogeneous reservoir, then (1) the pressures at the center are the same for both x and y direction; (2) the pressures at infinity are also the same (probably zero) for both x and y direction; (3) the overall fluid flow to the production well is larger along the x direction

since k_x is larger. Therefore, it is apparent that pressure drop will be more significant along the x direction, as seen in Figure 4.3.

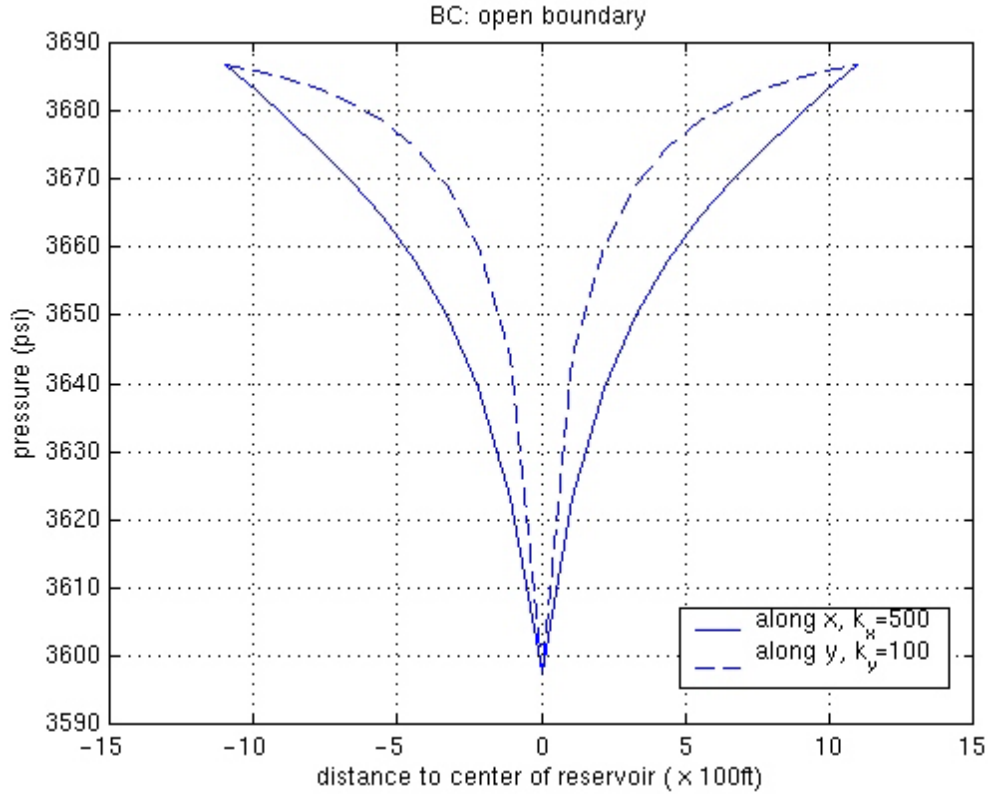


Figure 4.3: Pressure profiles for open boundary and anisotropic permeability.

4.4.4 Closed Boundary and Anisotropic Permeability, Plate (3,1) of Figure 4.2, and Explanation From the Analytical Solution

In plate (3,1), the pressure drop is more significant along the x direction (the horizontal direction), along which the permeability is larger.

This observation is easily explained by considering the partial differential equation [Carslaw & Jaeger, 1986; Gringarten & Ramey, 1973]. In 2D, equation (1) is often written as:

$$\frac{\partial p}{\partial t} = \frac{k_x}{\phi \mu c} \frac{\partial^2 p}{\partial x^2} + \frac{k_y}{\phi \mu c} \frac{\partial^2 p}{\partial y^2} + q \quad (2)$$

When $k_x = k_y$ (isotropic), the pressure distribution will be axisymmetric. When permeability is anisotropic, a simple variable substitution of

$$x' = x / \sqrt{k_x}, \quad y' = y / \sqrt{k_y} \quad (3)$$

explains the result shown in plate (3,1). Although different methods (mainly Fourier Transform, Laplace Transform and Green's Functions methods) can be applied to solve Equation (2) analytically, the fact that permeability appears in the numerator rather than in the denominator is itself sufficient to determine the pressure drop pattern in anisotropic reservoirs.

4.4.5 Closed Boundary Along One Direction, the Last Two Columns in Figure 4.2

The combined effects of permeability anisotropy and boundary conditions show more dramatic results when the boundary is open along one direction and closed along the other direction. The two basic observations are, first, pressure drop is more significant along the direction which has a closed boundary; second, there is competition in the effect of permeability and boundary condition in determining the pressure drop pattern.

4.5 Rectangular Reservoir

A seemingly simple and straightforward explanation for the elliptical shape of subsidence in Figure 4.1 is that the shape of the reservoir itself is elliptical. In the following, we will discuss what happens in a rectangular reservoir (instead of a elliptical reservoir, for mathematical convenience) to answer the question.

Figure 4.4 shows pressure distribution after 50 days of production in a rectangular reservoir for our specific setup. It mimics the situation of an infinite slab reservoir bounded by two impermeable faults at the top and bottom. It is interesting that although the reservoir extends along the x direction, the pressure contour actually extends along the y direction.

Figure 4.5 gives the explanation, in which the two situations in (a) and (b) are thought to be equivalent. Situation (a) is the same as Figure 4.4. Situation (b) describes a fully closed reservoir, with injection wells sitting on the boundary of the x direction --- it is apparent that pressure drop will be smaller along the x direction because of the supply by the injection wells.

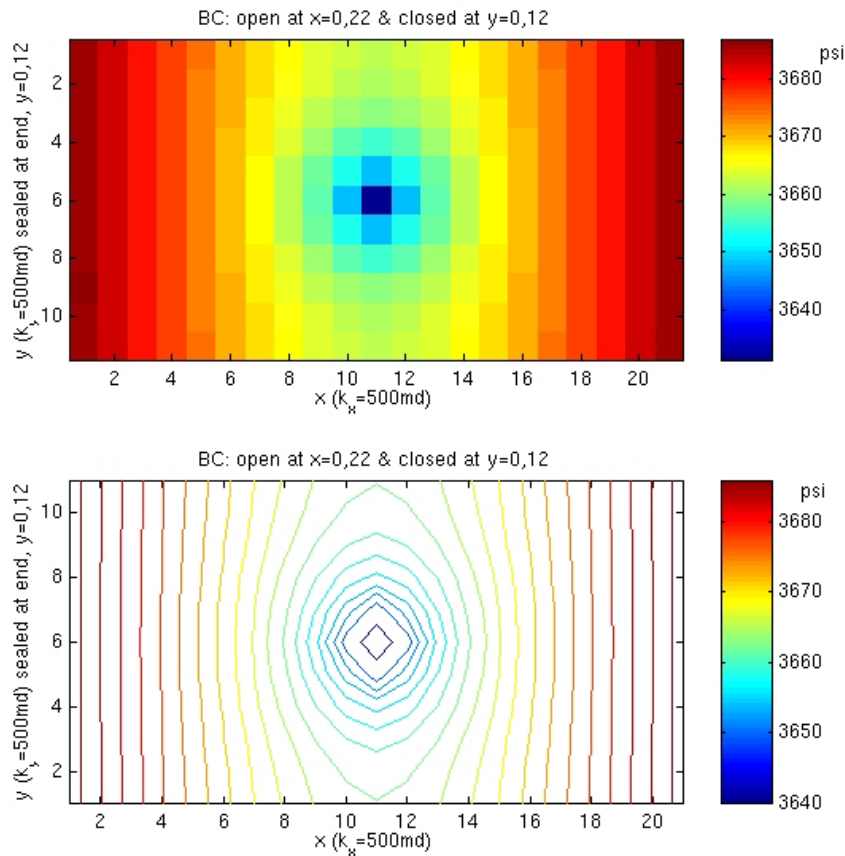


Figure 4.4: Pressure distribution after 50 days of production in a rectangular reservoir, whose length is twice its width. The single producing well is at the center of reservoir. Permeability is isotropic. The boundary is open to the left and right, while closed at the top and bottom.

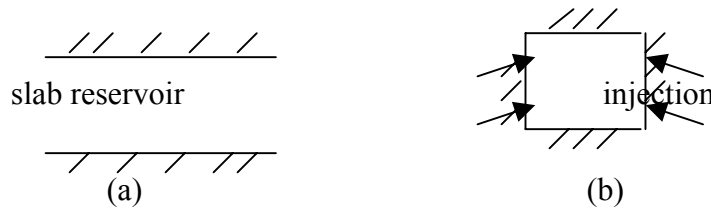


Figure 4.5: Explanation for the observation in Figure 4.4 that pressure drop is more significant along the direction where the boundaries are closed.

The result shows that, if we obtain a subsidence map similar to one shown in Figure 4.1, it is not always correct to conclude that the reservoir extends along N-S direction. If boundary condition happens to be similar to the one we show in Figure 4.4, then the result may be just the reverse.

4.6 Discussion

In this chapter, we have shown how reservoir simulation can be integrated with satellite remote sensing for better reservoir description and monitoring. The idea is simple: if subsidence occurs over an oil field, satellite remote sensing can be used to detect the subsidence, and reservoir simulation can be used to model the subsidence. By integrating reservoir simulation and satellite remote sensing, we can continuously monitor the hydrocarbon production in the reservoir.

Comparing to ten years ago, there is much less doubt about the importance of reservoir monitoring [Nur, 1989]. 4D seismic, for example, has shown remarkable success in the industry. Nevertheless, it is not the only possible approach. Ushijima *et al.* [1999], for example, explored a 4D electrical technique for monitoring fluid flow behaviors during massive water/steam injection operations through a borehole. In fact, if we really think about reservoir monitoring, its ultimate goal is no more than mapping the changes in producing reservoirs. The major changes during production/injection are typically fluid saturation and pore pressure changes (sometimes temperature changes as well), which have profound effects on a full range of physical quantities: velocity, electromagnetic properties, reservoir compaction, and so on. From this perspective, 4D seismic merely uses one of the above listed quantities – velocity – for its monitoring operations. The question to ask then is “can we use other quantities for monitoring as well?”

In this chapter, we have shown an initial step in such an attempt: using production-induced surface subsidence for reservoir monitoring. The basis for such monitoring will be the integration of reservoir simulation and InSAR, with one providing a technique for field measurement and the other for numerical simulation. From the example we presented above, the method seems to be feasible. Comparing to 4D seismic, it has two

significant advantages: (1) low cost (SAR data can typically be ordered with a modest fee); (2) continuous monitoring ability (SAR data are available for a specific point every one month or so). The second point is especially interesting because, unlike 4D seismic, which typically samples only a few points on the time axis, the method we proposed can have a much higher sampling rate (one sample per month) on the time axis, and hence closely monitor changes in the reservoir.

SAR does have limitations. The most significant is that SAR cannot be used to measure subsidence in offshore fields as well as in areas with heavy vegetation.

4.7 Conclusions

In this chapter, we analyzed the combined effect of permeability anisotropy and boundary condition on forming the pattern of reservoir pressure depletion. We found that in a producing reservoir, pressure tends to drop more along the large permeability direction, and along the direction at whose ends the boundary are closed to fluid flux.

Since subsidence is merely a surface imprint of reservoir pressure depletion, the result presented here can be used as a basis for detecting permeability anisotropy from surface subsidence.

Traditionally, permeability anisotropy is detected through well testing [*Zhang et al.*, 1996] or analyzing production data [*Arnold et al.*, 1962]. However, as high precision, high resolution InSAR data become available, the implication of detecting permeability anisotropy using InSAR data is promising and it can serve as a supplement or alternative to the traditional detection and monitoring tools.

4.8 Acknowledgments

This work was supported by the Stanford Rock Physics & Borehole Geophysics Project (SRB) and DOE.

4.9 References

- Arnold, M. D., Gonzalez, H.J., and Crawford, P.B., 1962, Estimation of Reservoir Anisotropy From Production Data, *Journal of Petroleum Technology*, August, 1962, pp. 909-912.
- Aziz, K., and Settari, A., 1979, *Petroleum Reservoir Simulation*, Applied Science Publishers.
- Carslaw, H.S., and Jaeger, J.C., 1986, Conduction of Heat in Solids, *Oxford University Press*.
- Donaldson, E.C., 1995, Simulation of Compaction due to Fluid Withdrawal, in *Subsidence due to Fluid Withdrawal*, edited by G.V. Chilingarian and E.C. Donaldson, Elsevier Science, pp. 425-438.
- Gringarten, A., and Ramey, H.J., 1973, The Use of Source and Green's Functions in Solving Unsteady-Flow Problems in Reservoirs, *SPE Journal*, October, 1973, pp. 285-296
- Massonnet, D., Holzer, T., and Vadon, H., 1997, Land Subsidence caused by the East Mesa Geothermal Field, California, Observed Using SAR Interferometry, *Geophysical Research Letters*, vol.24, no.8, pp. 901-904.
- Nur, A., 1989, Four-dimensional seismology and (true) direct detection of hydrocarbons: The petrophysical basis: *The Leading Edge*, vol. 8, no. 09, pp. 30-36.
- Ushijima, K., Mizunaga, H., and Tanaka, T., 1999, Reservoir monitoring by a 4-D electrical technique, *The Leading Edge*, December 1999.
- Zebker, H.A., Rosen, R.A., Goldstein, R.M., Gabriel, A., and Werner, C.L., 1994, On the Derivation of Coseismic Displacement Fields Using Differential Radar Interferometry: The Landers Earthquake, *JGR*, vol. 99, pp. 19617-19634.
- Zhang, L., and Dusseault, B., 1996, Anisotropic Permeability Estimation by Horizontal Well Tests, *SPE37071*, pp. 301-309.

Chapter 5

Dynamic Monitoring: Compaction/Subsidence as an Additional Input/Constraint in the 4D Seismic Monitoring Workflow

5.1 Abstract

Published laboratory data acquired on unconsolidated shaly sands show that effective pressure increase may cause strong porosity reduction and velocity increase. We use these data in a range of pressure and water saturation (via theoretical fluid substitution) to design a rock physics transform that links the acoustic and elastic impedance to pore pressure, saturation, and porosity. By using a synthetic example, we show that impedance inversion volumes can be transformed into volumes of changes in pressure, saturation, and porosity.

This result demonstrates that by integrating 4D seismic and geomechanics, we can predict reservoir compaction due to production and pressure depletion. Since reservoir compaction and surface subsidence are closely related, InSAR measured surface subsidence will provide an integral constraint on the 4D seismic prediction of porosity loss. Therefore, it is possible to combine traditional 4D seismic workflow and InSAR measurements of surface subsidence for better reservoir monitoring.

5.2 Introduction

In Chapter 3, we studied the measurement of surface subsidence using InSAR. In Chapter 4, through reservoir simulation, we demonstrated that InSAR measured subsidence may be used as a stand-alone monitoring tool for detecting reservoir

permeability anisotropy. In this chapter, we will study the 4D seismic response to reservoir compaction, and discuss the integration of the 4D seismic workflow and InSAR measurements of surface subsidence for better reservoir monitoring.

Reservoir compaction due to hydrocarbon production is common in unconsolidated reservoirs worldwide. Compaction may result in well failure, surface subsidence, and platform sinking. Examples of subsidence from Wilmington, California; Belridge, California; Ekofisk, the North Sea; Lake Maracaibo, Venezuela; and Groningen, the Netherlands, are well documented.

In a realistic producing reservoir, compaction and seismic velocity changes often coexist. However, traditionally, reservoir compaction and 4D seismic have been treated as two separate technical areas, the former by geomechanics and the latter by seismic imaging. Reservoir compaction is commonly studied using laboratory stress-strain measurements and coupled geomechanics and flow simulation. 4D seismic velocity changes are commonly interpreted as the combined effect of pressure and saturation changes, without considering porosity changes caused by compaction. Rock physics that treats rock in its entirety provides a natural link between seismic attributes, reservoir properties and conditions.

In this chapter we explore the effect of reservoir compaction on static and dynamic reservoir properties through the integration of geomechanics and 4D seismic. To outline a new workflow that provides porosity changes (in addition to pressure and saturation changes) from impedance inversion, we examine a dataset by *Yin* [1992] that includes handmade sand/clay mixtures. Such samples are relevant to soft sediments found in many locations, including the Gulf of Mexico. We use one of the samples to design a transform between the acoustic and elastic impedances and pressure, saturation, and porosity. Then we use this rock physics transform in a synthetic example to show how to derive porosity reduction from seismic inversion data.

This result shows that we can predict porosity loss in a reservoir from 4D seismic. On the other hand, porosity loss in the reservoir is related to surface subsidence. In Chapter 3, we have shown the relationship between absolute volume loss on the ground (subsidence) and the absolute volume loss in the reservoir (compaction, or porosity loss). Therefore, this relationship provides an integral constraint on the 4D seismic prediction of porosity loss.

5.3 The Status & Limitations in Today's Reservoir Compaction Study

Currently, studies on the detection, prediction and mitigation of reservoir compaction are commonly focused on the following aspects: (1) Geomechanics --- laboratory measurements of reservoir rock to establish the constitutive relationship between stress and strain during loading, unloading, and reloading, performed for several cycles; (2) Numerical modeling --- coupled simulation of fluid flow and geomechanics to model and predict reservoir compaction, during which stage the established constitutive relationship is used as an input; (3) Reservoir engineering --- the design and optimization of injection patterns to mitigate reservoir compaction and surface subsidence, aiming at preventing well failure and/or platform sinking.

However, besides the cause and effect relationship of “pressure change --- reservoir compaction”, there is another side to reservoir compaction: because of the strong dependences between velocity and porosity, porosity loss due to reservoir compaction often results in the increase in seismic velocity. Since there is such relationship between porosity change and velocity change, and velocity change can be obtained from 4D seismic, we can detect reservoir compaction from 4D seismic.

5.4 The Status & Limitations in Today's 4D Seismic Study

The feasibility of 4D seismic was first demonstrated in the laboratory by ultrasonic rock physics measurements [*Tosaya et al.*, 1984; *Wang & Nur*, 1986; *Nur* 1989]. Some early testing of the method in the fields include *Eastwood et al.*, 1994; *Lumley*, 1995; *Jenkins et al.*, 1997; etc. The application of 4D seismic for reservoir monitoring and management has grown exponentially in recent years [*Lumley*, 2001].

Figure 5.1 shows a few commonly used techniques in reservoir management, which include both the 4D seismic technique and techniques that have close relationships to 4D seismic. First of all, the goal of 4D seismic monitoring is to image fluid flow in a reservoir at the production stage. The principle of 4D seismic is fairly simple: We first subtract two 3D seismic volumes acquired at two different times to obtain the seismic

changes (process 2 in figure 5.1), which are then mapped into reservoir property changes (process 3b). To perform the mapping, a site-specific rock physics transform, which links seismic properties and reservoir properties, has to be used. Comparing to flow simulation (process 1), which *predicts* fluid flow, the advantage of 4D seismic is that it directly *images* fluid flow.

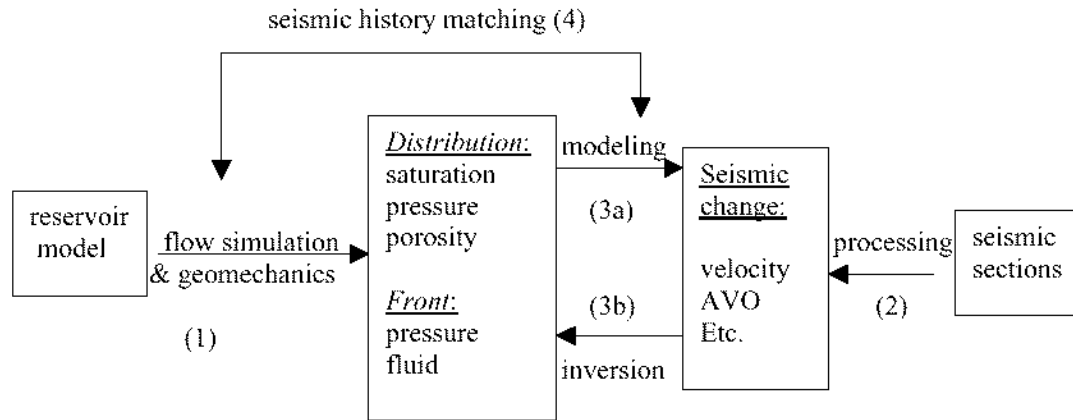


Figure 5.1: Links among reservoir simulation, 4D processing, 4D modeling, 4D inversion, and seismic history matching. Rock physics plays a central role in the dual processes of 4D modeling and 4D inversion.

The above process of “imaging fluid flow” from 4D seismic is an inversion process. There is also a forward process: if we have obtained reservoir property changes from flow simulation, then we can use forward modeling to obtain the 4D seismic change (step 3a). Again, in this forward process, a site-specific rock physics transform has to be used as well. It is straightforward that the rock physics transforms used in step 3a and step 3b have to be identical. It is also evident that rock physics plays a central role in the dual processes of 4D modeling and 4D inversion (steps 3a and 3b).

An optional step called “seismic history matching” (step 4), which optimizes between forward modeling and inversion, is sometimes used as well.

Currently most 4D seismic study aims at inverting pressure and saturation changes during production. There are many approaches to distinguishing the two effects from 4D seismic. Most of those approaches are based on the fact that pressure affects both P and S wave velocity, while saturation (approximately) only affects P wave velocity. Typically, a pair of seismic properties, each one containing either P or S wave information, are used. Commonly used pairs are “P wave velocity – S wave velocity”, “P wave velocity –

Vp/Vs ratio”, “AVO intercept – AVO gradient”, “Acoustic Impedance – Elastic Impedance”, “P wave impedance – Poisson’s ratio”, “Lame’s constant λ – Lame’s constant μ (both multiplied by density ρ)” etc [e.g., *Dvorkin et al.*, 1999; *Tura & Lumley*, 1999; *Landro*, 2001; *Carcione et al.*, 2001].

Although mathematically simple, the above approaches make, explicitly or implicitly, either one of the following two assumptions, which do not always hold:

- *Porosity does not change, or only undergoes very small changes, during production. Therefore, 4D seismic changes can be interpreted as the combined effects of pore pressure and fluid saturation changes only.*
- *Porosity may undergo changes, but it is implicitly included in the “velocity – pressure” relationship. Therefore, 4D seismic changes can still be interpreted as the combined effects of pore pressure and fluid saturation changes only.*

The first assumption is often incorrect. *Xu et al.* [2001] compiled a list of well-known compacting reservoirs worldwide, which demonstrated that not only does reservoir compaction (porosity loss) take place, but also it may be severe enough to cause significant surface subsidence.

The second assumption is sometimes incorrect as well, especially in unconsolidated soft sediments [*Prasad*, 2002, personal communication] or clay-rich sands [*Moos & Chang*, 1998; *Yin*, 1992]. There are two common mechanisms for porosity loss, neither of which can be handled implicitly by a “velocity-pressure” relationship: first, even under constant differential pressure, rock may undergo compaction (“creep”); second, when rock is loaded and then unloaded, even if the pressure does not change before and after the process, there may be porosity loss due to irrecoverable plastic deformation.

Figure 5.2 [*Moos & Chang*, 1998] shows the ultrasonic laboratory measurements on Wilmington sand. In Figure 5.2, porosity decreases during loading and rebounds during unloading. However, because porosity does not rebound fully during the unloading process, after one cycle, there is some permanent loss of porosity.

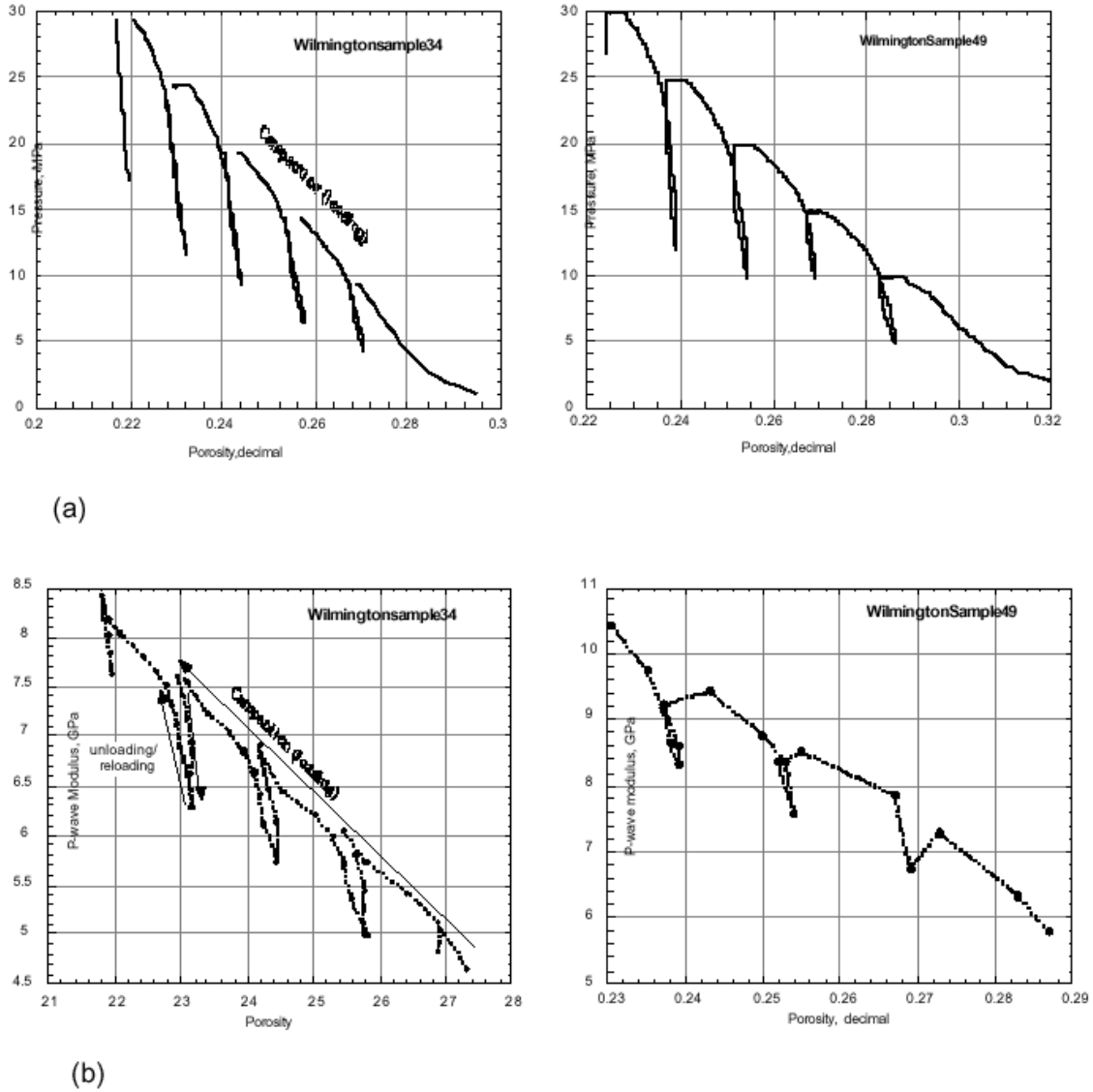


Figure 5.2: Ultrasonic laboratory measurements on Wilmington sands. (a) Confining pressure vs. porosity, illustrating loading (compaction) and unloading/reloading trends for the two samples in the study. (b) P-wave modulus calculated from pulse transmission measurements vs. porosity, showing time dependence. The loading, unloading and reloading trends can be seen clearly in the data as well [Moos & Chang, 1998].

Imagine we deplete a reservoir first and then manage to restore the pore pressure *fully* to its original state through injection. Because the pore pressure is restored fully, the pressure change before and after the full cycle is zero. However, because of porosity loss in the cycle, the rock velocity still increases. If we were to use the traditional “pressure, saturation \iff velocity” transform, then this velocity increase would be interpreted as pore pressure decrease. In other words, in a compacting reservoir, if porosity loss is

neglected, then the porosity effect on seismic will be wrongly interpreted as pressure effect. Specifically, neglecting porosity loss is equivalent to overestimating pore pressure decrease.

In addition, in the case of cyclic steam injection, porosity loss may accumulate during each cycle of loading and unloading. Therefore, even if porosity loss is small during each cycle, the cumulative effect may be significant.

5.5 Studying Reservoir Compaction and 4D Seismic Together

Reservoir compaction is a “static” effect, and velocity decrease is a “dynamic” effect. Therefore, the cause-effect relationship between reservoir compaction and velocity decrease contains both the “static” and the “dynamic” aspects.

However, interestingly, the two aspects of the same problem seem rarely to meet each other: On one hand, people who study reservoir compaction by measuring stress-strain curves in the lab rarely include velocity in their data interpretation, or even do not measure velocity changes (during loading, unloading, and reloading) at all. On the other hand, people who study time-lapse seismic monitoring often avoid the compaction issue by assuming constant porosity pre- and post-production.

New opportunities rise when we link the two aspects together. Specifically, there are two direct benefits if we are able to build the link between reservoir compaction and velocity change: (1) by including the compaction effect, we will achieve more accurate results in the 4D seismic study, especially in stress-sensitive reservoirs; (2) In reverse, with obtained 4D seismic data, using the link between reservoir compaction and velocity change, we can interpret it back to reservoir property changes, one of which is porosity change (reservoir compaction).

In this chapter, we attempt to build such a link --- a rock physics model -- by investigating the combined effects of pressure, saturation, and porosity on 4D seismic, based on published laboratory measurements. The model differs from existing compaction detection methods in that it may be used to detect compaction not from “stress-strain relationship”, but from “velocity-porosity relationship”. The model also differs from existing 4D techniques in that it not only considers pressure and saturation changes during production, but also considers porosity changes.

The methodology illustrated in this chapter may be used to construct site-specific rock models that can be readily applied in the following aspects: (1) detecting pressure, saturation, and porosity changes from 4D seismic, which are important for reservoir production management; (2) detecting absolute values of pressure, saturation, and porosity from 3D seismic, which are essential for overpressure detection, direct hydrocarbon identification, and reservoir characterization. In both cases, the only necessary inputs are 3D/4D seismic cubes and calibrated *site-specific* rock physics transforms; the outputs are pressure, saturation, and porosity cubes, or cubes of their changes.

In all the following discussions, isothermal conditions are assumed.

5.6 Yin's Laboratory Data of Shaly Sands

Figure 5.3 shows the ultrasonic laboratory measurements of Yin [1992]. As a quality control step, the data were smoothed to avoid sudden jumps in shear wave velocity measurements, which are often error-prone at low effective pressures. The plot shows the porosity and velocity changes of one single sample during loading and unloading. The sample of sand-clay mixture was prepared by mixing 70% clean Ottawa sand with 30% pure Kaolinite powder at room dry condition. The sample weighed 100 grams. The sample was loaded and then unloaded, and porosity was measured during the process (top plate). P wave and S wave velocities were measured simultaneously during the loading and unloading process (bottom plate).

During the loading cycle, the initial porosity of 27% as measured at about 10 MPa differential (confining minus pore, where pore pressure = 0 MPa for dry) pressure decreases to 24.5% at 15 MPa and 19.5% at 25 MPa (values are extrapolated from lab data). Such changes in differential pressure may occur in a high-pressure reservoir produced by depletion. The elastic-wave velocity changes associated with the differential pressure changes are also dramatic. The dry-rock P-wave velocity increases from 1100 to 1550 to 1750 m/s (extrapolated) as the pressure increases from 5 to 15 to 25 MPa. The corresponding S-wave velocity values are 600, 800, and 900 m/s (extrapolated). Also notice that during one full cycle of loading and unloading, due to

irrecoverable porosity loss, velocity increases significantly ($\sim 10\%$ for P wave velocity, $\sim 20\%$ for S wave velocity).

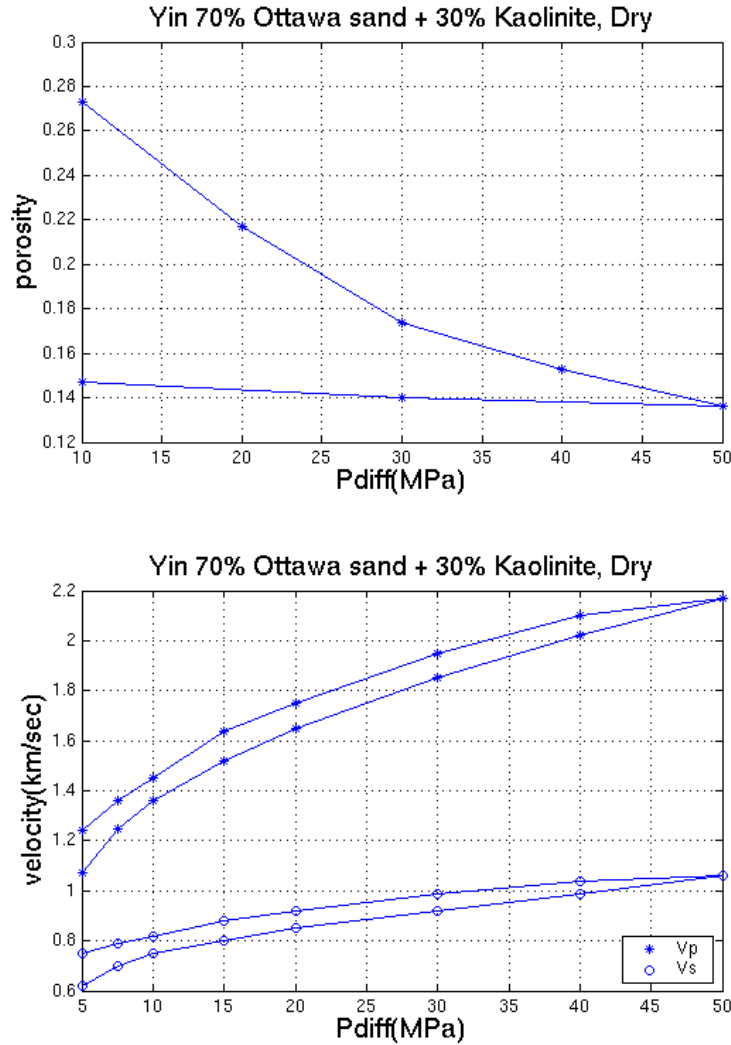


Figure 5.3: Laboratory data of Yin [1992] on room-dry sand-clay mixture of 30% clay content. Top – porosity versus differential (confining minus pore) pressure. The upper branch is loading while the lower branch is unloading. Bottom – P- and S-wave velocity versus differential pressure. The lower branches are for loading while the upper branches are for unloading.

The elastic-wave velocity changes shown in Figure 5.3 can be transformed into the changes of the acoustic and elastic impedance (Figure 5.4). This step is important for monitoring recovery from seismic impedance inversion. We see that both P and S wave impedances increase as differential pressure increases. Notice the pronounced effect of compaction on the dry-rock Poisson's ratio – it is relatively small in the uncompacted

rock (about 0.24) and increases to 0.34 as the rock is compacted to 14% porosity. The increase of Poisson's ratio with increasing differential pressure is often a good indication of dry or gas-saturated sands [Dvorkin *et al.*, 1999].

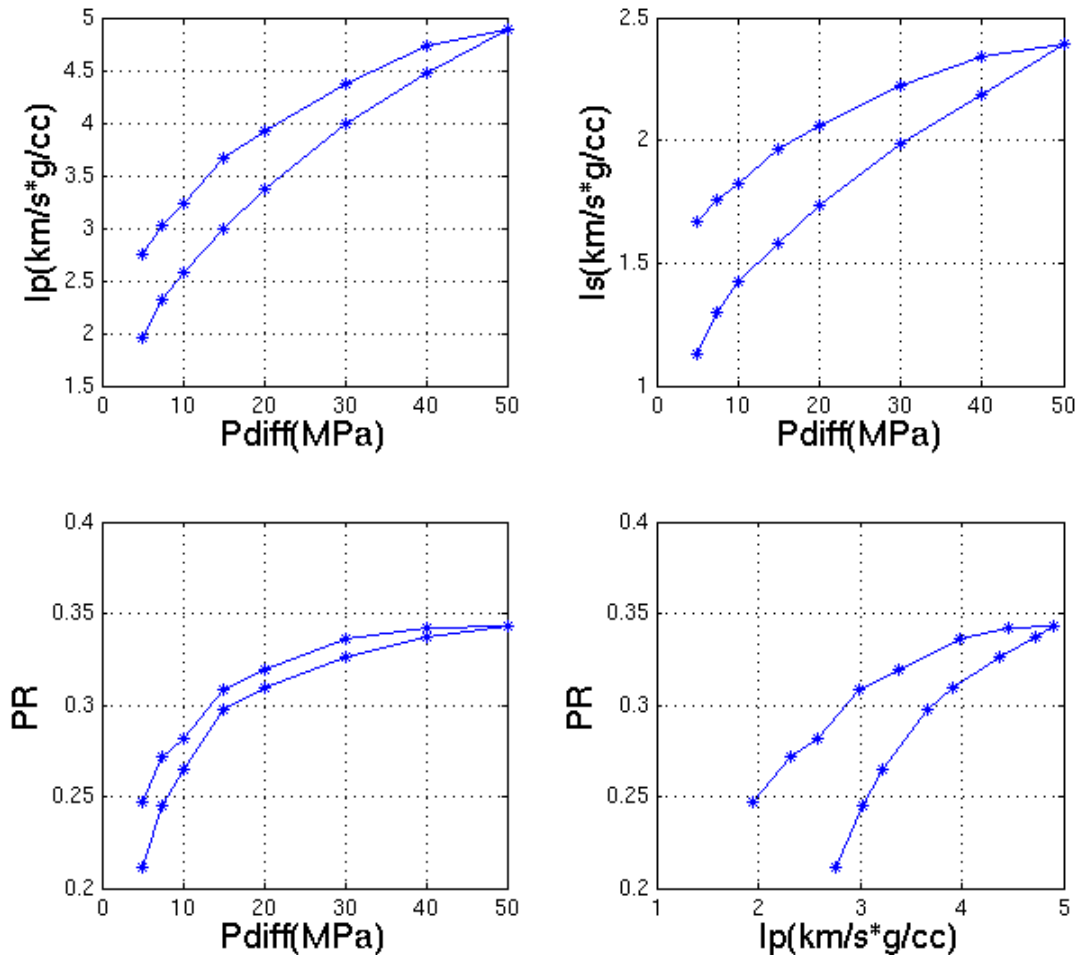


Figure 5.4: Laboratory data of Yin [1992] on room-dry sand-clay mixture of 30% clay content. Upper row – P- and S-wave impedance versus the differential pressure. Lower row – Poisson's ratio versus the differential pressure (left) and versus P-wave impedance (right). In the lower row, the upper branch is for loading while the lower branch is for unloading.

The experimental data shown in Figure 5.3 and 5.4 can be used to predict seismic property changes not only due to pressure but also due to saturation. An example is given in Figure 5.5, where we use fluid substitution (uniform and patchy) to calculate the elastic properties at partial and full water saturation from the dry-rock data.

Especially useful may be the Poisson's ratio versus P-wave impedance map that shows how the same rock sample occupies different positions depending on the state of

pressure and saturation (Figure 5.5, bottom row, right). This map can serve to simultaneously predict pore pressure and saturation from the acoustic impedance (P-wave impedance) and elastic impedance (Poisson's ratio) that come from seismic inversion.

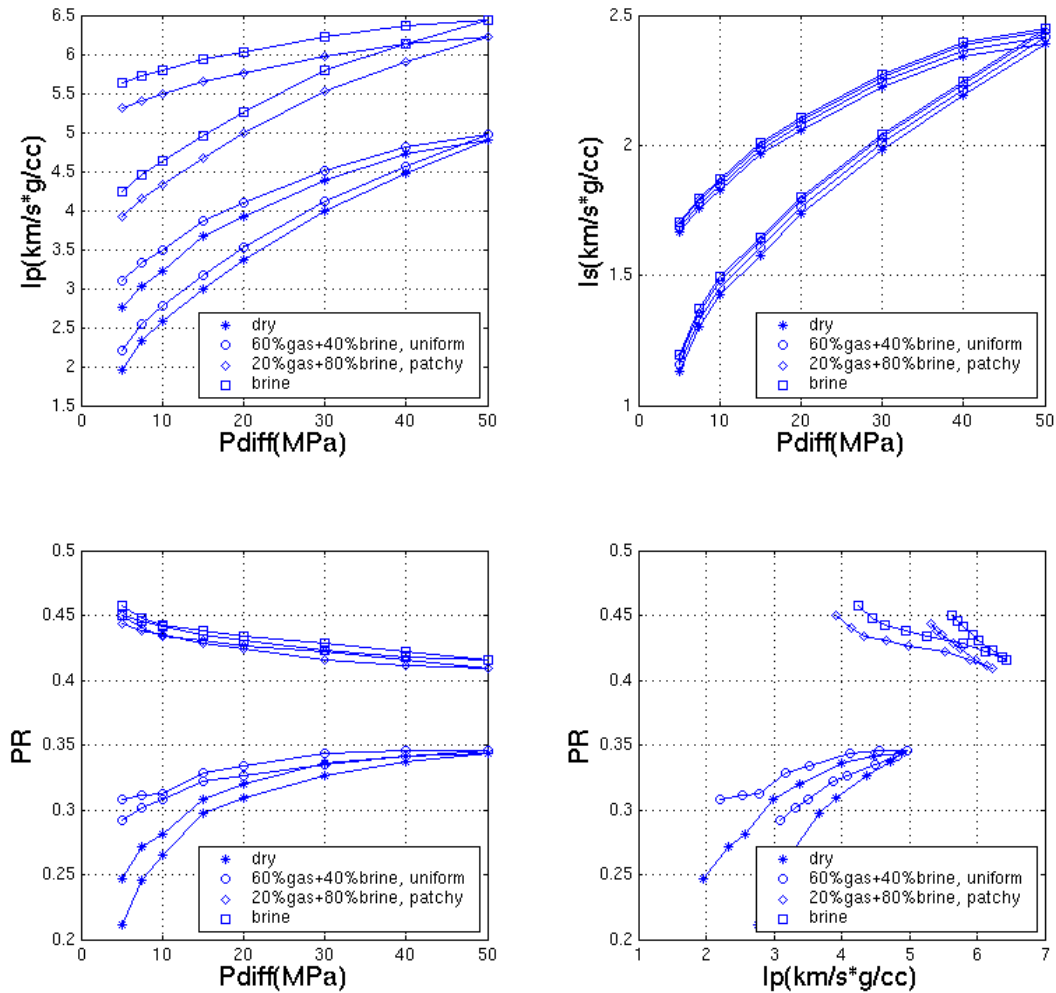


Figure 5.5: Upper row – P- and S-wave impedance versus the differential pressure for varying saturation. Lower row – Poisson's ratio versus the differential pressure (left) and versus P-wave impedance (right) for varying saturation. Dry data are from Yin's [1992] sand-clay mixture of 30% clay content. Saturated data are obtained from fluid substitution based on the dry data. During fluid substitution, uniform and patchy saturation methods have been used. Patchy saturation pattern is not uncommon during recovery in a heterogeneous reservoir.

To create this map, the original dry-rock experimental data have been used. Fluid substitution has been used to calculate the elastic properties of this sample at fully brine saturation as well as at partial saturation, using Gassmann's [1951] fluid substitution (uniform fluid distribution) for 60% gas and 40% brine in the pore space, and patchy

fluid substitution for 20% gas and 80% brine in the pore space. Figure 5.5 shows that pore pressure and saturation can be determined via rock physics if the P-wave impedance and Poisson's ratio are known from seismic.

5.7 Reservoir Compaction During Primary Depletion

Let us focus on the loading branch of the experiment shown in Figure 5.3. The compaction behavior of the shaly sand will be relevant to that occurring during primary reservoir depletion. By conducting fluid substitution within a large pressure range, we create surfaces of P-impedance and Poisson's ratio versus pressure and saturation (Figure 5.6).

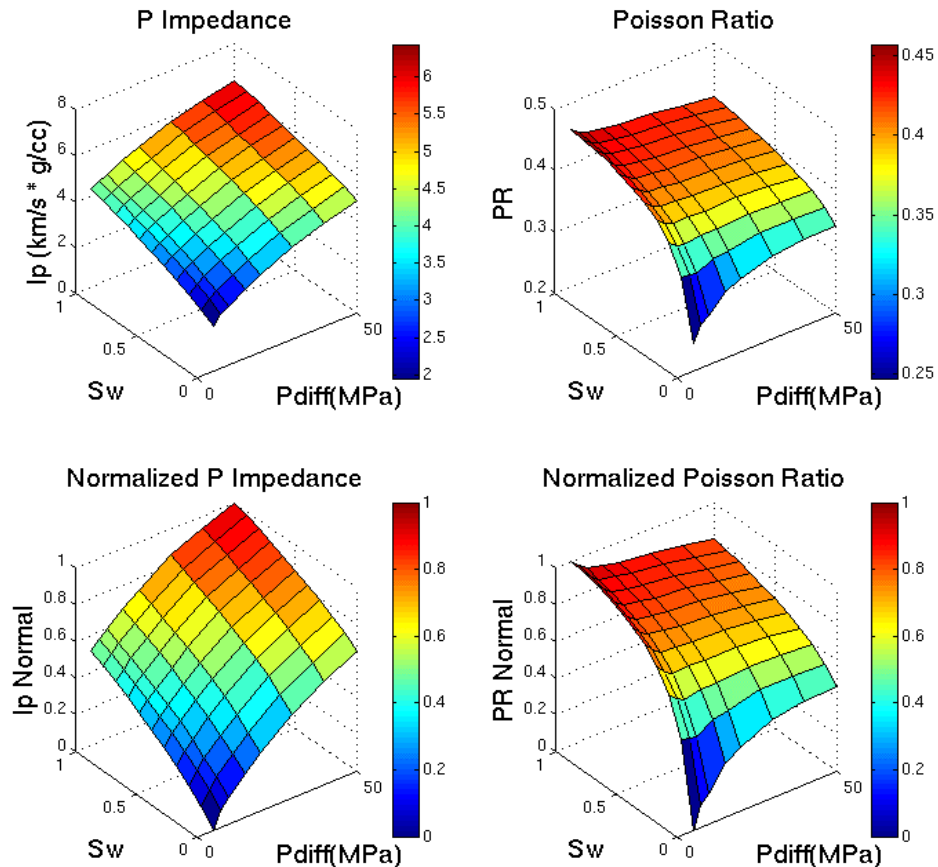


Figure 5.6: Patchy fluid substitution to estimate the P-wave impedance and Poisson's ratio variations within an effective pressure range. Upper row – absolute values. Lower row – values normalized between zero and one. Left column – P-wave impedance. Right column – Poisson's ratio

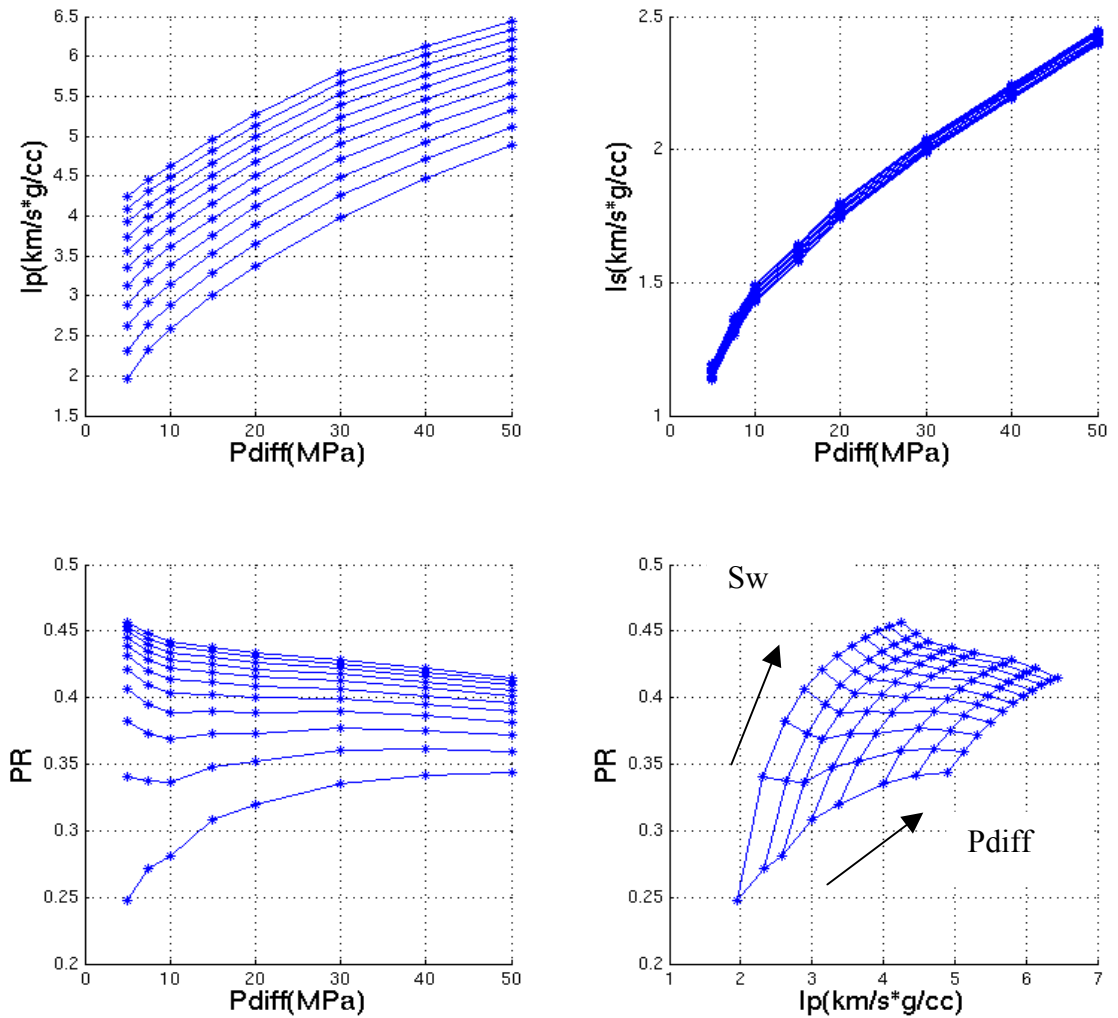


Figure 5.7: Upper row – P-wave impedance and S-wave impedance versus differential pressure and for varying saturation using patchy fluid substitution. Lower row – Poisson’s ratio versus differential pressure and versus P-wave impedance at varying pressure and saturation. Arrows show increasing P_{diff} or Sw . For the bottom right panel, $P_{diff} = 5, 7.5, 10, 15, 20, 30, 40, 50$ MPa, and Sw vary from 0 to 1 with step of 0.1.

The projections of the surfaces drawn in Figure 5.6 onto various rock physics planes are shown in Figure 5.7. They show that as differential pressure increases, both P- and S-wave impedances increase; as brine saturation increases, P- impedance increases, while S- impedance does not change significantly. Poisson’s ratio behaves differently: at high gas saturation, Poisson’s ratio increases with differential pressure; however, as brine saturation goes up, Poisson’s ratio decreases when differential pressure increases. We observe that after a certain threshold in differential pressure, Poisson’s ratio is almost

fully dependent on saturation, and does not change too much even when differential pressure is increased further [Domenico, 1977; Xu *et al.*, 1999]. Recent experiments [Prasad, 2002; Zimmer, 2002; Huffman & Castagna, 2001] have shown that if the differential pressure is even lowered further, sand is in a state of suspension (which produces very high Poisson's ratio, if water saturated) and is prone to shallow water flow hazards.

Especially important is the Poisson's ratio versus P-wave impedance crossplot that is in fact a diagnostic crossplot for simultaneously identifying pressure and saturation from the acoustic and elastic impedance. This plot is a basis for interpreting seismic inversion in terms of pore pressure and saturation. Using this plot, it is straightforward to go back and forth between (pressure, saturation) and (P impedance, Poisson's ratio). Having obtained the transform between (pressure, saturation) and (P impedance, Poisson's ratio), combining with the transform between pressure and porosity (the loading curve in Figure 5.3), we can detect reservoir compaction (porosity loss) from 4D seismic changes.

5.8 A Synthetic Example

Now let us consider a synthetic example --- a one-layer gas reservoir model with gas produced from the lower right corner and water entering in the upper left corner (Figure 5.8). The initial impedance and Poisson's ratio are set to be 3.1 km/s*g/cc and 0.36 respectively. As gas is produced, the pore pressure decreases (the differential pressure increases) and the water saturation increases. These changes (assigned for illustration purposes only; in practice they are typically obtained from reservoir simulation --- see Figure 5.1) in the 2D reservoir model are shown in Figure 5.8, upper row. The corresponding changes in the P-wave impedance and Poisson's ratio are calculated from the diagrams shown in Figure 5.6 and 5.7, and the new values of P-wave impedance and Poisson's ratio are shown in Figure 5.8, lower row.

Our goal is to interpret these changes in terms of pore pressure, water saturation, and, most important, porosity changes. The interpretation in terms of pore pressure and saturation is straightforward and is based on the surfaces drawn in Figure 5.6. Once pore pressure changes are known, the upper diagram from Figure 5.3 is used to calculate the

porosity changes in the reservoir. The results of this interpretation are shown in Figure 5.9.

The porosity changes appear to be large, especially in the vicinity of the gas producing well. The 0.08 porosity change from the initial porosity of about 0.3 accounts for about 25% pore volume change which translates into about 8% reservoir volume change. Such compaction in a thick reservoir can easily cause strong subsidence and wellbore damage. The rock physics methods described in this section allow us to monitor such compaction using seismic reflection profiling.

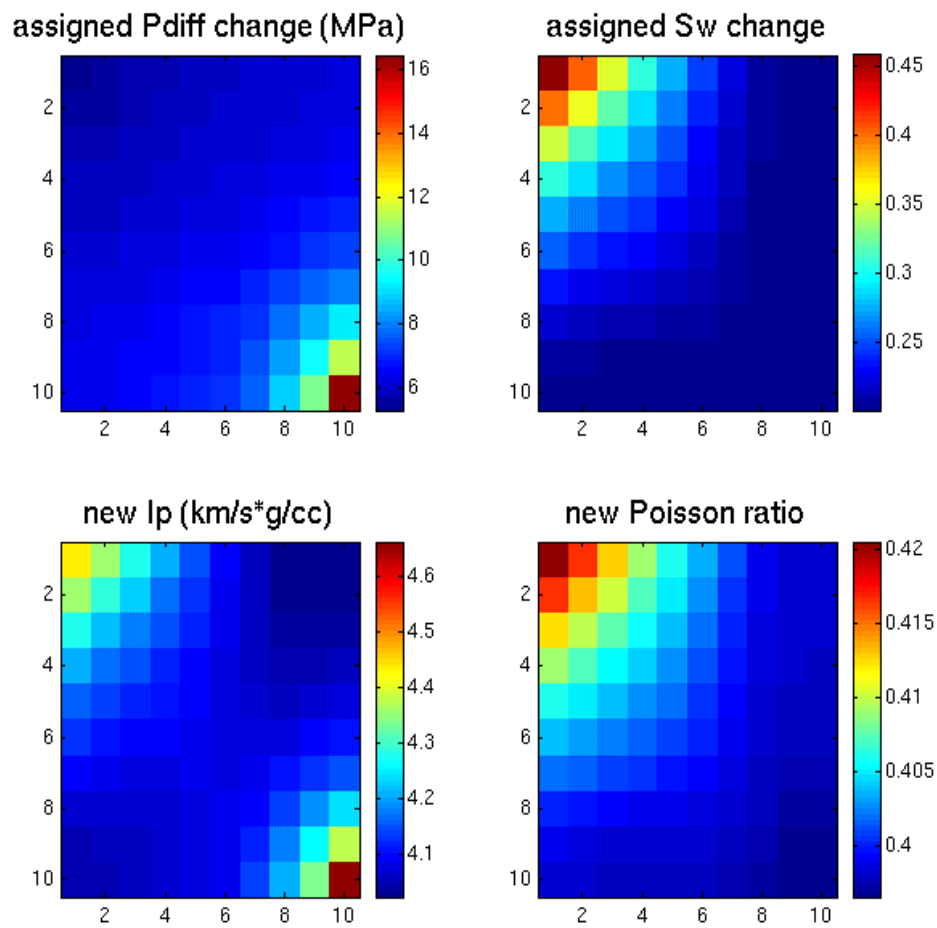


Figure 5.8: Upper row – Differential pressure and water saturation change during gas production from a model rectangular reservoir (map view). Gas is produced from the lower right corner and water is entering into the upper left corner. Lower row – calculated new P-wave impedance and Poisson's ratio. The initial Impedance and Poisson's ratio are set to be 3.1km/s*g/cc and 0.36 respectively (uniform).

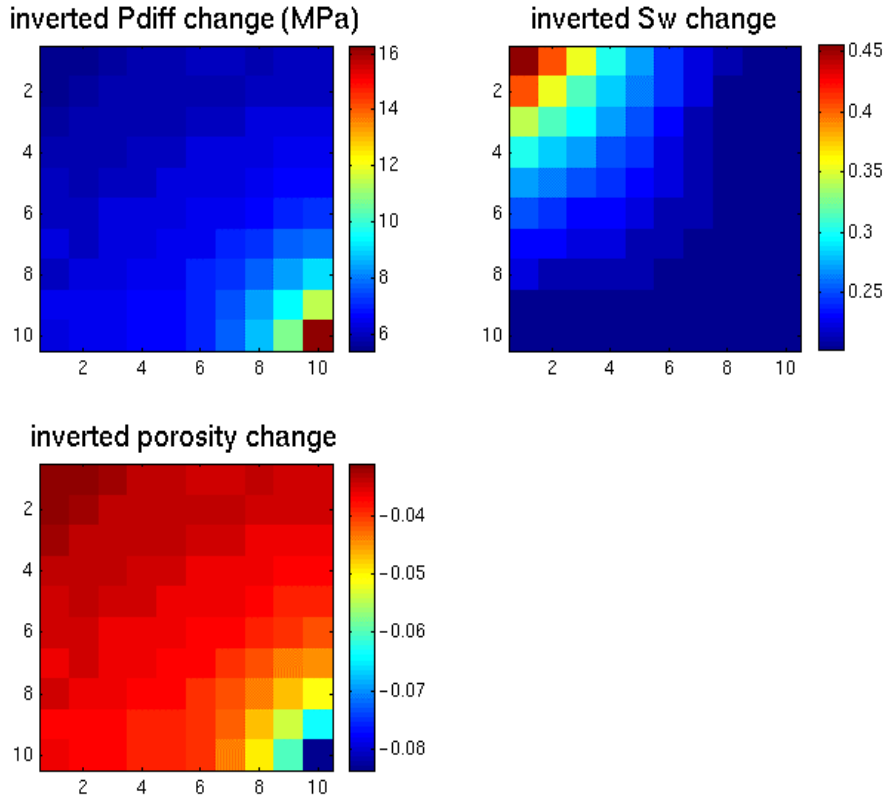


Figure 5.9: Pressure, saturation, and porosity changes from changes of P-wave impedance and Poisson's ratio.

To apply this method, the necessary inputs are (1) impedance and Poisson's ratio changes obtained from 4D seismic inversion; (2) rock physics transforms linking velocity to pressure, saturation and porosity (such as the one in Figure 5.7). The output will be pressure, saturation, and porosity changes during production.

There is also another use for Figure 5.7: Suppose the reservoir is under neither production nor injection. We merely acquire a 3D seismic survey, which is essentially a still picture of the reservoir for one single time point. Using well-established inversion techniques, we can obtain cubes of impedance and Poisson's ratio from the 3D seismic data. Then, using the transform in Figure 5.7, we can predict pressure and saturation distributions for the reservoir, which is very useful for reservoir characterization; direct hydrocarbon detection; and overpressure detection.

The example shown here is based on data from one sand/clay sample. The principle is general and has to be calibrated by site-specific data. The method can be used for reservoir characterization and monitoring, with emphasis on compaction monitoring.

5.9 Reservoir Compaction for Cycles of Depletion and Injection

The approach used here to link the inversion impedance to pore pressure, saturation, and porosity changes can be projected to other seismic attributes domains commonly used in the industry. Figure 5.10 shows the combined effect of pressure, saturation, and porosity on seismic changes plotted in six different attributes domains. For calculation of AVO intercept and gradient, caprock (shale) properties are assumed, and densities for sands and shales are estimated using the well-known Gardner formula [Mavko *et al.*, 1998].

Figure 5.10 shows the plot in the following domains: (top left) Poisson's ratio versus P impedance; (top right) P and S velocity ratio versus P velocity; (middle left) P versus S wave velocity; (middle right) AVO intercept versus AVO gradient; (bottom left) acoustic impedance versus elastic impedance (at 30°); (bottom right) Lamé's constant λ versus Lamé's constant μ , both multiplied by bulk density ρ .

Some interesting observations:

- *V_p - V_s plot appears as near horizontal lines (parallel to the x axis), because V_s almost does not change with saturation.*
- *Similarly, $\lambda\rho$ - $\mu\rho$ plot appears as near vertical lines (parallel to the y axis), because shear modulus does not change with saturation.*
- *V_p/V_s - V_p plot looks similar to PR- I_p plot, because Poisson's ratio directly depends on V_p/V_s ratio.*
- *In AI-EI plane, saturation effect is most dominant, while the pressure effect seems to be shrinking together.*

Figure 5.11 shows a synthetic example. The first row shows the initial reservoir condition. We do reservoir simulation to simulate the pressure and saturation changes due to gas production (lower right corner of the reservoir) and water injection (upper left corner of the reservoir). The changes are shown in the second row. These changes result in new distributions of pressure, saturation, impedance, Poisson's ratio, and porosity (third row). Then, we conduct reservoir simulation again to simulate the pressure and saturation changes (fourth row) due to water injection only from the lower right corner

of the reservoir. These changes result in new distributions of pressure, saturation, impedance, Poisson's ratio, and porosity (fifth row).

Comparing the values for the base survey (first row), repeat survey (third row), and the second repeat survey (fifth row), we observe that after the restoration of pressure, pressure is restored substantially, however there is almost no rebound in porosity. This phenomenon has been observed in many fields subject to compaction and subsidence, where injection programs help maintain pore pressure successfully but fail to mitigate subsidence.

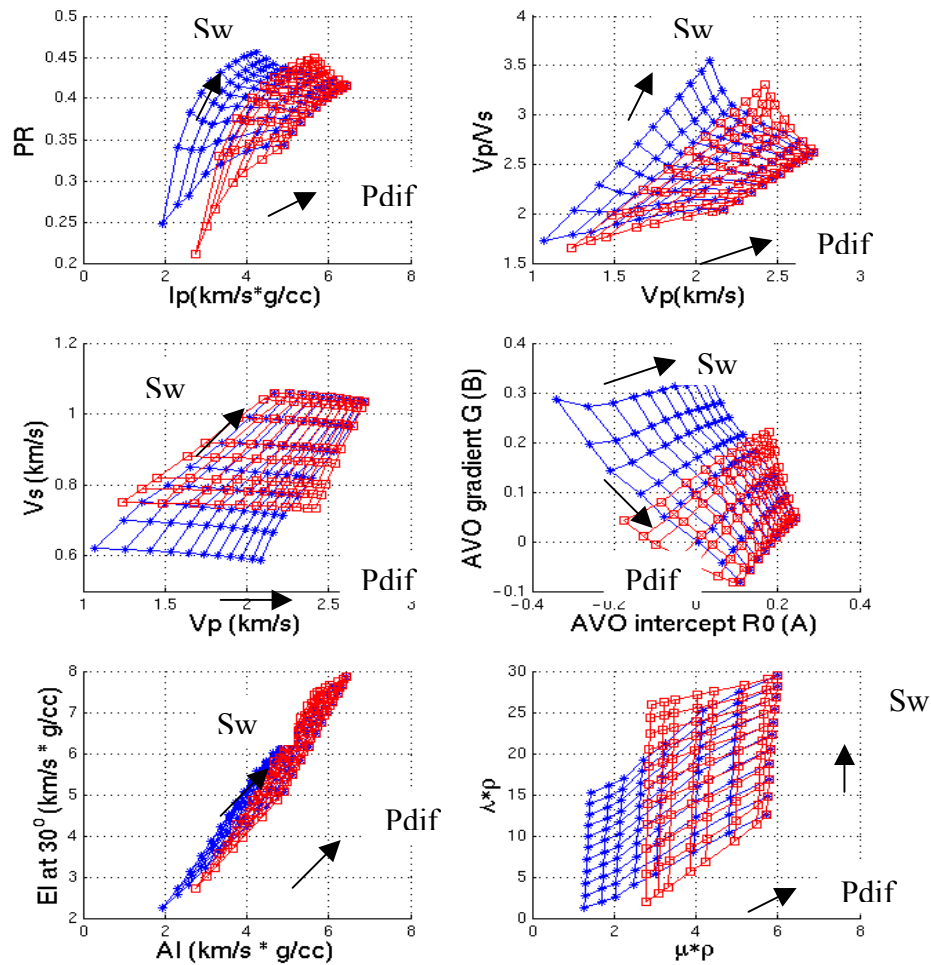


Figure 5.10: The combined effect of pressure, saturation, and porosity on seismic changes in six different domains. Row 1, left, Poisson's ratio versus P-wave impedance, and right, Vp/Vs ratio versus P-wave velocity. Row 2, left, P- versus S-wave velocity, and right, AVO intercept versus AVO gradient. Row 3, left, acoustic impedance versus elastic impedance at 30° , and right, Lamé's constant λ versus Lamé's constant μ , both multiplied by bulk density ρ . In all the domains, blue color corresponds to loading curve in Figure 5.10, and red color corresponds to unloading curve in Figure 5.11. Arrows show the directions of increasing differential pressure and water saturation.

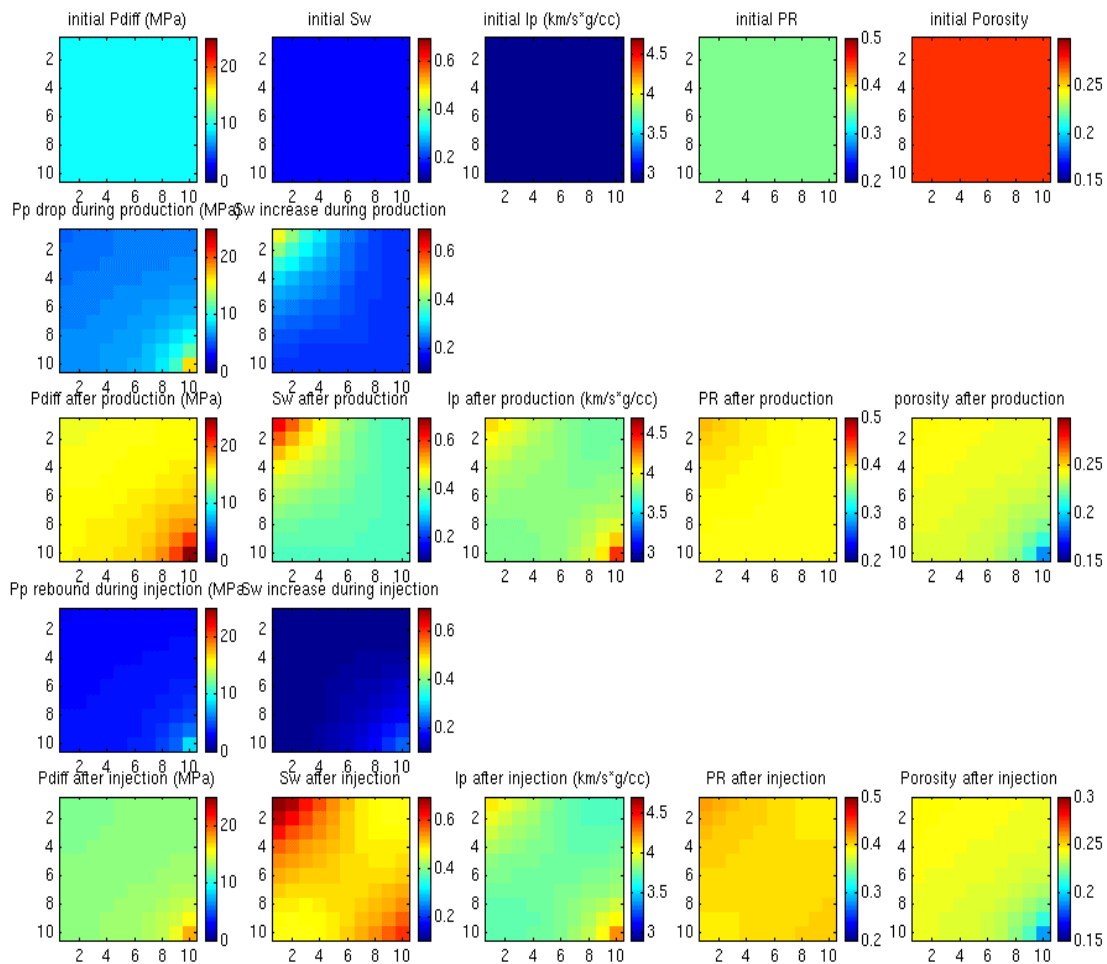


Figure 5.11: A synthetic example for one cycle of production and injection. The first row corresponds to base survey, the third row corresponds to repeat survey, the fifth row corresponds to a second repeat survey. The second and fourth rows are pressure and saturation changes between the surveys. First row: the initial reservoir condition. Second row: simulated pore pressure and saturation changes during production. Third row: new distributions of pressure, saturation, impedance, Poisson's ratio, and porosity. Fourth row: simulated pore pressure and saturation changes during pressure restoration. Fifth row: new distributions of pressure, saturation, impedance, Poisson's ratio, and porosity.

5.10 Discussion

The recent progress of geophysical measurement technology can allow one to extract both compressional and shear-wave data (such as impedance and Poisson's ratio) from surface and marine (OBC) seismic data, well logs, and cross-well measurements. For example, high resolution velocity and impedance can be inverted from seismic using

tomography [Lee *et al.*, 1998; Sayers *et al.*, 2002] or prestack full-waveform inversion [Dutta, 2002]. Because of this, the rock physics transforms presented in this chapter can easily be applied to extract reservoir properties from seismic volumes, and to detect reservoir compaction from 4D seismic.

The key in successfully applying this methodology is to fine-tune the best rock physics transform for the specific site under investigation. Specifically, we have to pay special attention to the following issues: (1) We have to choose the correct loading/unloading/reloading path for a specific situation. For example, although both secondary depletion (after injection) and primary depletion are processes during which differential pressure increases, they go along different loading/reloading paths. For a unconsolidated reservoir, if porosity decreases significantly during primary depletion, it may not decrease too much during secondary depletion. (2) We have to take into account the discrepancies between laboratory and field due to frequency dispersion and scale differences. (3) We have to take into account the uncertainty associated with saturation scales. In this chapter, we used patchy saturation in the fluid substitution. However, in reality, homogeneous, patchy, or some type of combination of the two, may be present. (4) We have to take into account the heterogeneity of the reservoir. For example, in this chapter, we start with one sample with a specific porosity, and put it under loading and unloading. However, in the field, there may be a distribution of different initial porosities. We have to take care of uncertainties associated with the heterogeneities as well. (5) The reservoir may be anisotropic, it may contain faults and fractures, all these issues will have to be considered as well. (6) To successfully map a field or its change, we need not only understand the properties of reservoir sands (which we present in this chapter), but also need to understand the properties of the overburden (sands and shales) as well. (7) In this chapter, we used rock physics transforms purely from laboratory measurements. As there are often significant errors in measuring velocity at low effective pressure (especially shear wave measurements), it is desirable to use theoretical models together with laboratory data to ensure quality.

5.11 Conclusions

In this chapter, we presented rock physics transforms which link velocity to pressure, saturation, and porosity, based on published laboratory measurements. The transforms can in principle be applied to two situations: (1) predict reservoir properties directly from 3D seismic, for example, overpressure prediction, direct hydrocarbon detection, and reservoir characterization. (2) detect reservoir property changes directly from 4D seismic, for example, pressure and saturation change mapping, and reservoir compaction detection. Although the transform itself may not be applied directly because it is rock-specific, the potential application of the methodology illustrated through the examples is very promising.

The results demonstrate that by integrating 4D seismic and geomechanics, we can predict reservoir compaction due to production and pressure depletion. Since reservoir compaction and surface subsidence are closely related, InSAR measured surface subsidence will provide an integral constraint on the 4D seismic prediction of porosity loss. Therefore, it is possible to combine traditional 4D seismic workflow and InSAR measurements of surface subsidence for better reservoir monitoring.

5.12 Acknowledgments

This work was supported by the Stanford Rock Physics & Borehole Geophysics Project (SRB) and DOE.

5.13 References

- Carcione, J. and Tinivella U., 2001, The seismic response to overpressure: a modeling study based on laboratory, well, and seismic data, *Geophysical Prospecting*, vol. 49, no. 5, pp. 523.
- Domenico, S. N., 1977, Elastic properties of unconsolidated sand reservoirs, *Geophysics*, vol. 42, pp. 1339-1368.
- Dutta, 2002, Deepwater geopressure prediction using prestack inversion of large offset P-wave data and rock model, *The Leading Edge*, vol. 21, no. 2, pp. 193.

- Dvorkin, J., Mavko, G., and Nur, A., 1999, Overpressure detection from compressional and shear-wave data, *Geophysical Research Letters*, 26, pp. 3417-3420.
- Eastwood, J., Lebel, P., Dilay, A., and Blakeslee, S., 1994, Seismic monitoring of steam-based recovery of bitumen: *The Leading Edge*, 13, pp. 242-251.
- Gassmann, F., 1951, Elasticity of porous media: Uber die elastizitat poroser medien, *Vierteljahrsschrift der Naturforschenden Gessellschaft*, 96, 1-23.
- Huffman A. and Castagna J., 2001, The petrophysical basis for shallow water flow predication using multicomponent seismic data, *The Leading Edge*, vol. 20, no. 9, pp. 1030.
- Lee S., Shaw J., Ho R., Burger, J., Singh, S., and Troyer, B., 1998, Illuminating the shadows: tomography, attenuation, and pore-pressure processing in the south Caspian sea, *The Leading Edge*, vol. 17, no. 6, pp. 777.
- Jenkins, S. D., Waite, M. W., and Bee, M. F., 1997, Time-lapse monitoring of the Duri steamflood: A pilot and case study: *The Leading Edge*, 16, pp. 1267-1273.
- Landro, M., 1999, Discrimination between pressure and fluid saturation changes from time lapse seismic data: *69th Ann. Internat. Mtg., Soc. Expl. Geophys.*, Expanded Abstracts, pp. 1651-1654.
- Lumley, D. E., 1995, 4-D seismic monitoring of an active steamflood: *65th Ann. Internat. Mtg., Soc. Expl. Geophys.*, Expanded Abstracts, pp. 203-206.
- 2001, Review of time-lapse seismic monitoring, *Geophysics*, Jan-Feb 2001.
- Mavko, G., Mukerji, T., & Dvorkin, J., 1998, *Rock physics handbook*, Cambridge University Press.
- Moos & Chang, 1998, Relationships between porosity, pressure, and velocities in unconsolidated Sands, presented at "Overpressures in Petroleum Exploration" workshop, Pau France, April 1998.
- Nur, A., 1989, Four-dimensional seismology and (true) direct detection of hydrocarbons: The petrophysical basis: *The Leading Edge*, vol. 8, no. 9, pp30-36.
- Prasad, M., 2002, Acoustic measurements in sands at low effective pressure: overpressure detection in sands, *Geophysics*, Vol. 67, no. 2, pp. 405-412.
- Sayers, C., Woodward, M., and Bartman, R., 2002, Seismic pore pressure prediction using reflection tomography and 4-C seismic data, *The Leading Edge*, vol. 21, no. 2, pp. 188.
- Tosaya, C.A., A. Nur, P. Aronstam, and G.Da Prat, 1984, Monitoring of thermal EOR fronts by seismic methods, *SPE California regional meeting*, pp. 12744.
- Tura, A., and Lumley, D. E., 1999, Estimating pressure and saturation changes from time-lapse AVO data: *69th Ann. Internat. Mtg., Soc. Expl. Geophys.*, Expanded Abstracts, pp. 1655-1658.

- Wang, Z., and Nur, A., 1986, Effect of temperature on wave velocities in sands and sandstones with heavy hydrocarbons: *56th Ann. Internat. Mtg., Soc. Expl. Geophys.*, Expanded Abstracts, session BHG1.2.
- Xu, H., J. Dvorkin, and A. Nur, 2001, Linking oil production to surface subsidence from satellite radar interferometry, *Geophysical Research Letters*, Vol. 28, #7, (April 2001). pp. 1307-1310.
- Xu, S. and Keys, R., 1999, Study of coupled effect of pressure, frequency, and fluid content on P- and S- wave velocities, *SEG abstracts 1999*.
- Yin, H., 1992, Acoustic velocity and attenuation of rocks: isotropy, intrinsic anisotropy, and stress induced anisotropy, Ph.D. thesis, Stanford University.
- Zimmer M., Prasad M., and Mavko, G., 2002, Pressure and porosity influences on Vp-Vs ratio in unconsolidated sands, *The Leading Edge*, vol. 21, no. 2, pp. 178.